

(NASA-CR-120423) RESULTS OF TESTS TO DETERMINE THE AERODYNAMIC CHARACTERISTICS OF TWO POTENTIAL AEROMANEUVERING ORBIT-TO-ORBIT SHUTTLE (Lockheed Missiles and Space Co.) 118 p HC \$9.00 CSCL 22C	N74-33302  Unclas G3/31 17138
---	--

*Lockheed*

**HUNTSVILLE RESEARCH & ENGINEERING CENTER**

LOCKHEED MISSILES & SPACE COMPANY, INC.  
A SUBSIDIARY OF LOCKHEED AIRCRAFT CORPORATION

HUNTSVILLE, ALABAMA

LOCKHEED MISSILES & SPACE COMPANY, INC.  
HUNTSVILLE RESEARCH & ENGINEERING CENTER  
HUNTSVILLE RESEARCH PARK  
4800 BRADFORD DRIVE, HUNTSVILLE, ALABAMA

RESULTS OF TESTS TO DETERMINE  
THE AERODYNAMIC  
CHARACTERISTICS OF TWO  
POTENTIAL AEROMANEUVERING  
ORBIT-TO-ORBIT SHUTTLE (AMOS)  
VEHICLE CONFIGURATIONS IN THE  
NASA-AMES 3.5-FOOT HYPERSONIC  
WIND TUNNEL - FINAL REPORT

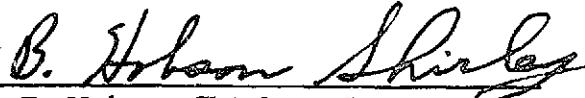
May 1974  
Contract NAS8-28608

Prepared for National Aeronautics and Space Administration  
Marshall Space Flight Center, Alabama 35812

by

F. C. Ketter, Jr.

APPROVED:



B. Hobson Shirley, Supervisor  
Aero-Mechanics Section

  
J. S. Farrior  
Resident Director

## FOREWORD

This report presents the results of an experimental investigation to define the aerodynamic force and static stability characteristics of potential orbit-to-orbit transfer vehicle configurations. Also, experimental data are compared with theoretical data predicted by Newtonian theory.

The tests were conducted in the NASA-Ames 3.5-Foot Hypersonic Wind Tunnel by personnel of the Lockheed-Huntsville Research & Engineering Center (Lockheed-Huntsville) for the NASA-Marshall Space Flight Center (MSFC) under Contract NAS8-28608.

This report was prepared in response to the requirements of the subject contract. The MSFC Contracting Officer's Representative is Mr. Josh D. Johnson, S&E-AERO-AAE.

## ACKNOWLEDGEMENTS

The author is grateful for the technical support and contributions by the following Lockheed-Huntsville personnel: D. B. Merriman, D. A. Love and C. D. Andrews.

CONTENTS

<u>Section</u>	<u>Page</u>
FOREWORD	ii
NOMENCLATURE	xi
1 INTRODUCTION AND SUMMARY	1
2 TEST INFORMATION	4
2.1 Test Facility	4
2.2 Test Conditions	4
2.3 Model Description	5
2.4 Test Apparatus	5
2.5 Data Reduction and Accuracy	6
3 RESULTS AND DISCUSSION	8
3.1 Comparison of AMOOS 5B Experimental Data with Theory	8
3.2 Comparison of AMOOS HB Experimental Data with Theory	13
3.3 Effects of Reynolds Number Variation on the Experimental Data	19
4 CONCLUSIONS	20
5 RECOMMENDATIONS	21
REFERENCES	22
Appendix	
A Justification for Use of Newtonian Flow Theory	A-1

## LIST OF TABLES

<u>Number</u>		<u>Page</u>
1	Detail Drawings of the AMOOS Models and Sting Assembly	23
2	Maximum Balance Loads (Task MK XLI-A) Used During AMOOS 5B Tests	24
3	Maximum Balance Loads (Task MK XVIII) Used During HB Tests	25
4	Reference Dimensions	26
5	Coefficient Accuracy	27
6	Test Schedule	28

## LIST OF ILLUSTRATIONS

<u>Figure</u>		<u>Page</u>
1	The Ames 3.5-Foot Hypersonic Wind Tunnel and Model Support System	29
2	The AMOOS 5B Configuration	30
3	The AMOOS HB Configuration with the Expansion Flap Deflected	31
4a	Drawings of the AMOOS HB and 5B Configurations	32
4b	AMOOS Flap Geometries	33
5	The AMOOS 5B Configuration with the Compression Flap Deflected	34
6	Rear View of the AMOOS HB Configuration	35
7	Axis Systems Showing Direction and Sense of Force and Moment Coefficients, Angle of Attack, and Sideslip Angle	36
8a	Comparison of Theoretical and Experimental Normal Force Coefficients for the 5B Configuration with Compression Flap Deflections	37
8b	Shadowgraph of the AMOOS 5B Configuration with a Compression Flap Deflection of $10^\circ$ at an Angle of Attack of $65^\circ$	38
8c	Comparison of Theoretical and Experimental Incremental Normal Force Coefficients for the 5B Configuration with Compression Flap Deflections	39

## LIST OF ILLUSTRATIONS (Continued)

<u>Figure</u>		<u>Page</u>
8d	Comparison of Theoretical and Experimental Axial Force Coefficients for the 5B Configuration with Compression Flap Deflections	40
8e	Comparison of Theoretical and Experimental Pitching Moment Coefficients for the 5B Configuration with Compression Flap Deflections	41
8f	Comparison of Theoretical and Experimental Incremental Pitching Moment Coefficients for the 5B Configuration with Compression Flap Deflections	42
8g	Comparison of Theoretical and Experimental Normal Force Coefficients for the 5B Configuration with Expansion Flap Deflections	43
8h	Comparison of Theoretical and Experimental Incremental Normal Force Coefficients for the 5B Configuration with Expansion Flap Deflections	44
8i	Comparison of Theoretical and Experimental Axial Force Coefficients for the 5B Configuration with Expansion Flap Deflections	45
8j	Comparison of Theoretical and Experimental Pitching Moment Coefficients for the 5B Configuration with Expansion Flap Deflections	46
8k	Comparison of Theoretical and Experimental Incremental Pitching Moment Coefficients for the 5B Configuration with Expansion Flap Deflections	47
8l	Plot of Incremental Normal Force Coefficients as Functions of Expansion Flap Deflection Angles for the 5B Configuration	48
8m	Plot of Incremental Pitching Moment Coefficients as Functions of Expansion Flap Deflection Angles for the 5B Configuration	49
9a	Comparison of Theoretical and Experimental Side Force Coefficients for the 5B Configuration with 0° Compression Flap Deflection	50
9b	Comparison of Theoretical and Experimental Yawing Moment Coefficients for the 5B Configuration with 0° Compression Flap Deflection	51

## LIST OF ILLUSTRATIONS (Continued)

<u>Figure</u>		<u>Page</u>
9c	Comparison of Theoretical and Experimental Rolling Moment Coefficients for the 5B Configuration with 0° Compression Flap Deflection	52
9d	Comparison of Theoretical and Experimental Side Force Coefficients for the 5B Configuration with 0° Expansion Flap Deflection	53
9e	Comparison of Theoretical and Experimental Yawing Moment Coefficients for the 5B Configuration with 0° Expansion Flap Deflection	54
9f	Comparison of Theoretical and Experimental Rolling Moment Coefficients for the 5B Configuration with 0° Expansion Flap Deflection	55
10a	Shadowgraph of the Basic (No Flap) HB Configuration at an Angle of Attack of 65°	56
10b	Comparison of Theoretical and Experimental Normal Force Coefficients for the HB Configuration with Compression Flap Deflections	57
10c	Shadowgraph of the HB Model with the Compression Flap Deflected 40° at a Model Angle of Attack of 30°	58
10d	Shadowgraph of the HB Model with the Compression Flap Deflected 40° at a Model Angle of Attack of 65°	59
10e	Comparison of Theoretical and Experimental Incremental Normal Force Coefficients for the HB Configuration with Compression Flap Deflections	60
10f	Comparison of Theoretical and Experimental Axial Force Coefficients for the HB Configuration with Compression Flap Deflections	61
10g	Comparison of Theoretical and Experimental Pitching Moment Coefficients for the HB Configuration with Compression Flap Deflections	62
10h	Comparison of Theoretical and Experimental Incremental Pitching Moment Coefficients for the HB Configuration with Compression Flap Deflections	63

## LIST OF ILLUSTRATIONS (Continued)

<u>Figure</u>		<u>Page</u>
10i	Comparison of Theoretical and Experimental Normal Force Coefficients for the HB Configuration with Expansion Flap Deflections	64
10j	Comparison of Theoretical and Experimental Incremental Normal Force Coefficients for the HB Configuration with Expansion Flap Deflections	65
10k	Comparison of Theoretical and Experimental Axial Force Coefficients for the HB Configuration with Expansion Flap Deflections	66
10l	Comparison of Theoretical and Experimental Pitching Moment Coefficients for the HB Configuration with Expansion Flap Deflections	67
10m	Comparison of Theoretical and Experimental Incremental Pitching Moment Coefficients for the HB Configuration with Expansion Flap Deflections	68
10n	Plot of Incremental Normal Force Coefficients as Functions of Expansion Flap Deflection Angles for the HB Configuration	69
10o	Plot of Incremental Pitching Moment Coefficients as Functions of Expansion Flap Deflection Angles for the HB Configuration	70
11a	Shadowgraph of the HB Model at a Model Sideslip Angle of $10^\circ$ with the Compression Flap Deflected	71
11b	Comparison of Theoretical and Experimental Side Force Coefficients for the HB Configuration with the Compression Flap Deflected $0^\circ$ at the Angles of Attack of $40^\circ$ , $45^\circ$ and $50^\circ$	72
11c	Comparison of Theoretical and Experimental Side Force Coefficients for the HB Configuration with the Compression Flap Deflected $40^\circ$ at the Angles of Attack of $40^\circ$ , $45^\circ$ and $50^\circ$	73
11d	Comparison of Theoretical and Experimental Yawing Moment Coefficients for the HB Configuration with the Compression Flap Deflected $0^\circ$ at the Angles of Attack of $40^\circ$ , $45^\circ$ and $50^\circ$	74
11e	Comparison of Theoretical and Experimental Yawing Moment Coefficients for the HB Configuration with the Compression Flap Deflected $40^\circ$ at the Angles of Attack of $40^\circ$ , $45^\circ$ and $50^\circ$	75



## LIST OF ILLUSTRATIONS (Continued)

<u>Figure</u>		<u>Page</u>
11f	Comparison of Theoretical and Experimental Rolling Moment Coefficients for the HB Configuration with the Compression Flap Deflected $0^\circ$ at the Angles of Attack of $40^\circ$ , $45^\circ$ and $50^\circ$	76
11g	Comparison of Theoretical and Experimental Rolling Moment Coefficients for the HB Configuration with the Compression Flap Deflected $40^\circ$ at the Angles of Attack of $40^\circ$ , $45^\circ$ and $50^\circ$	77
12a	Comparison of Theoretical and Experimental Side Force Coefficients for the HB Configuration with an Expansion Flap Deflection of $0^\circ$ at the Angles of Attack of $40^\circ$ , $45^\circ$ and $50^\circ$	78
12b	Comparison of Theoretical and Experimental Side Force Coefficients for the HB Configuration with an Expansion Flap Deflection of $-40^\circ$ at the Angles of Attack of $40^\circ$ and $50^\circ$	79
12c	Comparison of Theoretical and Experimental Yawing Moment Coefficients for the HB Configuration with an Expansion Flap Deflection of $0^\circ$ at the Angles of Attack of $40^\circ$ , $45^\circ$ and $50^\circ$	80
12d	Comparison of Theoretical and Experimental Yawing Moment Coefficients for the HB Configuration with an Expansion Flap Deflection of $-40^\circ$ at the Angles of Attack of $40^\circ$ and $50^\circ$	81
12e	Comparison of Theoretical and Experimental Rolling Moment Coefficients for the HB Configuration with an Expansion Flap Deflection of $0^\circ$ at the Angles of Attack of $40^\circ$ , $45^\circ$ and $50^\circ$	82
12f	Comparison of Theoretical and Experimental Rolling Moment Coefficients for the HB Configuration with an Expansion Flap Deflection of $-40^\circ$ at the Angles of Attack of $40^\circ$ and $50^\circ$	83
13a	Comparison of Theoretical and Experimental Side Force Coefficients for the HB Configuration with Compression Flap Deflections of $0^\circ$ and $40^\circ$ at an Angle of Attack of $40^\circ$	84

## LIST OF ILLUSTRATIONS (Continued)

<u>Figure</u>		<u>Page</u>
13b	Comparison of Theoretical and Experimental Side Force Coefficients for the HB Configuration with Compression Flap Deflections of $0^{\circ}$ and $40^{\circ}$ at an Angle of Attack of $45^{\circ}$	85
13c	Comparison of Theoretical and Experimental Side Force Coefficients for the HB Configuration with Compression Flap Deflections of $0^{\circ}$ and $40^{\circ}$ at an Angle of Attack of $50^{\circ}$	86
13d	Comparison of Theoretical and Experimental Yawing Moment Coefficients for the HB Configuration with Compression Flap Deflections of $0^{\circ}$ and $40^{\circ}$ at an Angle of Attack of $40^{\circ}$	87
13e	Comparison of Theoretical and Experimental Yawing Moment Coefficients for the HB Configuration with Compression Flap Deflections of $0^{\circ}$ and $40^{\circ}$ at an Angle of Attack of $45^{\circ}$	88
13f	Comparison of Theoretical and Experimental Yawing Moment Coefficients for the HB Configuration with Compression Flap Deflections of $0^{\circ}$ and $40^{\circ}$ at an Angle of Attack of $50^{\circ}$	89
13g	Comparison of Theoretical and Experimental Rolling Moment Coefficients for the HB Configuration with Compression Flap Deflections of $0^{\circ}$ and $40^{\circ}$ at an Angle of Attack of $40^{\circ}$	90
13h	Comparison of Theoretical and Experimental Rolling Moment Coefficients for the HB Configuration with Compression Flap Deflections of $0^{\circ}$ and $40^{\circ}$ at an Angle of Attack of $45^{\circ}$	91
13i	Comparison of Theoretical and Experimental Rolling Moment Coefficients for the HB Configuration with Compression Flap Deflections of $0^{\circ}$ and $40^{\circ}$ at an Angle of Attack of $50^{\circ}$	92
13j	Comparison of Theoretical and Experimental Side Force Coefficients for the HB Configuration with Expansion Flap Deflections of $0^{\circ}$ and $-40^{\circ}$ at an Angle of Attack of $40^{\circ}$	93
13k	Comparison of Theoretical and Experimental Side Force Coefficients for the HB Configuration with Expansion Flap Deflections of $0^{\circ}$ and $-40^{\circ}$ at an Angle of Attack of $50^{\circ}$	94

## LIST OF ILLUSTRATIONS (Concluded)

<u>Figure</u>		<u>Page</u>
13l	Comparison of Theoretical and Experimental Yawing Moment Coefficients for the HB Configuration with Expansion Flap Deflections of $0^{\circ}$ and $-40^{\circ}$ at an Angle of Attack of $40^{\circ}$	95
13m	Comparison of Theoretical and Experimental Yawing Moment Coefficients for the HB Configuration with Expansion Flap Deflections of $0^{\circ}$ and $-40^{\circ}$ at an Angle of Attack of $50^{\circ}$	96
13n	Comparison of Theoretical and Experimental Rolling Moment Coefficients for the HB Configuration with Expansion Flap Deflections of $0^{\circ}$ and $-40^{\circ}$ at an Angle of Attack of $40^{\circ}$	97
13o	Comparison of Theoretical and Experimental Rolling Moment Coefficients for the HB Configuration with Expansion Flap Deflections of $0^{\circ}$ and $-40^{\circ}$ at an Angle of Attack of $50^{\circ}$	98
14a	Comparison of Normal Force Coefficients for the HB Configuration with the Compression Flap Deflected $40^{\circ}$ at Two Different Reynolds Numbers	99
14b	Comparison of Axial Force Coefficients for the HB Configuration with the Compression Flap Deflected $40^{\circ}$ at Two Different Reynolds Numbers	100

NOMENCLATURE

<u>Symbol</u>	<u>Description</u>
$C_A$	total axial force coefficient, $F_A/q_\infty S_{ref}$ , positive in the negative direction of X (dimensionless)
$C_D$	drag force coefficient in the wind axis system, $F_D/q_\infty S_{ref}$ , positive in the negative direction of $X_w$ (dimensionless)
c.g.	abbreviation for center of gravity
$C_L$	lift force coefficient (stability or wind axis system), $F_L/q_\infty S_{ref}$ , positive in the negative direction of $Z_s$ or $Z_w$ (dimensionless)
$C_l$	rolling moment coefficient in the body axis system, $M_X/q_\infty S_{ref}l$ , (dimensionless)
$C_m$	pitching moment coefficient in the body axis system, $M_Y/q_\infty S_{ref}l$ , (dimensionless)
$C_N$	normal force coefficient (body axis system), $F_N/q_\infty S_{ref}$ , positive in the negative direction of Z (dimensionless)
$C_n$	yawing moment coefficient in the body axis system, $M_Z/q_\infty S_{ref}l$ , (dimensionless)
$C_p$	pressure coefficient = $\frac{p - p_\infty}{q_\infty}$ (dimensionless)
$C_Y$	side force coefficient (body or stability axis system), $F_Y/q_\infty S_{ref}$ , positive in the positive direction of Y (dimensionless)
$\Delta C_m$	incremental pitching moment coefficient defined as the pitching moment coefficient determined with flap deflection at a particular angle of attack minus the pitching moment coefficient with no flap deflection at the same angle of attack (dimensionless)
$\Delta C_N$	incremental normal force coefficient defined as the normal force coefficient determined with flap deflection at a particular angle of attack minus the normal force coefficient with no flap deflection at the same angle of attack (dimensionless)
$F_A$	axial force, positive in the negative direction of X (N, lb)

## NOMENCLATURE (Continued)

<u>Symbol</u>	<u>Description</u>
$F_D$	drag force in the wind axis system, positive in the negative direction of $X_w$ (N, lb)
$F_L$	lift force (stability or wind axis system), positive in the negative direction of $Z_s$ or $Z_w$ (N, lb)
$F_N$	normal force, positive in the negative direction of $Z$ (N, lb)
$F_Y$	side force, positive in the positive direction of $Y$ (N, lb)
$L/D$	lift-to-drag ratio, $C_L/C_D$ (dimensionless)
$l_{ref}$	reference length (body length) (m, ft)
$M$	Mach number (dimensionless)
$M_X$	rolling moment in the body axis system; i.e., moment about the X-axis (a positive rolling moment tends to rotate the positive Y-axis toward the positive Z-axis), (N-m, ft-lb)
$M_Y$	pitching moment in the body (or stability) axis system; i.e., moment about the Y-axis (a positive pitching moment tends to rotate the positive Z-axis toward the positive X-axis), (N-m, ft-lb)
$M_Z$	yawing moment in the body axis system; i.e., moment about the Z-axis (a positive yawing moment tends to rotate the positive X-axis toward the positive Y-axis), (N-m, ft-lb)
$p$	local static pressure ( $N/m^2$ , psi)
$p_o$	tunnel supply pressure ( $N/m^2$ , psi)
$p_\infty$	freestream static pressure ( $N/m^2$ , psi)
$q_\infty$	dynamic pressure, $\rho_\infty V_\infty^2/2$ ( $N/m^2$ , psi)
$Re_\infty/L$	freestream Reynolds number per unit length (1/m, 1/ft)
$S_{ref}$	reference area ( $m^2$ , $ft^2$ )
$T_o$	tunnel supply temperature ( $^{\circ}K$ , $^{\circ}R$ )
$T_\infty$	freestream static temperature ( $^{\circ}K$ , $^{\circ}R$ )

## NOMENCLATURE (Concluded)

<u>Symbol</u>	<u>Description</u>
$V_{\infty}$	freestream airspeed or speed of the aircraft relative to the surrounding atmosphere (m/sec, ft/sec)
X, Y, Z	body axis system coordinates (the X, Z-plane is the plane of symmetry and the origin of the axis system is the center of gravity, center of mass, or any other convenient point) (m, ft)
<u>Greek</u>	
$\alpha$	angle of attack, angle between the projection of the wind $X_w$ -axis on the body X, Z-plane and the body X-axis (deg)
$\beta$	sideslip angle, angle between the wind $X_w$ -axis and the projection of this axis on the body X, Z-plane (deg)
$\delta$	flap deflection angle, positive when the trailing edge is deflected down (deg)
$\rho_{\infty}$	freestream air density (kg/m <sup>3</sup> , slug/ft <sup>3</sup> )

## Section 1

## INTRODUCTION AND SUMMARY

An orbit-to-orbit transfer vehicle will be an essential element of the future space transportation system required to accomplish the NASA mission spectrum. The orbit-to-orbit vehicle is designed to operate as a third stage for the two-stage space shuttle. Past studies have defined vehicle systems which are capable of performing a large number of NASA missions by using propulsive maneuvers in vacuum only. However, the accomplishment of high energy missions such as payload transfer to and from synchronous orbit exceeds the capabilities of most of the proposed vehicle systems which have the disadvantage of large sensitivity to small inert weight changes and specific impulse variations. To reduce the sensitivity and improve the payload capability of the transfer vehicle, the utilization of atmospheric entry and exit passes may be an attractive alternate mode of mission operation due to the possible trading of propulsion requirements for aerodynamic forces for aerobraking and aeromaneuvering. The proposed direct-entry mode applicable to the aeromaneuvering orbit-to-orbit shuttle (AMOOS) vehicle at the associated high velocities, while offering a reduction in propulsion requirements, has the adverse effects of: (1) encountering the entry heating environment, and (2) encountering aerodynamic loads on the vehicle. Aerodynamic characteristics have been estimated for preliminary AMOOS configurations (Ref. 1) using the Hypersonic Arbitrary Body Aerodynamic Computer Program (Gentry Program), Ref. 2. Newtonian theory is employed in this program as the fundamental technique for calculating continuum flow hypersonic aerodynamics. Justification for the use of Newtonian theory is presented in Appendix A. The complex geometries of the candidate AMOOS configurations, in conjunction with control surface deflections, result in intricately varying flow regimes surrounding the AMOOS vehicle. Newtonian flow theory can only approximate the aerodynamics of AMOOS vehicles because of the limitations of its basic assumptions. Wind tunnel tests are necessary to establish the validity of the Newtonian theory estimates so that reliable data are available for future AMOOS studies.

An aerodynamic wind tunnel investigation was conducted in the NASA-Ames Research Center (ARC) 3.5-foot hypersonic facility to provide data for use in obtaining experimental force and static stability characteristics of two potential AMOOS vehicle configurations. Another objective of this report was to compare the experimental data with the aerodynamic characteristics estimated using Newtonian theory, thus establishing the usefulness of these predictions.

The candidate AMOOS configurations selected for the wind tunnel tests were the AMOOS 5B and HB configurations. Two flap configurations were tested for each candidate — a forward or compression surface flap and an aft or expansion flap. Photographs and sketches of the two configurations with different control surfaces are shown in Figs. 1 through 6.

Specifically, the objectives of the wind tunnel test were to:

1. Obtain aerodynamic force and static stability characteristics of two candidate configurations, and
2. Determine flap effectiveness.

Typically, test parameters covered the following ranges:

Mach number:	10.27
Angle of Attack:	30 to 65 degrees
Sideslip Angle:	-2 to 10 degrees
Flap Deflection Angle:	0 to <u>+40</u> degrees
Reynolds number/foot:	$6.5 \times 10^5$ to $1.3 \times 10^6$

It was determined that Newtonian theory generally predicted the aerodynamics of the 5B configuration with acceptable accuracy for all expansion flap deflections and for compression flap deflections less than or equal to 10 degrees. Flow separation upstream of large compression flap deflections was detected from the experimental data. Newtonian theory could not predict this phenomenon because of the limitations of the assumptions employed in



its derivation. The agreement between the analytical and experimental data for the HB configuration was not as favorable as that for the 5B configuration. Both configurations indicated positive longitudinal, lateral, and roll stability with expansion flap deflections.

## Section 2

### TEST INFORMATION

This section includes a description of the test facility, models and test apparatus used in this investigation. Also the test conditions, data reduction techniques and data accuracy are discussed. This information was obtained from Refs. 3 and 4.

#### 2.1 TEST FACILITY

The Ames 3.5-foot hypersonic wind tunnel is a closed-circuit blowdown type tunnel capable of operating at nominal Mach numbers of 5, 7 and 10 at pressures to  $12,410,496 \text{ N/m}^2$  (1800 psia) and temperatures to  $1333^\circ\text{K}$  ( $2400^\circ\text{R}$ ) for run times to four minutes. The major components of the facility include a gas storage system where the test gas is stored at  $20,684,160 \text{ N/m}^2$  (3000 psi), a storage heater filled with aluminum-oxide cored brick capable of heating the test gas to  $1333^\circ\text{K}$  ( $2400^\circ\text{R}$ ), contoured nozzles with exit diameters of 1.067 m (42 in.) for generating the desired Mach number, and a  $25,485 \text{ m}^3$  ( $900,000 \text{ ft}^3$ ) vacuum storage system which operates to pressures of  $2068.4 \text{ N/m}^2$  (0.3 psia). The test section is an open-jet type enclosed within a chamber approximately 3.66 m (12 ft) in diameter and 12.19 m (40 ft) in length, arranged transversely to the flow direction. The length of the jet is approximately 3.05 m (10 ft) (Ref. 3).

A data acquisition system accepts analog signals at rates up to 2500 samples per second, converts them into digital form, and records on magnetic tape for later reduction by a digital computer.

#### 2.2 TEST CONDITIONS

The nominal test conditions were set for a tunnel supply pressure of  $8,272,800 \text{ N/m}^2$  (1200 psi) and a tunnel supply temperature of  $1111.1^\circ\text{K}$

(2000<sup>0</sup>R). These conditions resulted in a unit Reynolds number which closely matched that attained by a full scale AMOOS vehicle at the perigee point of a one pass mission (Ref. 1). Trajectory simulations have indicated that the drag force is largest at the perigee. Since the primary aerodynamic forces occur near the perigee, it was essential to simulate the corresponding flow conditions in the wind tunnel tests. Also, since the proposed AMOOS vehicle will be operating near  $C_{L_{max}}$  to compensate for atmospheric density variations, the experimental data were obtained at and surrounding the  $C_{L_{max}}$  range for the two vehicles with different control surfaces.

### 2.3 MODEL DESCRIPTION

The models tested were two 0.018-scale force models of the AMOOS 5B and HB configurations (Figs. 2, 3 and 4). The two force models were constructed of 17-4 PH stainless steel. Two flap configurations were fabricated for each model. A compression or forward body flap was built for the undersides of both configurations. Also, an expansion or aft flap, hinged at the base, was built for each model. The compression flap could be manually positioned at angles of 0, 10, 20 and 40 degrees while the expansion flap could be positioned at 0, -10, -20 and -40 degrees. Flap deflection settings for both flaps were achieved by preset angle wedges upon which the flaps were bolted. The sign convention employed was such that a downward flap deflection from the horizontal was positive. A photograph of the 5B configuration with no flap is presented as Fig. 2. Figure 5 shows the 5B configuration with the compression flap deflected.

### 2.4 TEST APPARATUS

A model support system (Fig. 1) was provided that could pitch models through an angle-of-attack range of -20 to +18 degrees, in a vertical plane, about a fixed point of rotation on the tunnel centerline. This rotation point was set at 0.597 m (23.5 in.) from the nozzle exit plane. The model normally was out of the test stream (strut centerline 0.94 m (37 in.) from tunnel centerline) until the tunnel test conditions were established after which it was inserted.

Insertion time was adjustable to a minimum of 1/2 second and the models were inserted at any strut angle. Closed-circuit video system with a recorder was available for visually monitoring the experiments within the test cabin. The Lockheed-Huntsville double knuckle sting, designed to support the 0.018-scale AMOOS models, was used for each investigation. By setting the sting at a prebent angle of 50 degrees, and then pitching the sector from -20 to +15 degrees, angles of attack from 30 to 65 degrees were obtained. Also, by rolling the sting assembly 90 degrees from the pitch plane, sweeps in the yaw plane were performed through sideslip angles of -2 to 10 degrees. These sweeps were obtained at angles of attack of 40, 45 and 50 degrees by setting the sting at these three prebent angles. Identifying numbers for the Lockheed-Huntsville double knuckle sting and associated equipment detail drawings are listed in Table 1. Figure 1 shows the sting assembly installed in the ARC 3.5-foot tunnel. Because of the tunnel high temperature environment and the necessity of providing thermal protection for the balance lead wires, a protective shroud of asbestos cloth and copper plating was banded around the sting assembly, as shown in Figs. 3 and 6.

Task Mk XLI-A and Mk XVIII six-component internal strain gage balances were used in the tests. These balances are 0.019 m (0.75 in.) in maximum diameter and 0.097 m (3.83 in.) in length. Maximum load capacities are shown in Tables 2 and 3.

Shadowgraphs of the flow field were obtained for flow visualization. The shadowgraphs were taken at 10 degree angle-of-attack increments for each sweep in the pitch plane and at 4 degree sideslip increments in the yaw plane.

## 2.5 DATA REDUCTION AND ACCURACY

Force and moment output from the respective balances in each test was recorded for each run. The recorded data were corrected for balance interactions and weight tares. Model angles of attack and sideslip were corrected for static balance and sting deflections. Corrected force and moment data were reduced to coefficient form using the reference dimensions presented in Table 4.

The six-component balance data were reduced in the body axis system shown in Fig. 7. The measured forces were non-dimensionalized to coefficient form as follows:

$$C_A = \frac{F_A}{q_\infty S_{ref}} \quad \text{total axial force coefficient}$$

$$C_l = \frac{M_X}{q_\infty S_{ref} l_{ref}} \quad \text{rolling moment coefficient}$$

$$C_m = \frac{M_Y}{q_\infty S_{ref} l_{ref}} \quad \text{pitching moment coefficient}$$

$$C_N = \frac{F_N}{q_\infty S_{ref}} \quad \text{normal force coefficient}$$

$$C_n = \frac{M_Z}{q_\infty S_{ref} l_{ref}} \quad \text{yawing moment coefficient}$$

$$C_Y = \frac{F_Y}{q_\infty S_{ref}} \quad \text{side force coefficient}$$

$$C_D = \frac{F_D}{q_\infty S_{ref}} \quad \text{drag force coefficient}$$

$$C_L = \frac{F_L}{q_\infty S_{ref}} \quad \text{lift force coefficient}$$

$$L/D = C_L / C_D \quad \text{lift-to-drag ratio}$$

Note that the same reference area,  $S_{ref}$ , was used to obtain all coefficients and the same reference length,  $l_{ref}$ , was used to obtain all moment coefficients. The coefficient accuracies for the two Task balances are presented in Table 5.

### Section 3

## RESULTS AND DISCUSSION

The completed test schedule consisted of force tests of both the AMOOS 5B and HB configurations and one Reynolds number variation test. The order in which the tests were performed is presented in Table 6. No attempt was made to compare the aerodynamics of the AMOOS 5B and the HB vehicles since that task is a requirement under a separate contract (NAS8-28586) entitled "Feasibility and Tradeoff Study of an Aeromaneuvering Orbit-to-Orbit Shuttle (AMOOS)."

Theoretical continuum flow aerodynamics were derived for each configuration using the Hypersonic Arbitrary-Body Aerodynamic Computer Program (Gentry Program), (Ref. 2). Newtonian impact theory was employed to compute the aerodynamics on the windward side of the vehicles, and a pressure coefficient ( $C_p$ ) equal to zero (as required by Newtonian theory) was used to calculate the forces on the leeward side of the vehicles. No viscous effects were included due to the inviscid flow assumption made for Newtonian theory. All moment coefficients were reduced about the c.g. locations listed in Table 4. Curves have been faired through the theoretical data to differentiate those data from the experimental data.

Section 3.1 contains a comparison of the experimentally determined AMOOS 5B data with the theoretical predictions. Section 3.2 presents a comparison of the experimental HB data with theoretical predictions. In Section 3.3 the effect of a variation of Reynolds number on the experimental data is discussed.

### 3.1 COMPARISON OF AMOOS 5B EXPERIMENTAL DATA WITH THEORY

Presented in Figs. 8 and 9 are plots comparing the experimental aerodynamic coefficients and the coefficients computed using Newtonian theory for the AMOOS 5B configuration.

Figure 8a is a comparison of the theoretical and experimental normal force coefficients for the AMOOS 5B configuration with compression flap deflections. Very good agreement is seen for the basic (no flap) configuration. The slight overprediction by the theoretical model is probably due to the inaccuracy of the calculation of the pressure distribution around the nose of the vehicle. Good agreement is also seen for the case of the 20 degree flap deflection except at very high angles of attack. Flow separation ahead of the deflected flap is most likely causing the normal force to drop off at the higher angles of attack. Poorer agreement with theory is viewed for the experimental data for a flap deflection of 10 degrees over the entire angle of attack range. Since the likelihood of flow separation for a flap deflection of 10 degrees is slight, it must be assumed that the experimental data are somewhat low for that condition. Figure 8b is a shadowgraph of the AMOOS 5B configuration with a flap deflection of 10 degrees at an angle of attack of 65 degrees.

Figure 8c is a plot of the incremental normal force coefficient as a function of angle of attack for the 5B configuration for compression flap deflections. The incremental normal force coefficient is defined in the nomenclature.

A loss of flap effectiveness for the 20 degree deflection case is evident as the curve converges to the 10-degree deflection case at high angles of attack. Agreement with theory is good for the 20-degree deflection case for moderate to large angles of attack. The agreement between the experimental and theoretical data for the 10-degree deflection case is very poor, however, which further suggests that the experimentally determined normal force coefficient for a compression flap deflection of 10 degrees is low.

The theoretical and experimental axial force coefficients for the 5B configuration for compression flap deflections are presented in Fig. 8d. Note that the axial force increases with increasing flap deflection. The agreement of the experimental data with theory is good for the case of 0-degree flap deflection. For 10-degree flap deflections, however, the agreement with theory becomes poorer as the program underpredicts the axial force. The experimental axial force coefficients are higher because as the flap is deflected, it rotates closer to the bow shock curving around the body. The associated higher pressures cannot be predicted by Newtonian theory, resulting

in the underprediction as seen from the curves. For the case of 20-degree flap deflection, Newtonian theory overpredicts the axial force at high angles of attack since flow separation cannot be predicted by the theoretical model because of the limitations in its assumptions.

Figure 8e is a plot of experimental and theoretical pitching moment coefficients for the 5B configuration with compression flap deflections. The curves representing different flap deflections indicate that the no flap or 0-degree deflection case has the greatest longitudinal stability. For the 20-degree deflection case, evidence of flow separation and loss of flap effectiveness is seen in the flattening out of the moment curve. Agreement with theory for larger flap deflections is poor because the Newtonian theory overpredicts the normal force and underpredicts the axial force.

The incremental pitching moment coefficients for the 5B configuration with compression flap deflections are presented as Fig. 8f. The flap effectiveness decreases with increasing angle of attack. Evidence of flow separation is seen as the curve representing the case of 20-degree flap deflection converges to the curve for 10-degree deflection at high angles of attack. Poor agreement with theory is evident as was determined from examining the pitching moment coefficient curves (Fig. 8e) for flap deflections greater than 0 degrees.

A comparison of the theoretical and experimental normal force coefficients determined for the 5B configuration for expansion flap deflections is presented as Fig. 8g. Agreement of the data is favorable over the entire angle of attack range as far as the trend of the data is concerned. The magnitude of the theoretical data is approximately 10% higher than the experimental data for the three flap deflections. The overprediction by the theoretical model is probably due to the inaccuracy of the calculation of the pressure distribution around the nose of the vehicle, and the failure of the theoretical model to account for flow over the top surface of the expansion flap, which results in a negative normal force component. Better quality shadowgraphs and pressure distribution data are needed to verify these assumptions.



Figure 8h is a plot of incremental normal force coefficients as functions of angle of attack for the 5B model with expansion flap deflections. Increasing flap effectiveness with increasing angle of attack is noted for all flap deflections. The curves indicate that the 0-degree flap deflection condition is the most effective case. The theoretical model overpredicts the flap effectiveness because flow over the top surface of the flap is not considered.

A comparison of the theoretical and experimental axial force coefficients for the 5B configuration for expansion flap deflections is made in Fig. 8i. The experimental data indicate that the axial force decreases with increasing negative flap deflections as was predicted by theory. The measured axial force peaks for all flap deflections at lower angles of attack and is larger in magnitude for all flap deflections than theory predicted. These trends are again probably due to the previously mentioned effect of the flow over the top surface of the expansion flap and to the viscous drag contribution.

Figure 8j is a plot of pitching moment coefficient as a function of angle of attack for the 5B configuration with expansion flap deflections. The curves representing all three flap deflections (0, -10 and -20 degrees) indicate positive longitudinal stability. Agreement between the theoretical prediction and the experimental data is excellent for the case of 0-degree flap deflection except at high angles of attack. Poor agreement between the theoretical and experimental data is also seen for the -10-degree and -20-degree flap deflections. The deviations in the theoretical and experimental moment curves for these flap deflections are due to the inability of Newtonian flow to accurately predict the normal and axial force coefficients for the previously mentioned reasons.

Figure 8k presents the incremental pitching moment coefficients determined for the 5B configuration for expansion flap deflections. The curves reflect the expected trends determined from the total pitching moment plots.

Figures 8l and 8m are plots of incremental normal force and pitching moment coefficients, respectively, replotted as functions of expansion flap deflection angles.

Theoretical and experimental side force coefficients as functions of sideslip angle are plotted in Fig. 9a for the 5B configuration with 0-degree compression flap deflection at angles of attack of 40, 45 and 50 degrees. The side force increases with angle of attack as the projected area of the model normal to the flow increases. Newtonian theory overpredicts the side force because the pressure distribution around the 5B nose is not accurately calculated. The experimental data curves do not pass through the origin of the axis system most likely because of undefined flow angularity and possible model warpage due to heating.

Figure 9b presents a plot of yawing moment coefficient as a function of sideslip angle for the 5B configuration with 0-degree compression flap deflection at angles of attack of 40, 45 and 50 degrees. The experimental data indicate positive directional stability and increased stability with increasing angle of attack. This result is due to the increase in side force and axial force with increasing angle of attack. The theoretical prediction shows favorable agreement with the experimental data for these angles of attack despite the underpredictions of the axial force (see Fig. 8d) which caused a slight underprediction of the yawing moment.

Theoretical and experimental rolling moment coefficients as functions of sideslip angle are plotted in Fig. 9c for the 5B configuration with 0-degree compression flap deflection. The curves indicate that there is little variation in the rolling moment coefficient with angle of attack. The slopes of the curves indicate positive roll stability. Again, tunnel flow angularity and model warpage due to the high temperatures are probable explanations as to the failure of the experimental data to pass through the origin of the plot.

A plot of side force coefficient as a function of sideslip angle for the 5B configuration with the expansion flap deflected 0 degrees at model angles of attack of 40, 45 and 50 degrees is presented as Fig. 9d. The trend of increasing side force as a function of sideslip angle with increasing angle of attack is due to the increase in the projected area normal to the flow as angle of attack is increased. A comparison of the experimental data with

the theoretical data indicates that the computer program overpredicts the side force, probably because of its inability to accurately predict the pressure distribution around the 5B nose. Tunnel flow angularity and slight model warpage due to the high temperatures causing body asymmetry are probable causes for the slight side forces measured at zero sideslip angle.

Figure 9e is a plot of yawing moment coefficient versus sideslip angle for the 5B configuration with the expansion flap deflected 0 degrees and at angles of attack of 40, 45 and 50 degrees. All three curves reflect positive directional stability and the stability improves with increasing angle of attack. The theoretical data underpredict the yawing moment measured experimentally because Newtonian theory considerably underpredicted the axial force at angles of attack of 40, 45 and 50 degrees.

A comparison of the theoretical and experimental rolling moment coefficients for the 5B configuration with the expansion flap deflected 0 degrees at angles of attack of 40, 45 and 50 degrees is presented as Fig. 9f. There is little variation with angle of attack. The slopes of the curves indicate positive roll stability. The experimental data do not pass through the origin because of tunnel flow angularity and model warpage due to high heating.

### 3.2 COMPARISON OF AMOOS HB EXPERIMENTAL DATA WITH THEORY

In Figs. 10, 11 and 12, plots comparing the experimental aerodynamic coefficients and the coefficients computed using Newtonian theory for the AMOOS HB configuration are presented. A shadowgraph of the basic (no flap) HB configuration is presented as Fig. 10a. The bow shock is parallel and close to the body as would be expected for hypersonic flow.

A comparison of the experimental and theoretical normal force coefficients for the AMOOS HB configuration with varying compression flap deflections is shown as Fig. 10b. Reasonable agreement between the theoretical and experimental data is seen for the basic (no flap) condition. The theoretical method overpredicts the normal force on the HB vehicle, but the trend of the

theoretical normal force coefficients curve is similar to that for the experimental data. The overprediction of the normal force on the HB vehicle is most likely due to the extreme bluntness of the HB nose causing relatively large areas of subsonic flow around the nose as a result of a strong detached bow shock. The associated pressures cause expansions to occur around the sides of the vehicle onto the lee side of the model resulting in a negative normal force component. Newtonian theory cannot predict such occurrences because a pressure coefficient equal to zero is required on the lee side of the vehicle in the shadow of the flow.

For increasing flap deflection, the analytical model computes a consistent increase of normal force with angle of attack until a deflection of 40 degrees is reached. The experimental data, however, show a loss of normal force at moderate to high angles of attack for flap deflections of 20 and 40 degrees. Separation of the flow upstream of the flap causes the loss of normal force at the high angles of attack. Figure 10c is a shadowgraph of the 40 degree compression flap at a model angle of attack of 30 degrees. The bow shock shows no tendency to curve away from the model surface until it intersects the shock emanating from the hinge line of the flap. A shear layer resulting from the shock-shock interaction impinges upon the flap. Figure 10d is a shadowgraph of the same flap deflection at an angle of attack of 65 degrees. The bow shock begins to curve away from the model surface ahead of the deflected flap suggesting flow separation.

Figure 10e presents a plot of incremental normal force coefficient as a function of angle of attack. The incremental normal force coefficient is defined in the nomenclature.

The experimental data show a loss of normal force occurring for all angles of attack with flap deflections of 20 and 40 degrees. The theoretical predictions of the incremental normal force coefficients are consistently low for all flap deflections and only the trend is accurately predicted for the case of a 40-degree flap deflection.

A comparison of the theoretical and experimental axial force coefficients for the HB configuration with compression flap deflections is shown as Fig. 10f. For the case of zero flap deflection, Newtonian theory slightly overpredicts the axial force despite its inviscid flow assumption. This is probably due to the inability of the theoretical model to accurately predict the pressure distribution around the blunt nose of the HB configuration. Investigators of space shuttle type aerodynamics have discovered similar comparisons of theoretical and experimental axial force data (Ref. 5). For the higher flap deflections, the theoretical predictions are much larger than the experimental data indicating the inability of Newtonian theory to predict flow separation.

Figure 10g, which is a plot of pitching moment coefficient as a function of angle of attack, also illustrates the inability of Newtonian theory to predict the loss of flap effectiveness due to flow separation. The experimental data for the basic (no flap) configuration indicate that the vehicle is longitudinally stable. For increasingly larger compression flap deflections, however, the vehicle becomes neutrally and finally negatively stable longitudinally. An examination of the analytical data shows that Newtonian theory did not predict the loss of longitudinal stability.

Figure 10h presents a plot of incremental pitching moment coefficient versus angle of attack for compression flap deflections. A loss of flap effectiveness is evident by the tendency of the increments to converge to zero as angle of attack is increased. Agreement between the experimental and theoretical data is again poor.

A comparative plot of theoretical and experimental normal force coefficients for the HB vehicle with expansion flap deflections is shown in Fig. 10i. The experimental data show the expected trend of decreasing normal force with increasingly negative flap deflections. This trend can be explained by the fact that as the flap is deflected negatively, it becomes shaded from the flow by the body. An anomaly in this trend appears for the -10-degree deflection. The normal force is higher for this condition than for the 0-degree deflection. No satisfactory explanation of this anomaly may be made from the present

data resources. More detailed shadowgraphs and pressure distribution data are required to verify the anomaly and to aid in its explanation. The curves representing the theoretical predictions show that Newtonian theory overpredicted the normal force on the HB configuration as was previously explained for the 5B configuration.

Figure 10j is a plot of incremental normal force coefficient versus angle of attack for the HB vehicle with expansion flap deflections.

A comparison of theoretical and experimental axial force coefficients for the HB vehicle with expansion flap deflections is presented as Fig. 10k. The overprediction is due to the same reason as was explained for compression flap deflections.

Figure 10l is a comparison of experimental and theoretical pitching moment coefficients for the HB configuration for expansion flap deflections. Reasonably good agreement with theory is evident for this flap for all deflection angles. The slopes of all the curves indicate that the HB vehicle for any expansion flap deflection is definitely longitudinally stable. No evidence of flow separation is apparent.

A comparison of experimental and theoretical incremental pitching moment coefficients for the HB configuration for expansion flap deflections is presented as Fig. 10m. Good agreement with theory is evident for this flap for all flap deflections. This is probably due to the fact that the effect of the nose has been eliminated in computing the pitching moment increment for each flap deflection. The slopes of the curves indicate that the aft flap becomes more effective with increasing angle of attack and for less negative deflections.

Figures 10n and 10o are plots of incremental normal force and pitching moment coefficients, respectively, as functions of expansion flap deflection angles.

Figure 11a is a shadowgraph of the HB configuration, with the compression flap deflected, yawed at a sideslip angle of 10 degrees. Two shock patterns are observed — the main bow shock and the secondary shock off the deflected compression flap.

Figures 11b and 11c are plots of side force coefficients as functions of sideslip angle for angles of attack of 40, 45 and 50 degrees for compression flap deflections of 0 and 40 degrees, respectively. The trend of increasing side force as a function of sideslip angle with increasing angle of attack is as expected since the projected area of the vehicle normal to the flow increases as angle of attack is increased.

Figures 11d and 11e are plots of yawing moment coefficients as functions of sideslip angle for angles of attack of 40, 45 and 50 degrees for compression flap deflections of 0 and 40 degrees, respectively. The slopes of the curves indicate positive directional stability. Figure 11d, which represents the no flap condition, shows the expected trend of increasing yawing moment with increasing angle of attack since the side force and axial force increased with angle of attack. Figure 11e, which represents the condition for a 40-degree compression flap deflection, however, does not show the same trend. The yawing moment coefficients for angles of attack of 40 and 45 degrees are higher than that for an angle of attack of 50 degrees. This change in the trend may be explained by referring to Fig. 10f, which is a plot of axial force coefficient as a function of angle of attack. It can be seen that for the curve representing the 40-degree compression flap deflection, the axial force falls off sharply for moderate angles of attack. The result is that although the side force did increase with increasing angle of attack, the axial force actually decreased substantially causing lower yawing moment coefficients.

Plots of rolling moment coefficients as functions of sideslip angle for angles of attack of 40, 45 and 50 degrees are presented as Figs. 11f and 11g. The slopes of the curves indicate that the HB vehicle has positive roll stability. Both figures show the expected trend of increasing rolling moment with increasing angle of attack.

Plots of side force coefficients as functions of sideslip angle for an expansion flap deflection of 0 degrees at angles of attack of 40, 45 and 50 degrees and for a flap deflection of -40 degrees at angles of attack of 40 and 50 degrees are presented as Figs. 12a and 12b, respectively. For increasing angle of attack, there is a corresponding increase in side force coefficient. As was seen for the cases of compression flap deflections, Newtonian theory overpredicts the side force.

Figures 12c and 12d are plots of yawing moment coefficients as functions of sideslip angle for an expansion flap deflection of 0 degrees at angles of attack of 40, 45 and 50 degrees and for a flap deflection of -40 degrees at angles of attack of 40 and 50 degrees, respectively. In Fig. 12c, the experimental data curves representing the three angles of attack almost coincide. Figure 12d, which is a similar plot for the -40 degree flap deflection, shows the same trend. This relationship is due to the very slight effect the variation of angle of attack has on the side and axial force coefficients for expansion flap deflections.

Plots of rolling moment coefficients versus sideslip angle for an expansion flap deflection of 0 degrees at angles of attack of 40, 45 and 50 degrees and for a deflection of -40 degrees at angles of attack of 40 and 50 degrees, respectively, are shown as Figs. 12e and 12f. The curves indicate that the AMOOS HB configuration with expansion flap deflections has better roll stability at the higher angles of attack.

Comparative plots of side force coefficients, yawing moment coefficients, and rolling moment coefficients for the HB configuration with both compression and expansion flap deflections are plotted in Fig. 13. These data are the same as were plotted in Figs. 11 and 12; however, the coefficients are plotted for a constant angle of attack with varying flap deflection.



### 3.3 EFFECTS OF REYNOLDS NUMBER VARIATION ON THE EXPERIMENTAL DATA

Due to test time limitations, only one run was made to examine the effect of Reynolds number variation on the experimental data. The configuration tested was the AMOOS HB model with the compression flap deflected 40 degrees. The larger unit Reynolds number at which the model was tested was approximately  $1.2 \times 10^6$  while the smaller was  $6.0 \times 10^5$ , and the actual run numbers were 16 and 25, respectively (see Table 6). Figure 14a is a plot comparing normal force coefficients versus angle of attack for the two Reynolds number conditions. There is virtually no difference in normal force coefficient for the two cases; the maximum difference between the two curves amounts to 0.2%. Figure 14b presents a plot of axial force coefficients as a function of angle of attack for the two Reynolds number conditions. The plot shows that the axial force measured for the lower Reynolds number condition was 2.0 to 4.0% higher than that measured at the higher Reynolds number. This increase in axial force is probably due to the increase in skin friction because of the lower Reynolds number. For laminar flow, the skin friction coefficient is proportional to  $1/\sqrt{\text{Re}/ft}$  (Ref. 6). Halving the Reynolds number would result in approximately a 41% increase in the skin friction coefficient. Such an increase in the skin friction can account for the 2.0 to 4.0% increase in axial force.

Section 4  
CONCLUSIONS

An experimental investigation was conducted in the ARC 3.5-Foot Hypersonic Wind Tunnel to determine the aerodynamic force and static stability characteristics of two potential AMOOS vehicle configurations. Comparisons between the experimental data and the theoretical data predicted by Newtonian theory were made in Section 3. Based upon the data contained in this report, the following conclusions are presented:

1. Newtonian theory predicted the aerodynamics of the AMOOS 5B configuration with acceptable accuracy except for compression flap deflections greater than 10 degrees.
2. The agreement between the analytical data and the experimental data for the AMOOS HB configuration was not as favorable as that for the 5B configuration because Newtonian theory did not accurately compute the pressure distribution around the blunt HB nose.
3. The AMOOS HB and 5B configurations have positive longitudinal stability for all expansion flap deflections.
4. Both the AMOOS HB and 5B configurations have positive directional stability for both flap configurations at angles of attack near those corresponding to  $C_{L_{max}}$ .
5. Both the AMOOS HB and 5B configurations have positive roll stability for deflections of both flaps at angles of attack near those corresponding to  $C_{L_{max}}$ .

Section 5  
RECOMMENDATIONS

Based upon the experience and results obtained, the following recommendations are made regarding future tests:

1. Because of data fluctuations, it is suggested that the basic (no flap) configuration runs be repeated to ensure the validity of the experimental data for the baseline cases.
2. Because of the evidence of flow separation upstream of the deflected compression flap and the resulting loss of flap effectiveness, it is recommended that this flap no longer be considered as a potential flap configuration for the AMOOS vehicle.
3. It is suggested that the present shadowgraph system in the ARC 3.5-Foot Hypersonic Wind Tunnel be improved so that better quality shadowgraphs may be obtained.
4. Base pressure taps and forebody static pressure ports are recommended for consideration in future AMOOS wind tunnel models to aid in the prediction of base pressure effects and flow separation.
5. Oil flow photographs should be considered for future tests to determine flow separation and transition points on the AMOOS models.
6. It is suggested that the effects of Reynolds number variation on control surface effectiveness be investigated in future tests.

## REFERENCES

1. Andrews, C. D., "Feasibility and Tradeoff Study of an Aeromaneuvering Orbit-to-Orbit Shuttle (AMOOS)," LMSC-HREC TR D306600, Lockheed Missiles & Space Company, Huntsville, Ala., June 1973.
2. Gentry, A. E., "Hypersonic Arbitrary-Body Aerodynamic Computer Program, Mark III Version," Vols. 1 and 2, DAC 61552, Douglas Aircraft Co., Santa Monica, Calif., April 1968.
3. Ames Research Center, Staff Experimental Fluid Dynamics Branch, "Test Planning Information for the NASA-Ames 3.5-Foot Hypersonic Wind Tunnel," December 1972.
4. Ketter, F. C., "Pretest Report for Tests to Determine the Aerodynamic Characteristics of Two Potential Aeromaneuvering Orbit-to-Orbit Shuttle (AMOOS) Vehicle Configurations in the NASA-Ames 3.5-Foot Hypersonic Wind Tunnel," LMSC-HREC TB D306791, Lockheed Missiles & Space Company, Huntsville, Ala., October 1973.
5. Arrington, James P., and David R. Stone, "Aerodynamic and Flow-Visualization Studies of Two Delta-Wing Entry Vehicles at a Mach Number of 20.3," NASA TN D-7283, August 1973.
6. Schlichting, H., Boundary Layer Theory, McGraw-Hill, New York, 1960.

Table 1  
DETAIL DRAWINGS OF THE AMOOS MODELS  
AND STING ASSEMBLY

Part Description	Drawing Number
AMOOS 5B Model	R72 134
AMOOS HB Model	R72 135
Sting Mount	R72 137
Double Clevis	R72 138
Balance Mount	R72 139
Sting Adapter	R72 136
Sting Assembly	R72 141
Thermal Model	RT2 134

NOTE: These drawings were made by the Lockheed Missiles & Space Company, Huntsville Research & Engineering Center for Contract NAS8-28608 and may be supplied upon request following receipt of approval from MSFC

Table 2  
MAXIMUM BALANCE LOADS  
(TASK MK XLI-A)  
USED DURING AMOOS 5B TESTS

Normal Force	889.6 N (200 lb <sub>f</sub> )
Side Force	444.8 N (100 lb <sub>f</sub> )
Axial Force	148.3 N ( 30 lb <sub>f</sub> )
Rolling Moment	11.30 N-m (100 in-lb <sub>f</sub> )

NOTE: There are 0.076 m (3.0 in.) between the two 444.8 N (100 lb<sub>f</sub>) normal force gages and 0.0635 m (2.5 in.) between the two 222.4 N (50 lb<sub>f</sub>) side force gages.

Table 3  
 MAXIMUM BALANCE LOADS  
 (TASK MK XVIII)  
 USED DURING AMOOS HB TESTS

Normal Force	889.6 N (200 lb <sub>f</sub> )
Side Force	444.8 N (100 lb <sub>f</sub> )
Axial Force	296.6 N ( 60 lb <sub>f</sub> )
Rolling Moment	6.78 N-m ( 60 in-lb <sub>f</sub> )

NOTE: There are 0.076 m (3.0 in.) between the two 444.8 N (100 lb<sub>f</sub>) normal force gages and 0.0635 m (2.5 in.) between the two 222.4 N (50 lb<sub>f</sub>) side force gages.

Table 4  
REFERENCE DIMENSIONS

Parameters	Full Scale	Model Scale
Reference Area, $S_{ref}$ ( $m^2$ )	15.70	0.0051
( $ft^2$ )	168.948	0.0547
Reference Length, $l_{ref}$ (m)	17.88	0.322
(ft)	58.667	1.056
Geometrical Center of Balance (distance from model nose)		
5B Model (m)	—	0.204
(ft)	—	0.670
HB Model (m)	—	0.205
(ft)	—	0.672
Moment Reference Point c.g. (distance from model nose)		
.50 $l$ (m)	8.94	0.161
(ft)	29.33	0.528



Table 5

## COEFFICIENT ACCURACY

a. Task MK XLI-A Balance  
(Used for AMOOS 5B Tests)

	$p_o = 1200$ psia
$C_N$	$\pm 0.0782$
$C_Y$	$\pm 0.039$
$C_A$	$\pm 0.0117$
$C_m$	$\pm 0.0092$
$C_n$	$\pm 0.0038$
$C_l$	$\pm 0.0031$

b. Task MK XVIII-A Balance  
(Used for AMOOS HB Tests)

	$p_o = 1200$ psia	$p_o = 600$ psia
$C_N$	$\pm 0.0782$	$\pm 0.1564$
$C_Y$	$\pm 0.039$	$\pm 0.078$
$C_A$	$\pm 0.0234$	$\pm 0.0468$
$C_m$	$\pm 0.0092$	$\pm 0.0184$
$C_n$	$\pm 0.0038$	$\pm 0.0076$
$C_l$	$\pm 0.0018$	$\pm 0.0036$

Table 6  
 TEST SCHEDULE  
 AMOOS Test No. 1  
 Ames Test No. 179

Run	Model	Flap	$\delta$ (deg)	$\alpha$ (Nom) (deg)	$\beta$ (Nom) (deg)	$P_o$ (psi)
1	5B	Comp	0	A	0	1200
2	5B	Comp	+10	A	0	1200
3	5B	Comp	+20	A	0	1200
4	5B	Exp	0	A	0	1200
5	5B	Exp	-10	A	0	1200
6	5B	Exp	-20	A	0	1200
7	5B	Exp	0	50	B	1200
8	5B	Comp	0	50	B	1200
9	5B	Comp	0	45	B	1200
10	5B	Exp	0	45	B	1200
11	5B	Exp	0	40	B	1200
12	5B	Comp	0	40	B	1200
13	HB	Comp	0	A	0	1200
14	HB	Comp	10	A	0	1200
15	HB	Comp	20	A	0	1200
16	HB	Comp	40	A	0	1200
17	HB	Exp	0	A	0	1200
18	HB	Exp	-10	A	0	1200
19	HB	Exp	-20	A	0	1200
20	HB	Exp	-40	A	0	1200
21	HB	Exp	-40	50	B	1200
22	HB	Exp	0	50	B	600
23	HB	Comp	0	50	B	600
24	HB	Comp	40	50	B	600
25	HB	Comp	40	A	0	600
26	HB	Comp	40	45	B	600
27	HB	Comp	0	45	B	600
28	HB	Exp	0	45	B	600
29	HB	Exp	0	40	B	600
30	HB	Comp	0	40	B	600
31	HB	Comp	40	40	B	600
32	HB	Exp	-40	40	B	600

Note: A = 30 to 65 degrees, B = -2 to +10 degrees.

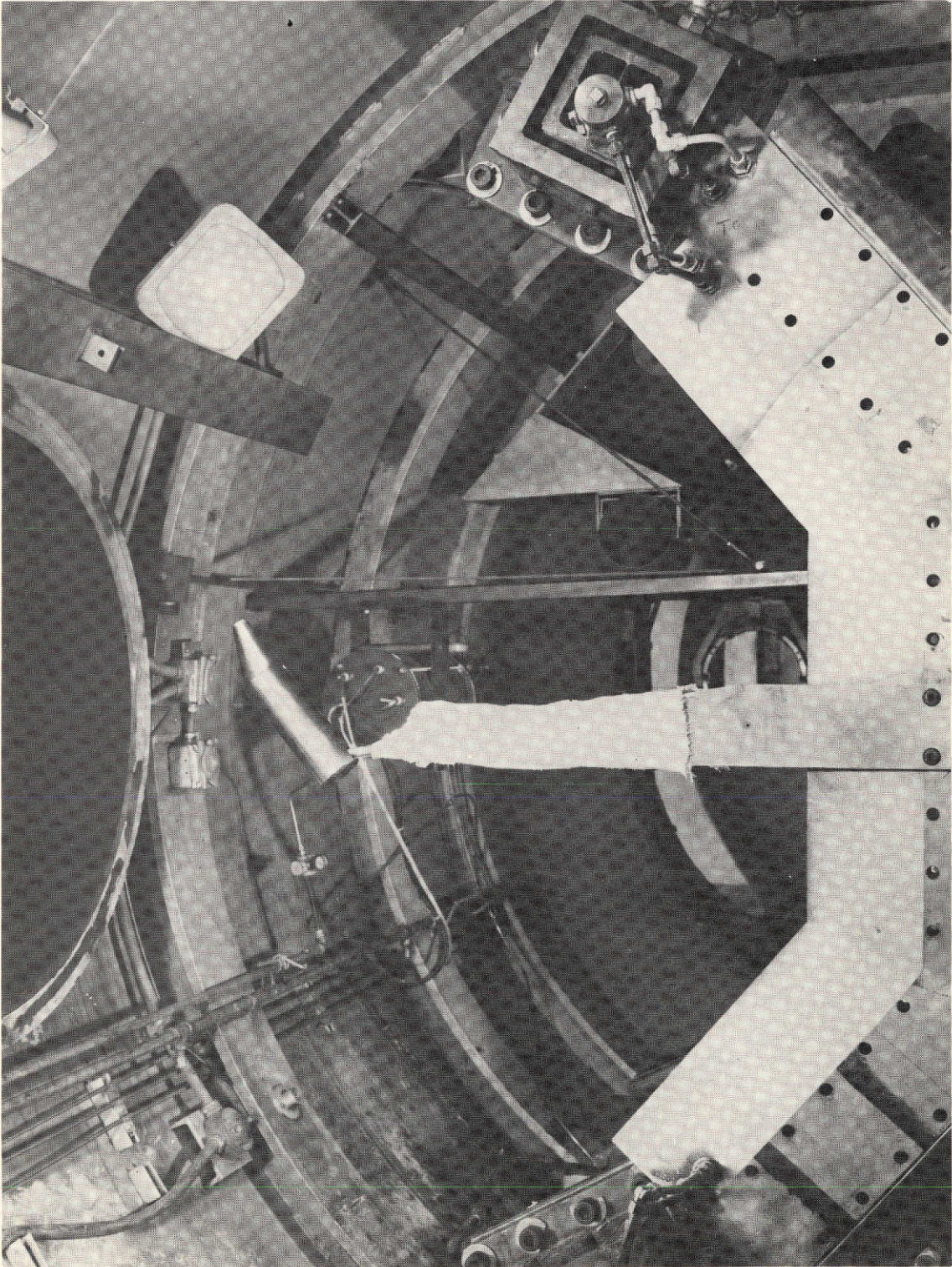


Fig. 1 - The Ames 3.5-Foot Hypersonic Wind Tunnel and Model Support System



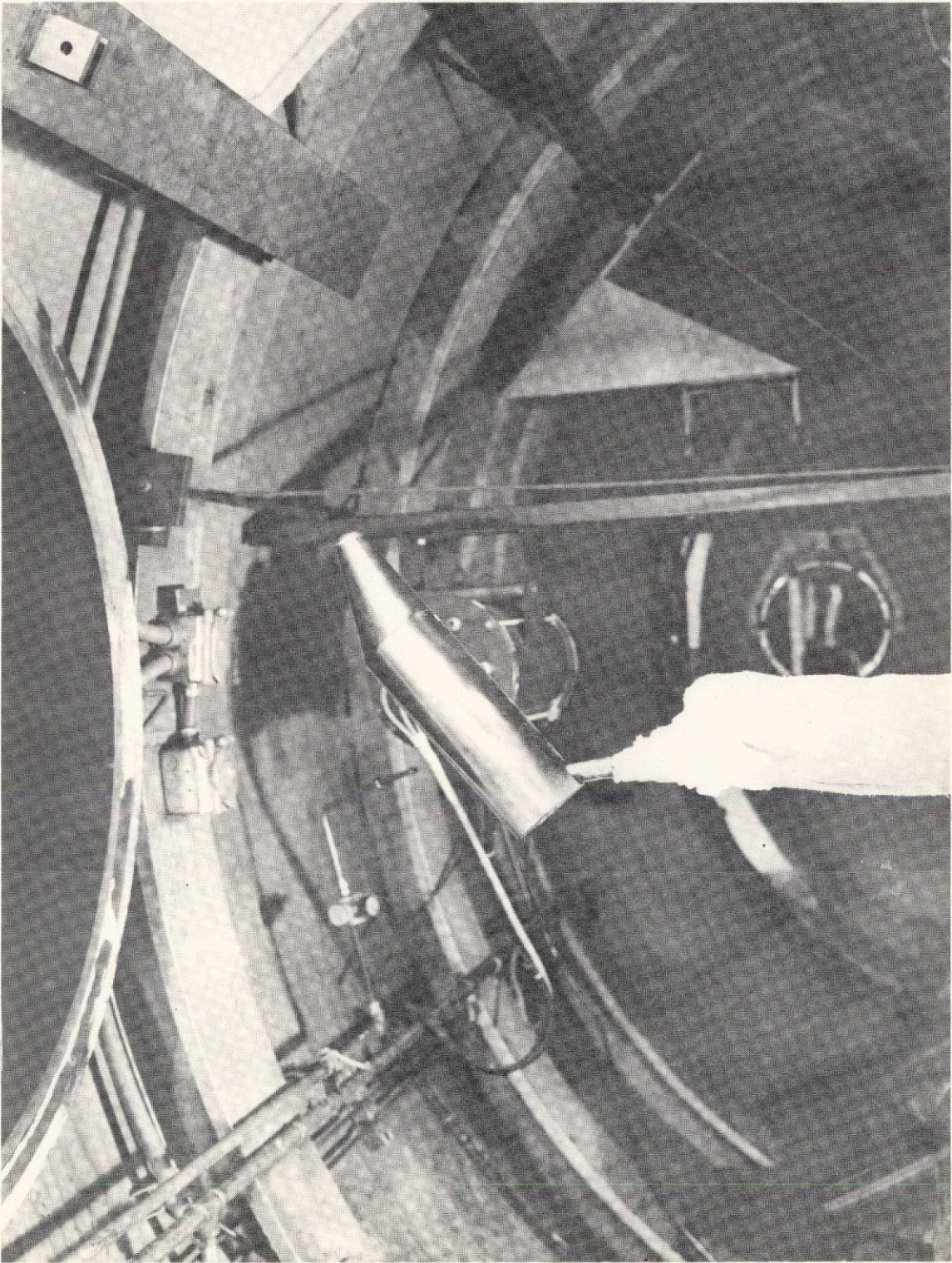


Fig. 2 - The AMOOS 5B Configuration



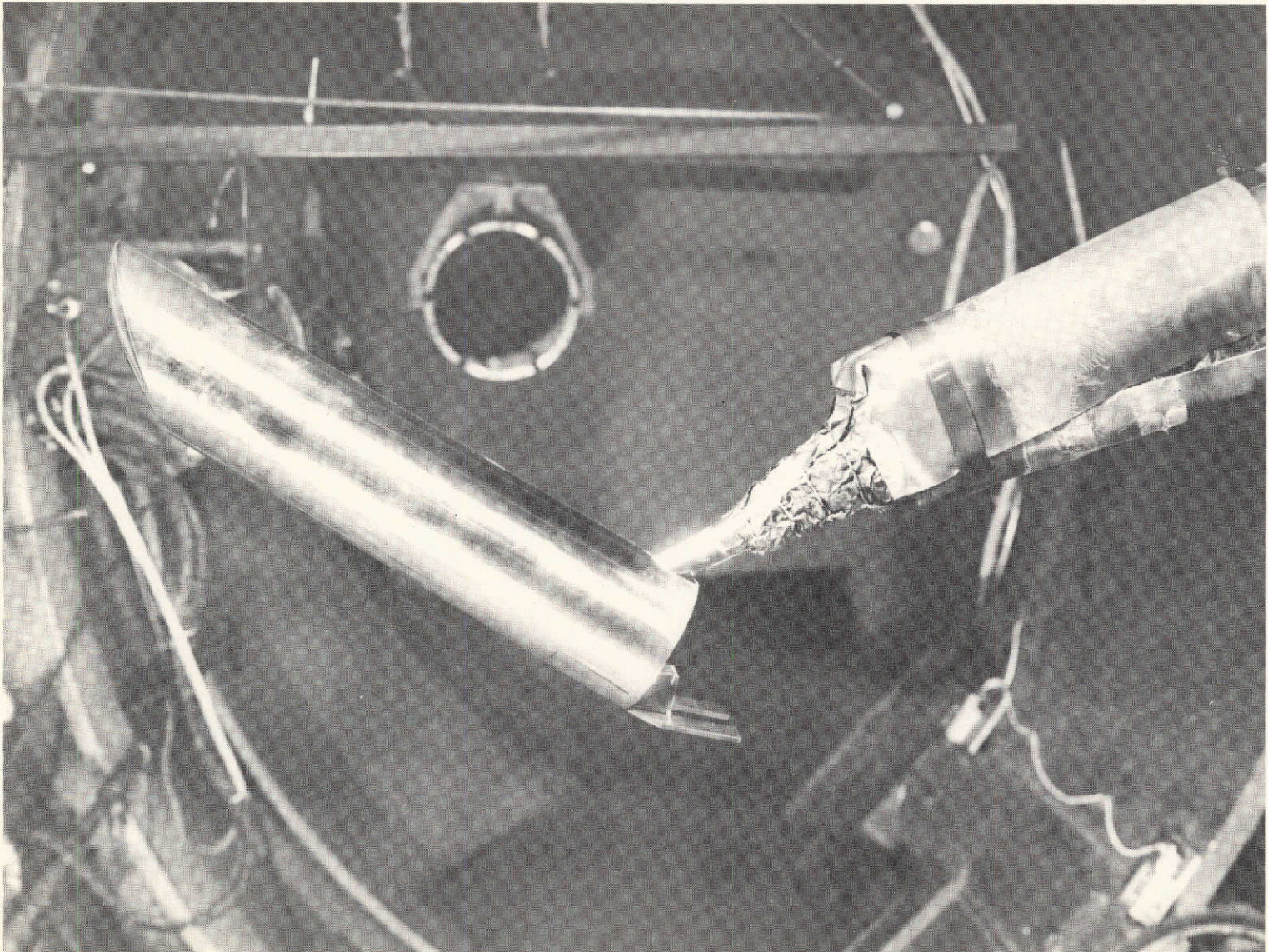
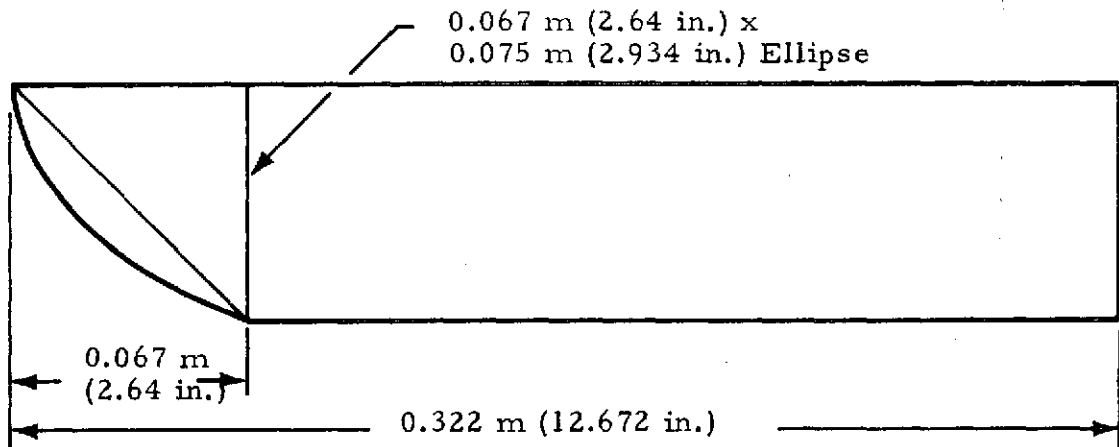
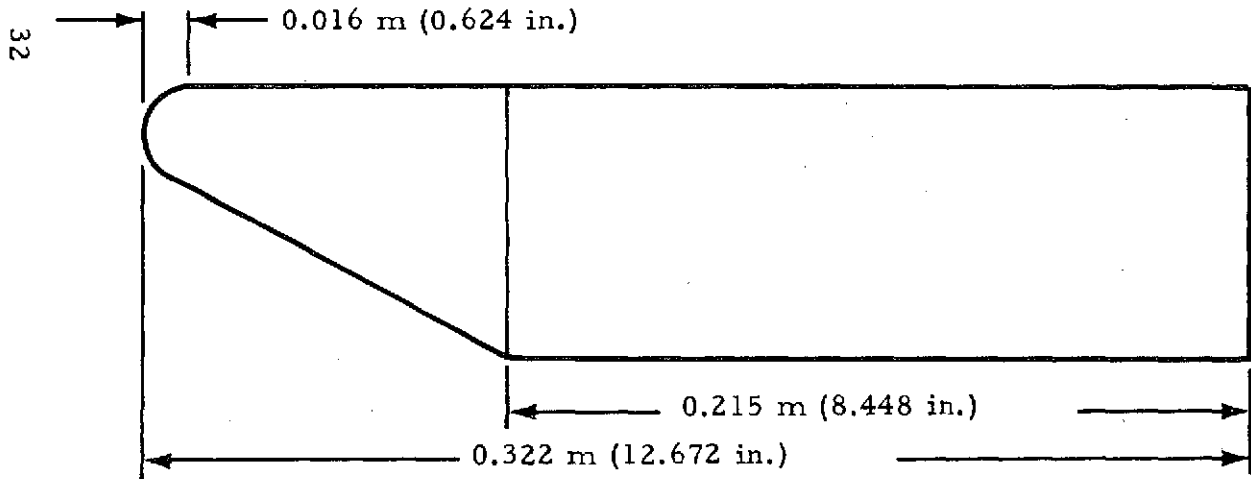
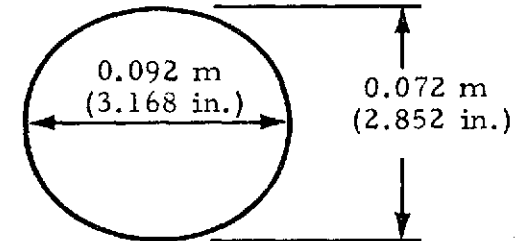


Fig. 3 - The AMOOS HB Configuration with the Expansion Flap Deflected



AMOOS HB CONFIGURATION



AMOOS 5B CONFIGURATION

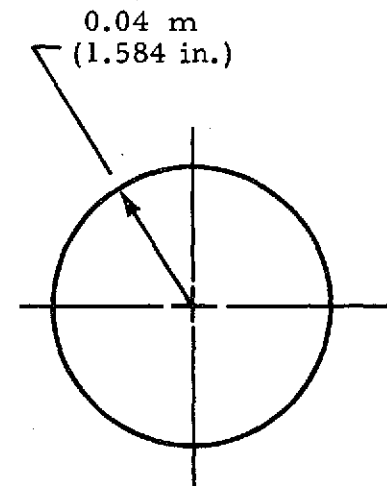
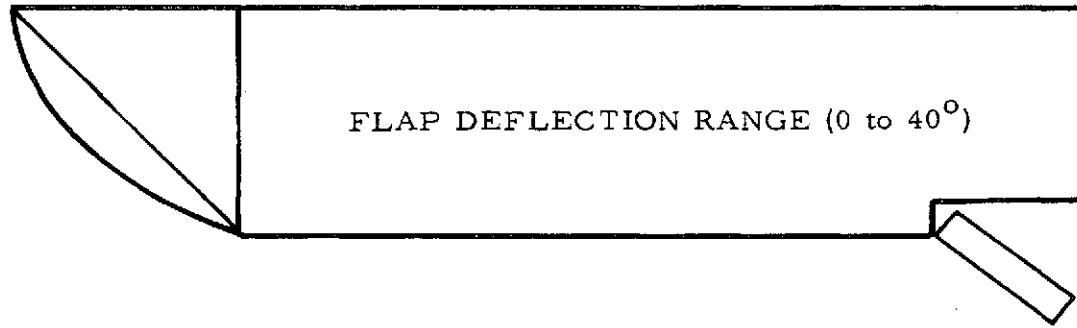
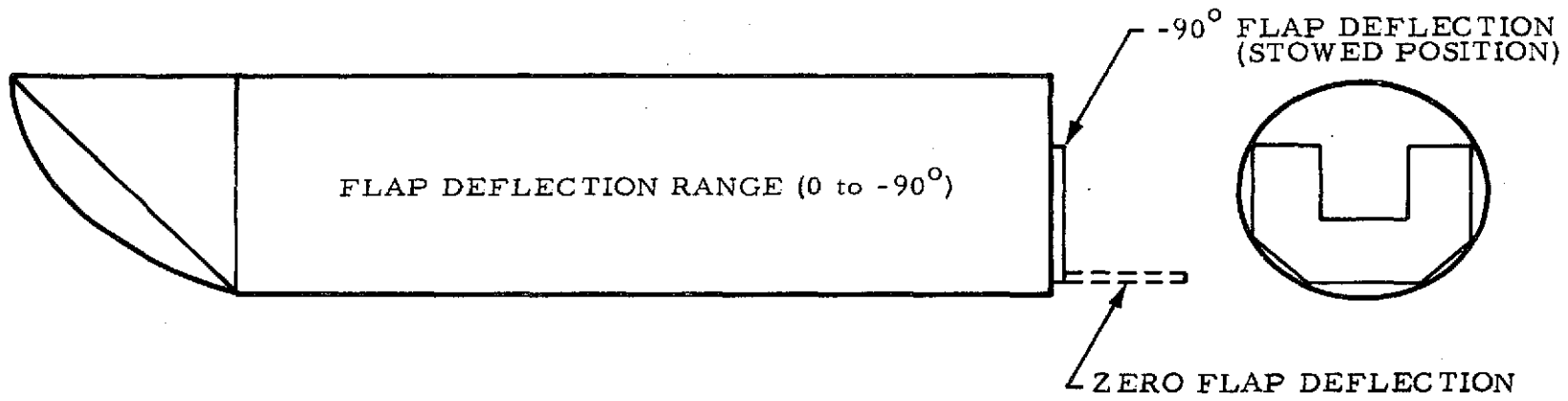
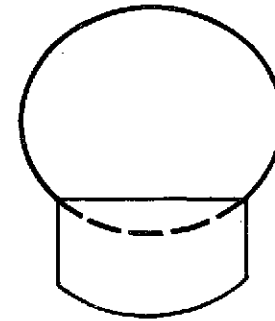


Fig. 4a - Drawings of the AMOOS HB and 5B Configurations



AMOOS HB CONFIGURATION WITH COMPRESSION FLAP



AMOOS HB CONFIGURATION WITH EXPANSION FLAP

Fig. 4b - AMOOS Flap Geometries



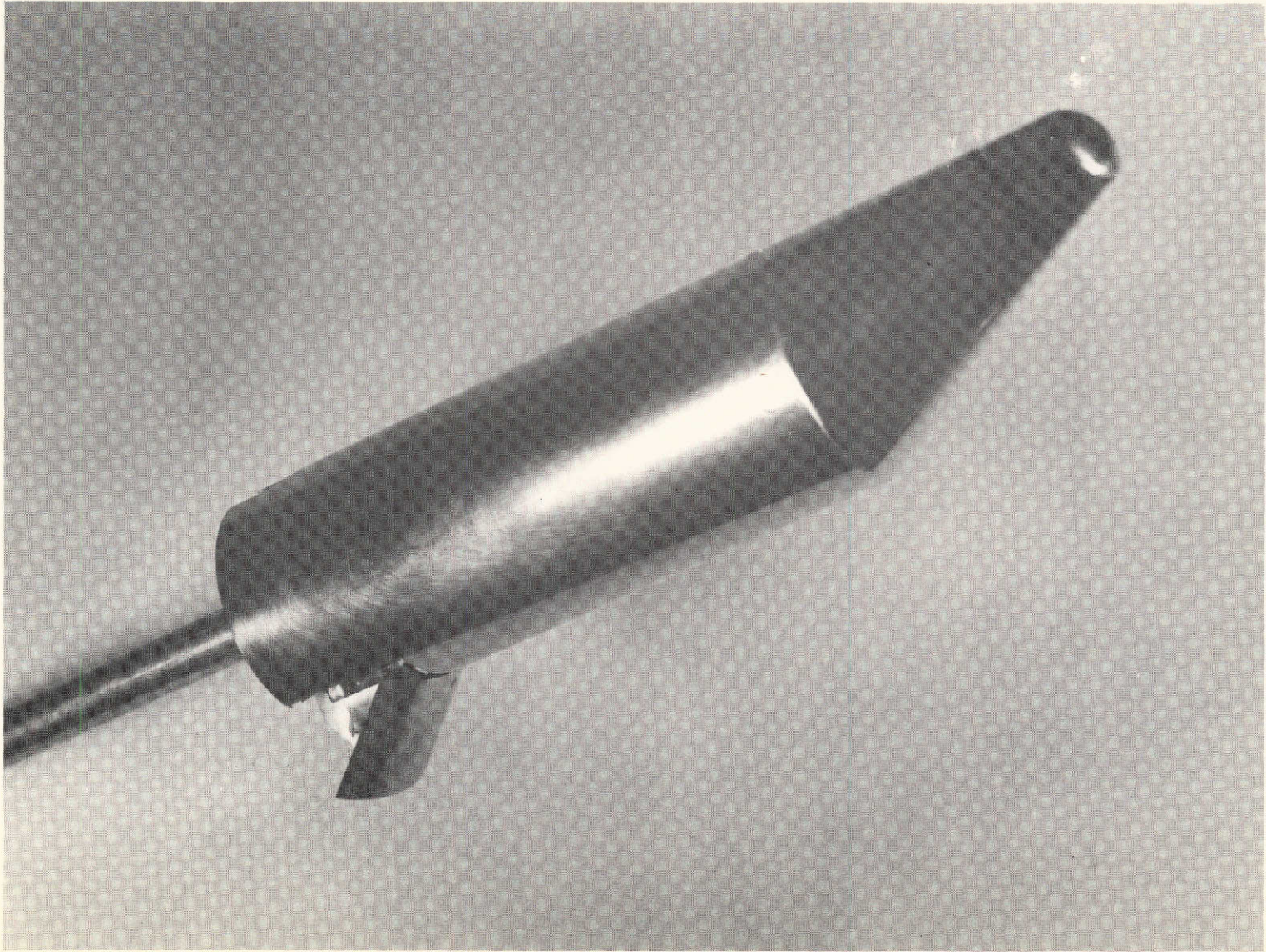


Fig. 5 - The AMOOS 5B Configuration with the Compression Flap Deflected



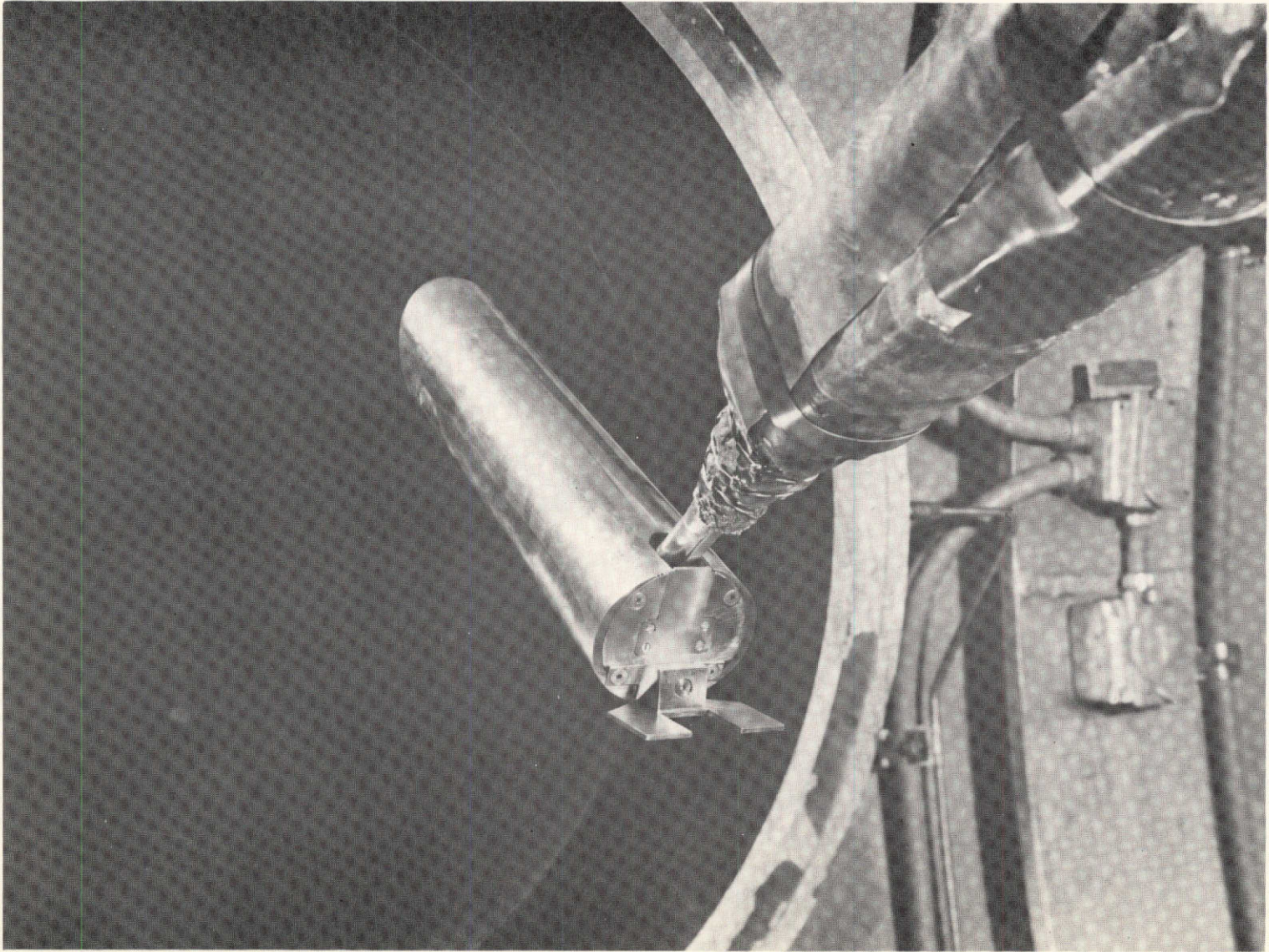


Fig. 6 - Rear View of the AMOOS HB Configuration

Note:

1. Positive directions of force coefficients, moment coefficients, and angles are indicated by arrows.
2. For clarity, origins of wind and stability axes have been displaced from the center of gravity.

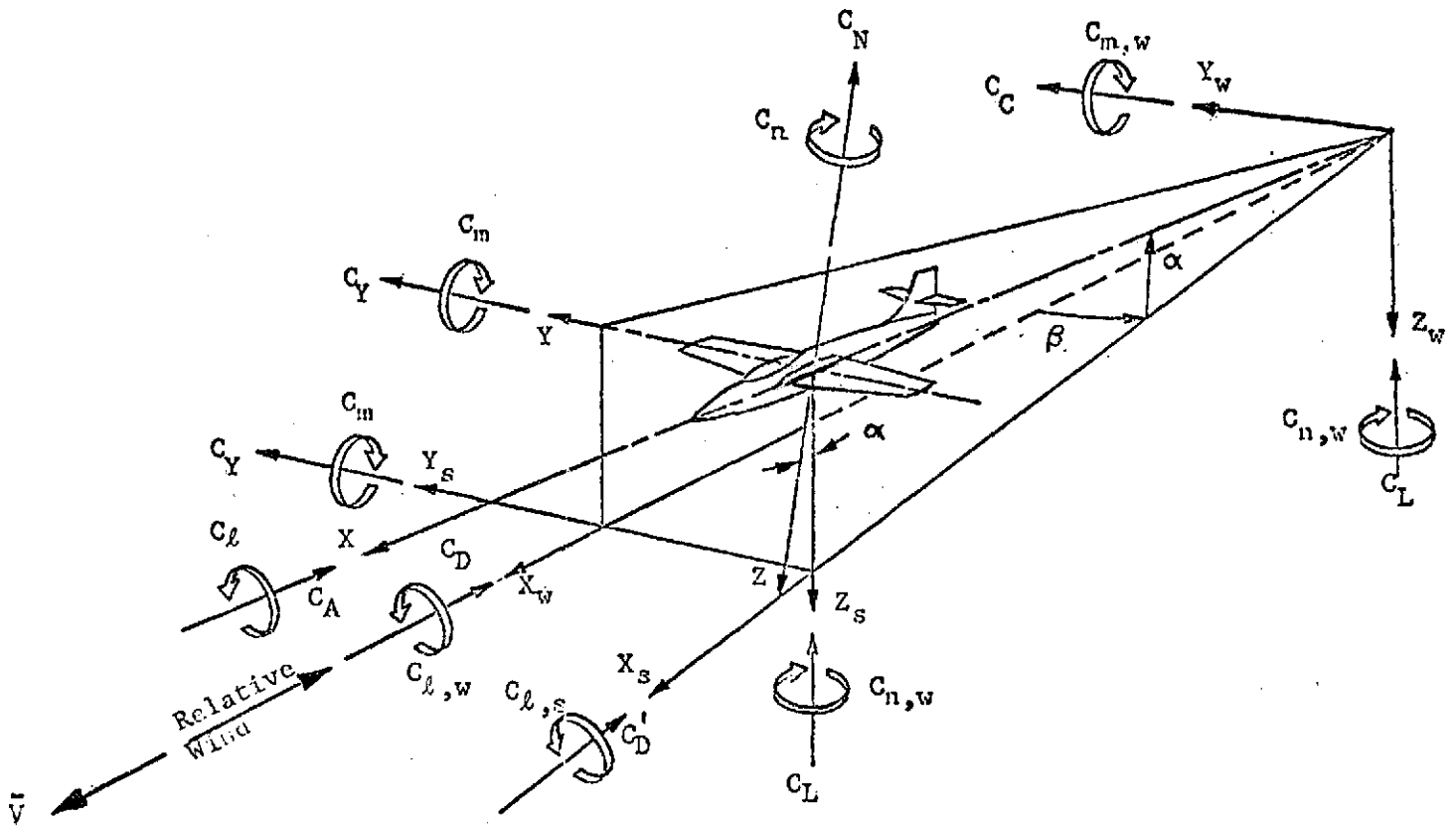


Fig. 7 - Axis Systems Showing Direction and Sense of Force and Moment Coefficients, Angle of Attack, and Sideslip Angle

COMPARISON OF AMOOS 5B EXPERIMENTAL AND THEORETICAL AERODYNAMIC DATA

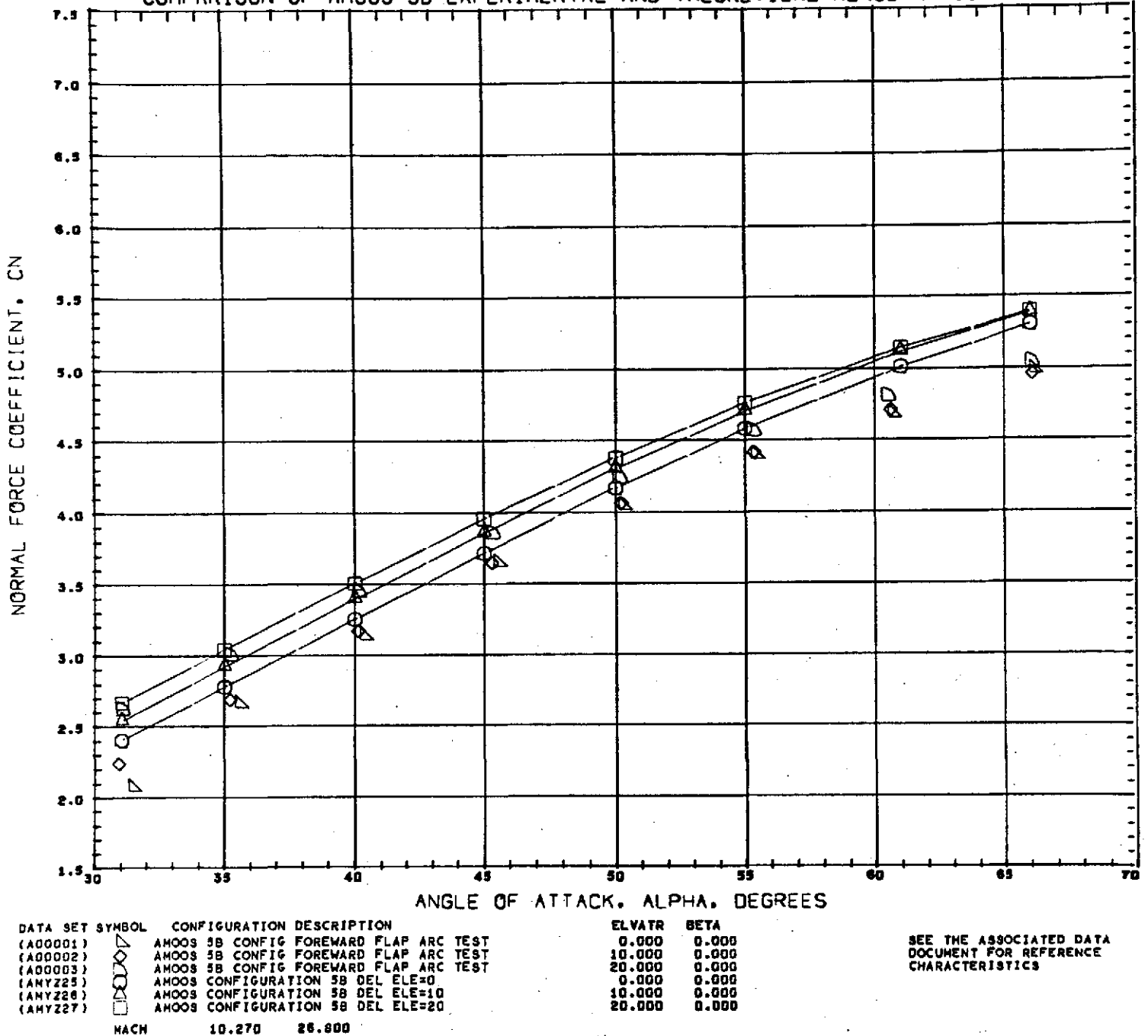


Fig. 8a - Comparison of Theoretical and Experimental Normal Force Coefficients for the 5B Configuration with Compression Flap Deflections



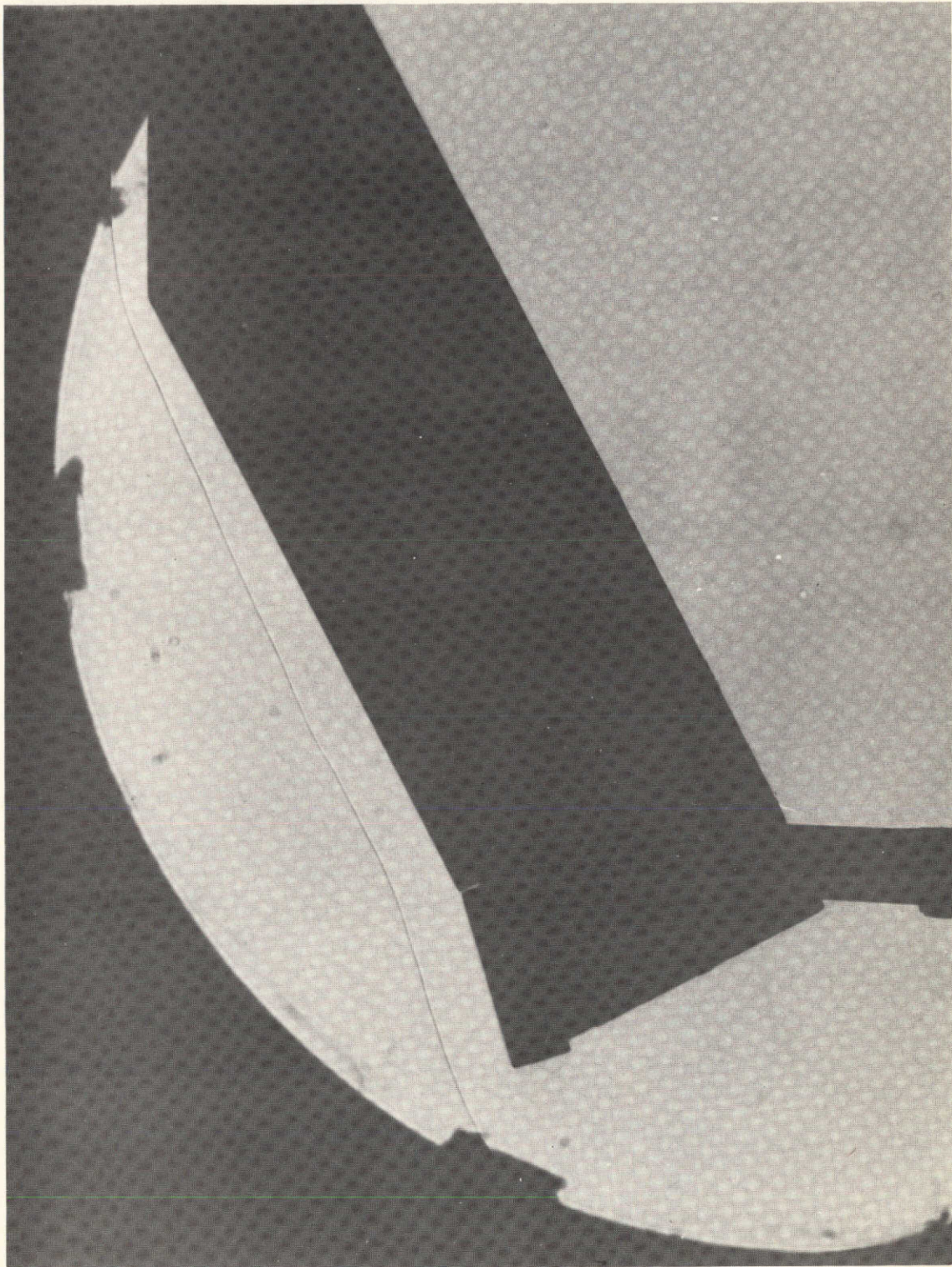


Fig. 8b - Shadowgraph of the AMOOS 5B Configuration with a Compression Flap Deflection of  $10^{\circ}$  at an Angle of Attack of  $65^{\circ}$

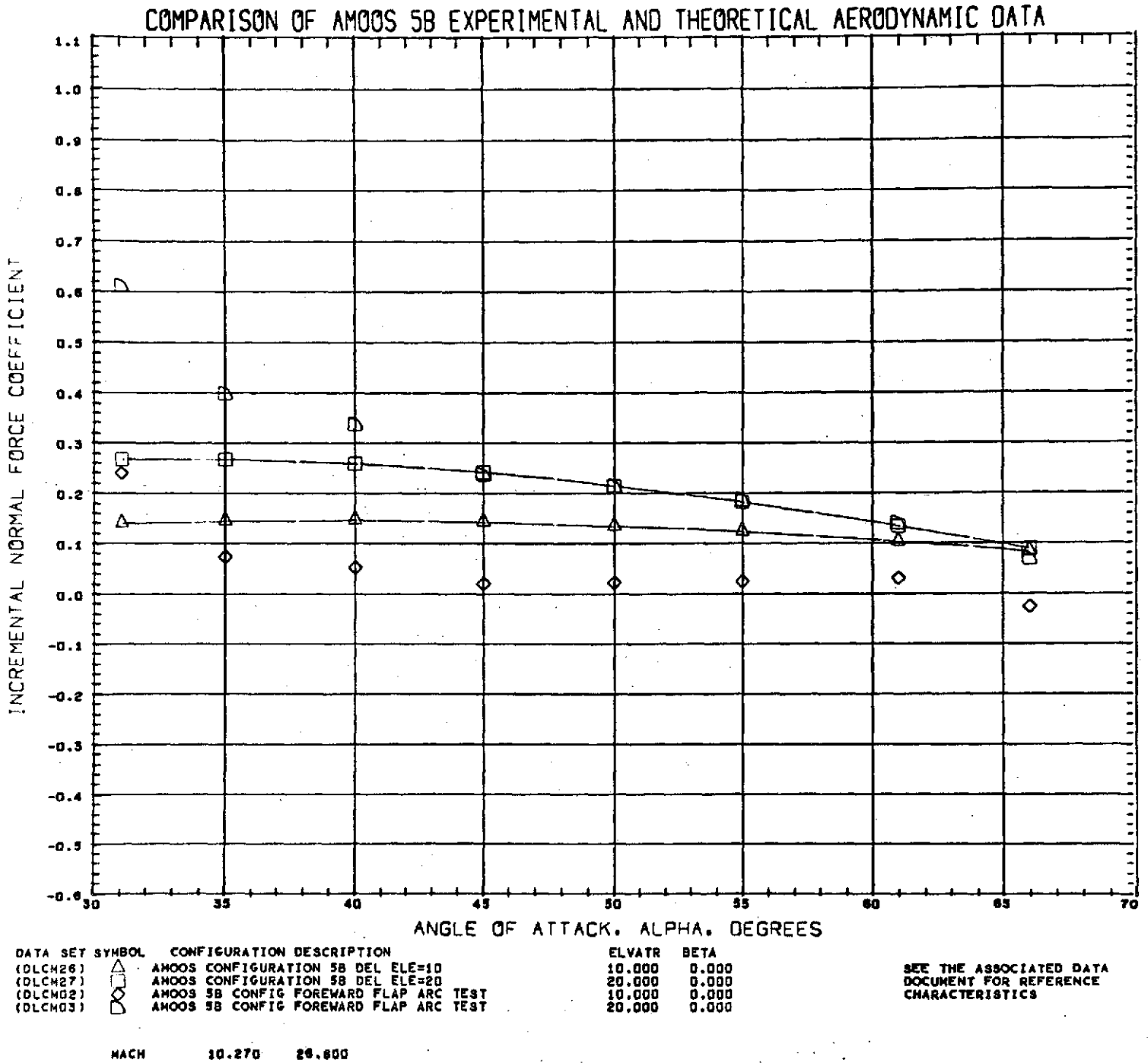


Fig. 8c - Comparison of Theoretical and Experimental Incremental Normal Force Coefficients for the 5B Configuration with Compression Flap Deflections

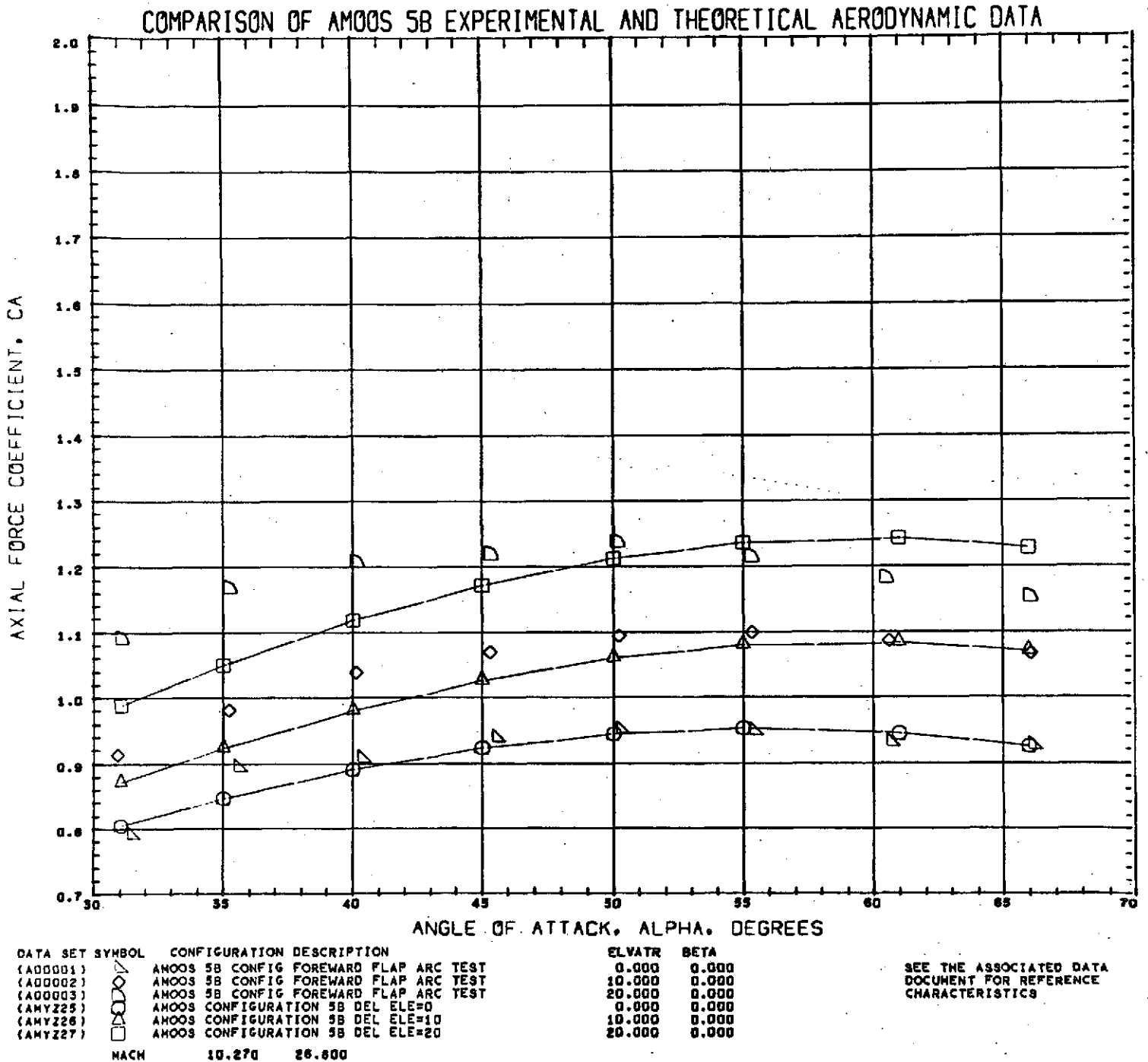
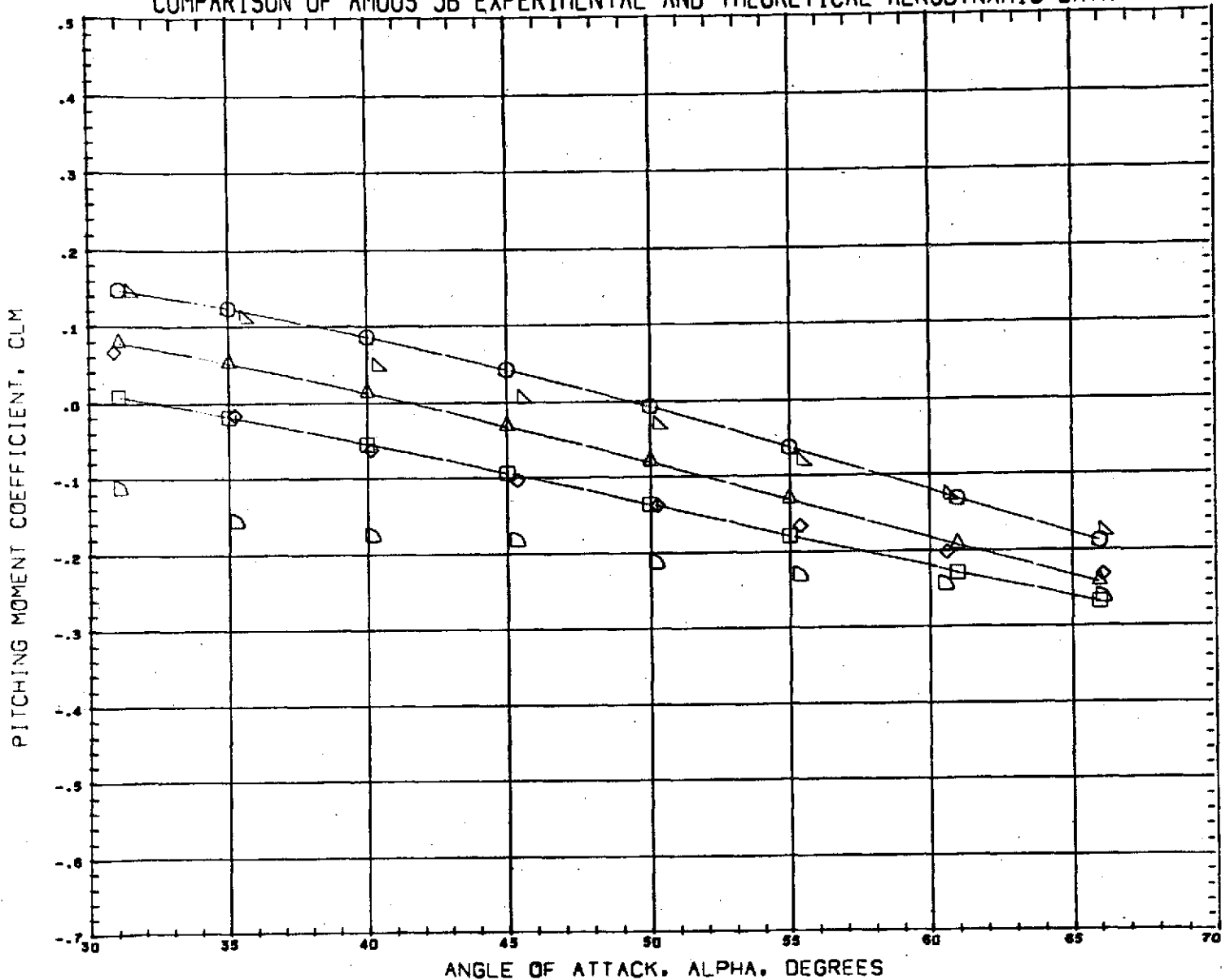


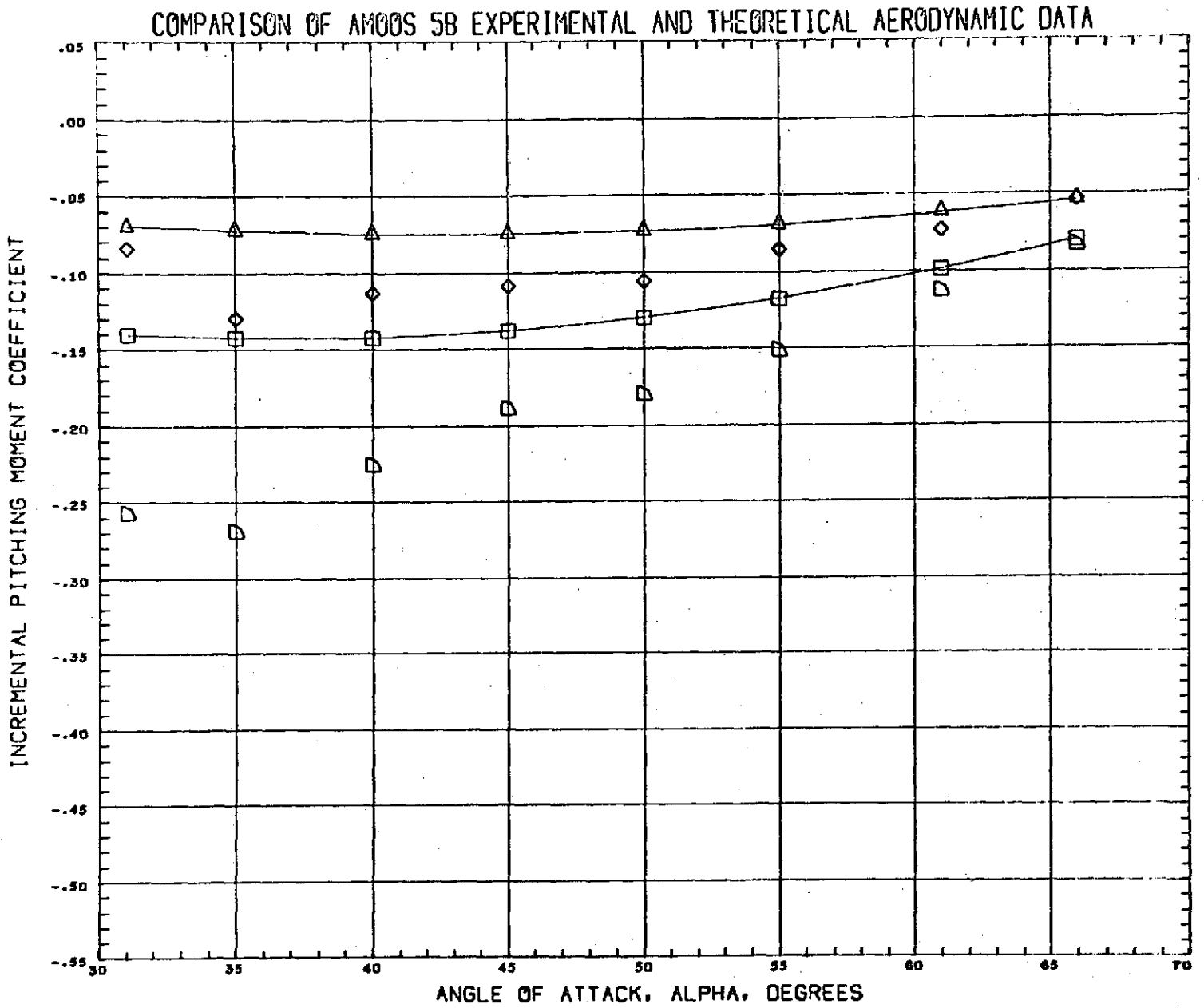
Fig. 8d - Comparison of Theoretical and Experimental Axial Force Coefficients for the 5B Configuration with Compression Flap Deflections

COMPARISON OF AMOOS 5B EXPERIMENTAL AND THEORETICAL AERODYNAMIC DATA



DATA SET SYMBOL	CONFIGURATION DESCRIPTION	ELVATR	BETA	
(AG0001)	AMOOS 5B CONFIG FORWARD FLAP ARC TEST	0.000	0.000	SEE THE ASSOCIATED DATA DOCUMENT FOR REFERENCE CHARACTERISTICS
(AG0002)	AMOOS 5B CONFIG FORWARD FLAP ARC TEST	10.000	0.000	
(AG0003)	AMOOS 5B CONFIG FORWARD FLAP ARC TEST	20.000	0.000	
(AMZ225)	AMOOS CONFIGURATION 5B DEL ELE=0	0.000	0.000	
(AMZ226)	AMOOS CONFIGURATION 5B DEL ELE=10	10.000	0.000	
(AMZ227)	AMOOS CONFIGURATION 5B DEL ELE=20	20.000	0.000	
MACH 10.270 26.800				

Fig. 8e - Comparison of Theoretical and Experimental Pitching Moment Coefficients for the 5B Configuration with Compression Flap Deflections



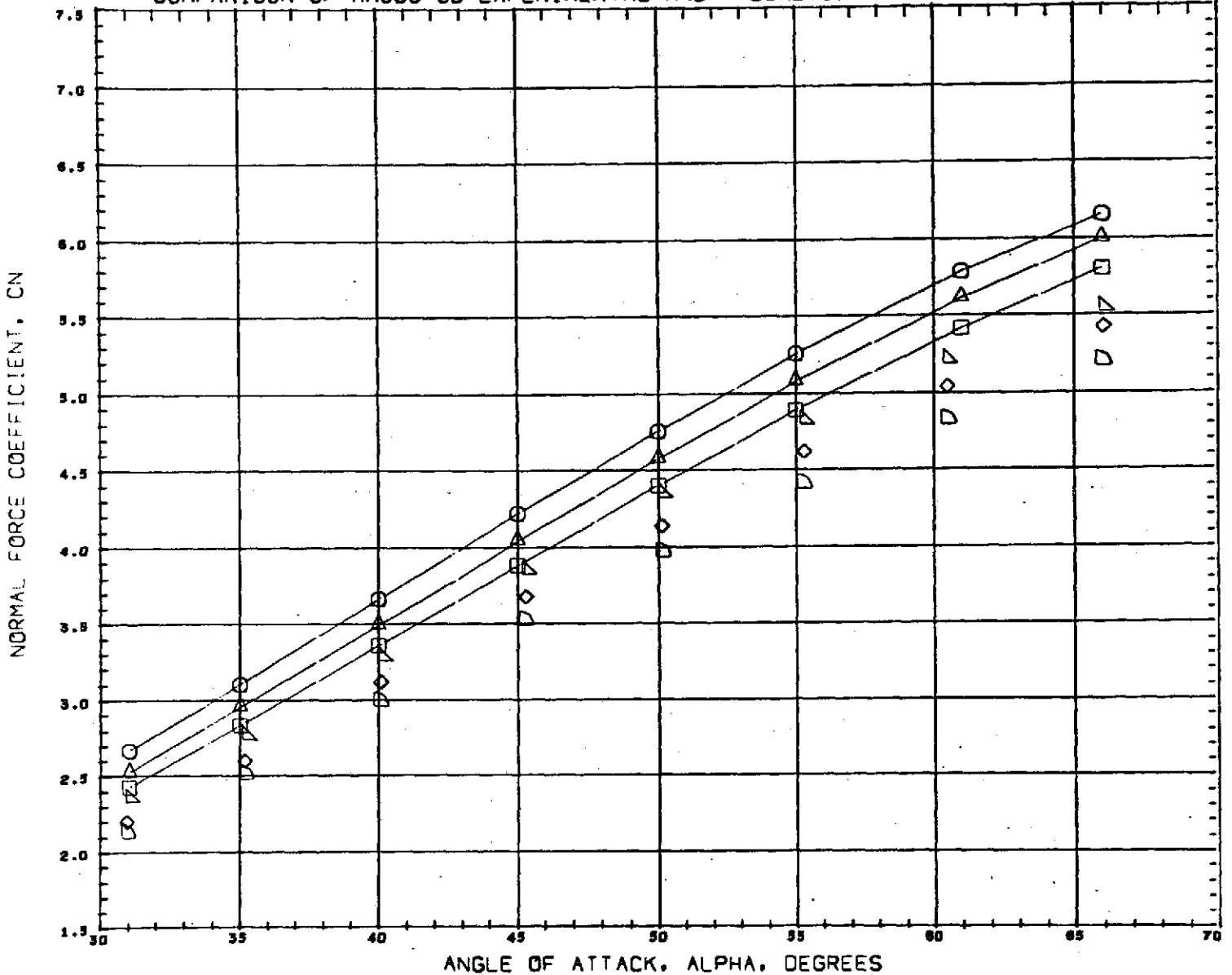
DATA SET SYMBOL	CONFIGURATION DESCRIPTION	ELVATR	BETA	
(DLCH26)	AMOOS CONFIGURATION 5B DEL ELE=10	10.000	0.000	SEE THE ASSOCIATED DATA DOCUMENT FOR REFERENCE CHARACTERISTICS
(DLCH27)	AMOOS CONFIGURATION 5B DEL ELE=20	20.000	0.000	
(DLCH02)	AMOOS 5B CONFIG FORWARD FLAP ARC TEST	10.000	0.000	
(DLCH03)	AMOOS 5B CONFIG FORWARD FLAP ARC TEST	20.000	0.000	

MACH      10.270      26.000

Fig. 8f - Comparison of Theoretical and Experimental Incremental Pitching Moment Coefficients for the 5B Configuration with Compression Flap Deflections



COMPARISON OF AMOOS 5B EXPERIMENTAL AND THEORETICAL AERODYNAMIC DATA



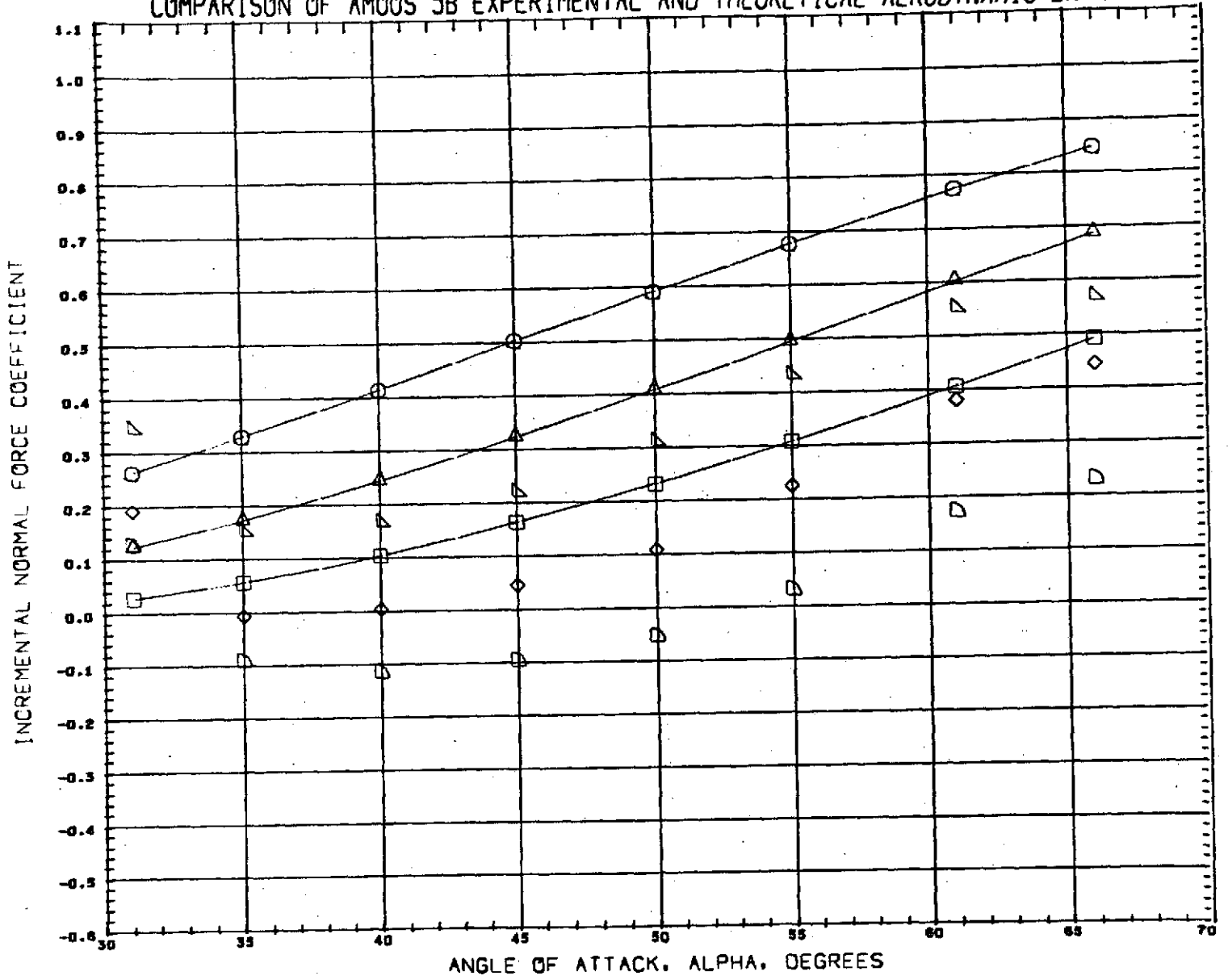
DATA SET SYMBOL	CONFIGURATION DESCRIPTION	ELVATR	BETA
(A00004)	AMOOS 5B CONFIG AFT FLAP ARC TEST	0.000	0.000
(A00005)	AMOOS 5B CONFIG AFT FLAP ARC TEST	-10.000	0.000
(A00006)	AMOOS 5B CONFIG AFT FLAP ARC TEST	-20.000	0.000
(ANY265)	AMOOS CONFIGURATION 5B BAS ROT DEL ELE=0	0.000	0.000
(ANY266)	AMOOS CONFIGURATION 5B BAS ROT DEL ELE=-10	-10.000	0.000
(ANY267)	AMOOS CONFIGURATION 5B BAS ROT DEL ELE=-20	-20.000	0.000

SEE THE ASSOCIATED DATA DOCUMENT FOR REFERENCE CHARACTERISTICS

MACH 10.270 26.800

Fig. 8g - Comparison of Theoretical and Experimental Normal Force Coefficients for the 5B Configuration with Expansion Flap Deflections

COMPARISON OF AMOOS 5B EXPERIMENTAL AND THEORETICAL AERODYNAMIC DATA



DATA SET SYMBOL	CONFIGURATION DESCRIPTION	ELVATR	BETA
(DLCH65)	AMOOS CONFIGURATION 5B BAS ROT DEL ELE=0	0.000	0.000
(DLCH66)	AMOOS CONFIGURATION 5B BAS ROT DEL ELE=-10	-10.000	0.000
(DLCH67)	AMOOS CONFIGURATION 5B BAS ROT DEL ELE=-20	-20.000	0.000
(DLCH68)	AMOOS 5B CONFIG AFT FLAP ARC TEST	0.000	0.000
(DLCH69)	AMOOS 5B CONFIG AFT FLAP ARC TEST	-10.000	0.000
(DLCH70)	AMOOS 5B CONFIG AFT FLAP ARC TEST	-20.000	0.000

SEE THE ASSOCIATED DATA DOCUMENT FOR REFERENCE CHARACTERISTICS

MACH 10.270 26.800

Fig. 8h - Comparison of Theoretical and Experimental Incremental Normal Force Coefficients for the 5B Configuration with Expansion Flap Deflections

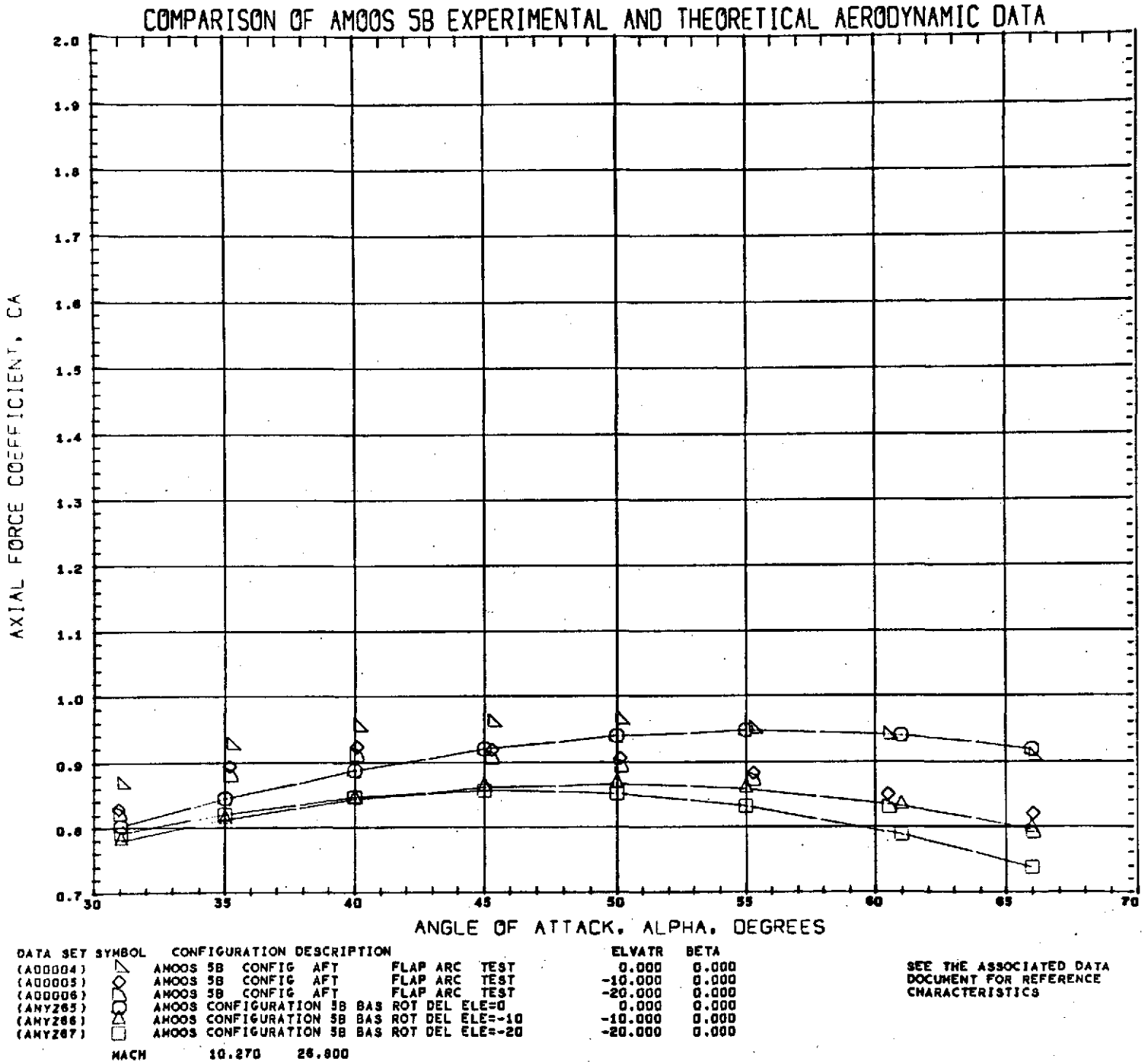


Fig. 8i - Comparison of Theoretical and Experimental Axial Force Coefficients for the 5B Configuration with Expansion Flap Deflections

COMPARISON OF AMOOS 5B EXPERIMENTAL AND THEORETICAL AERODYNAMIC DATA

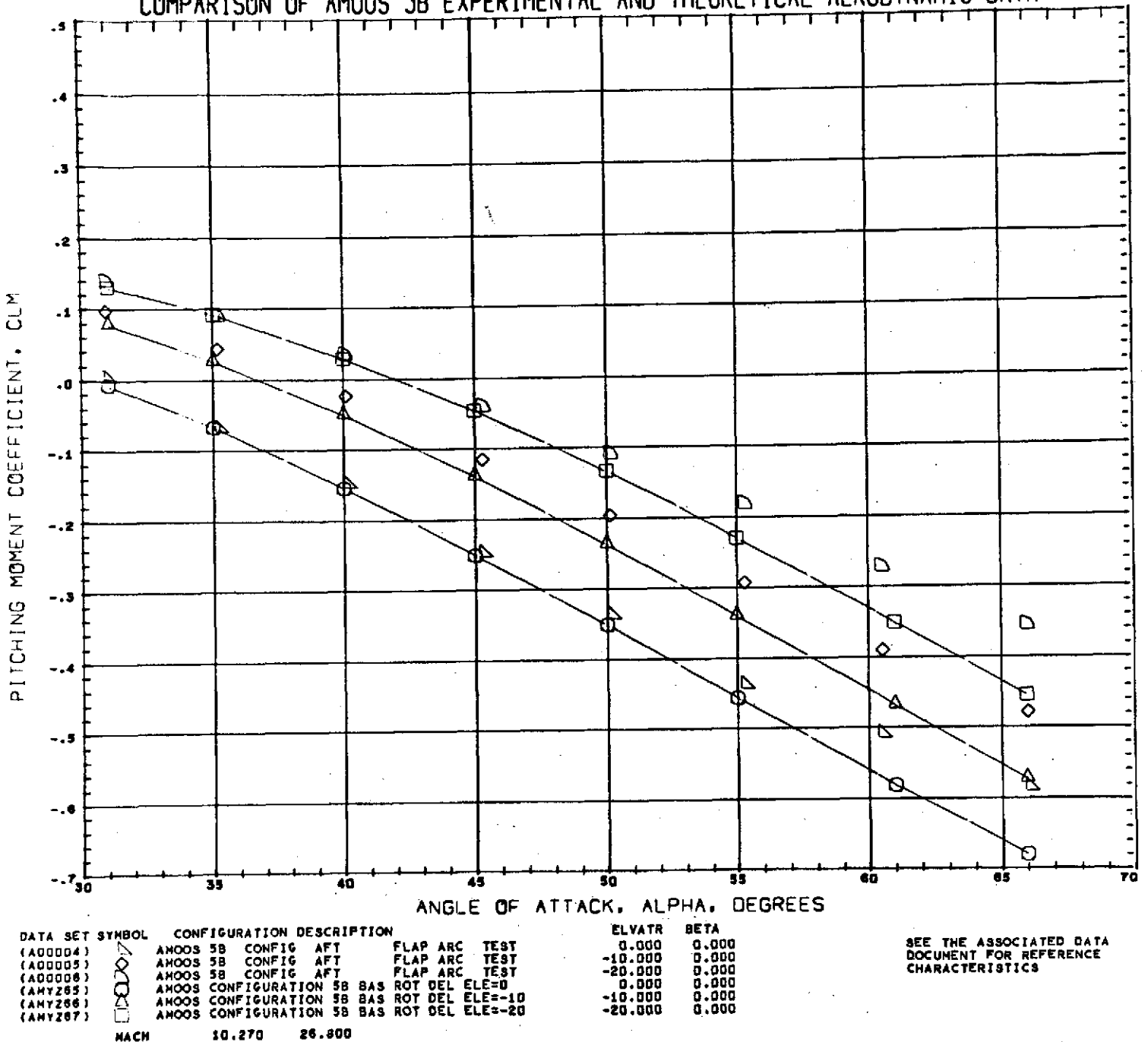


Fig. 8j - Comparison of Theoretical and Experimental Pitching Moment Coefficients for the 5B Configuration with Expansion Flap Deflections

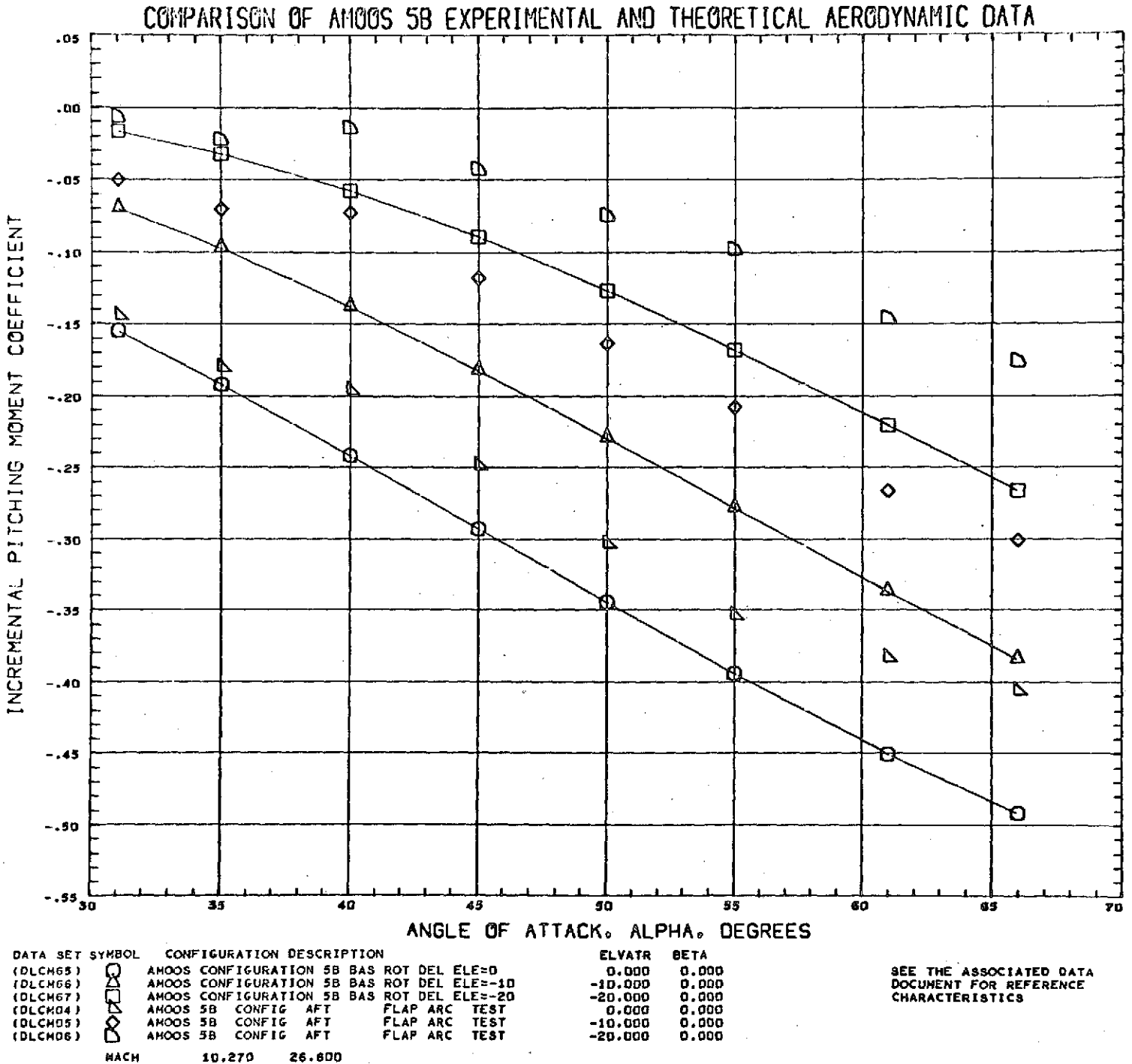


Fig. 8k - Comparison of Theoretical and Experimental Incremental Pitching Moment Coefficients for the 5B Configuration with Expansion Flap Deflections

COMPARISON OF AMOOS 5B EXPERIMENTAL AND THEORETICAL AERODYNAMIC DATA

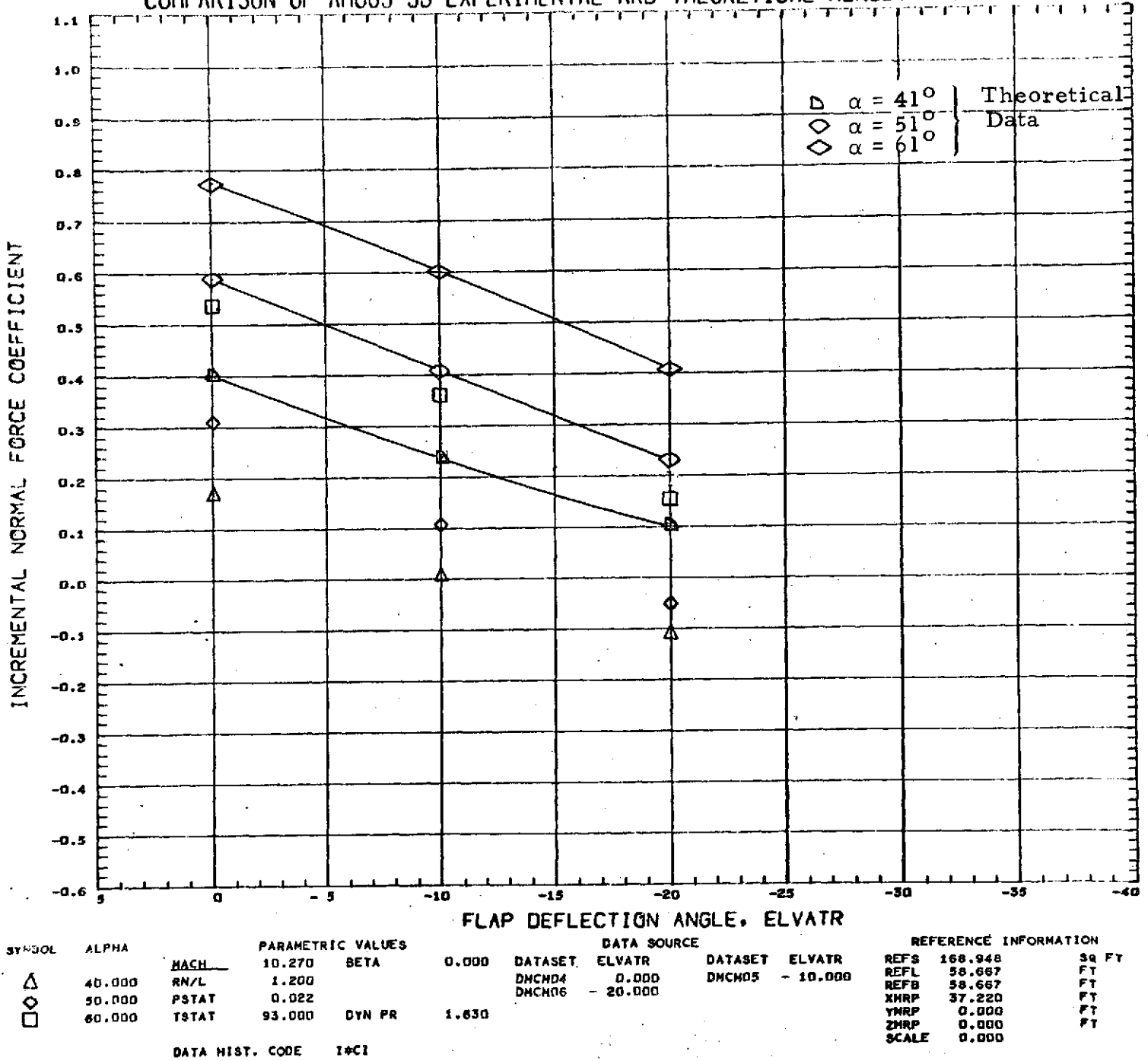


Fig. 8f - Plot of Incremental Normal Force Coefficients as Functions of Expansion Flap Deflection Angles for the 5B Configuration

COMPARISON OF AMOOS 5B EXPERIMENTAL AND THEORETICAL AERODYNAMIC DATA

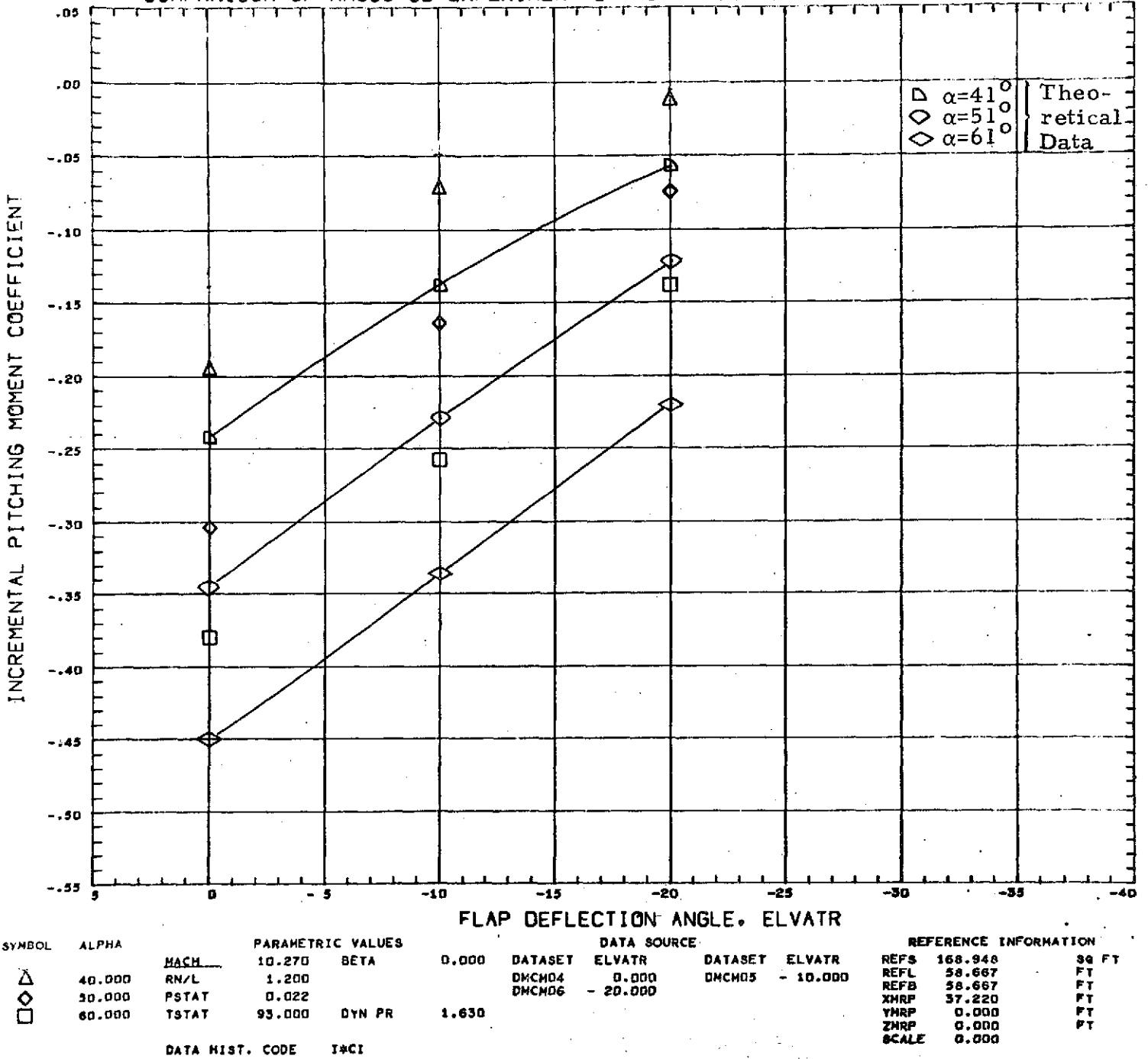


Fig. 8m - Plot of Incremental Pitching Moment Coefficients as Functions of Expansion Flap Deflection Angles for the 5B Configuration

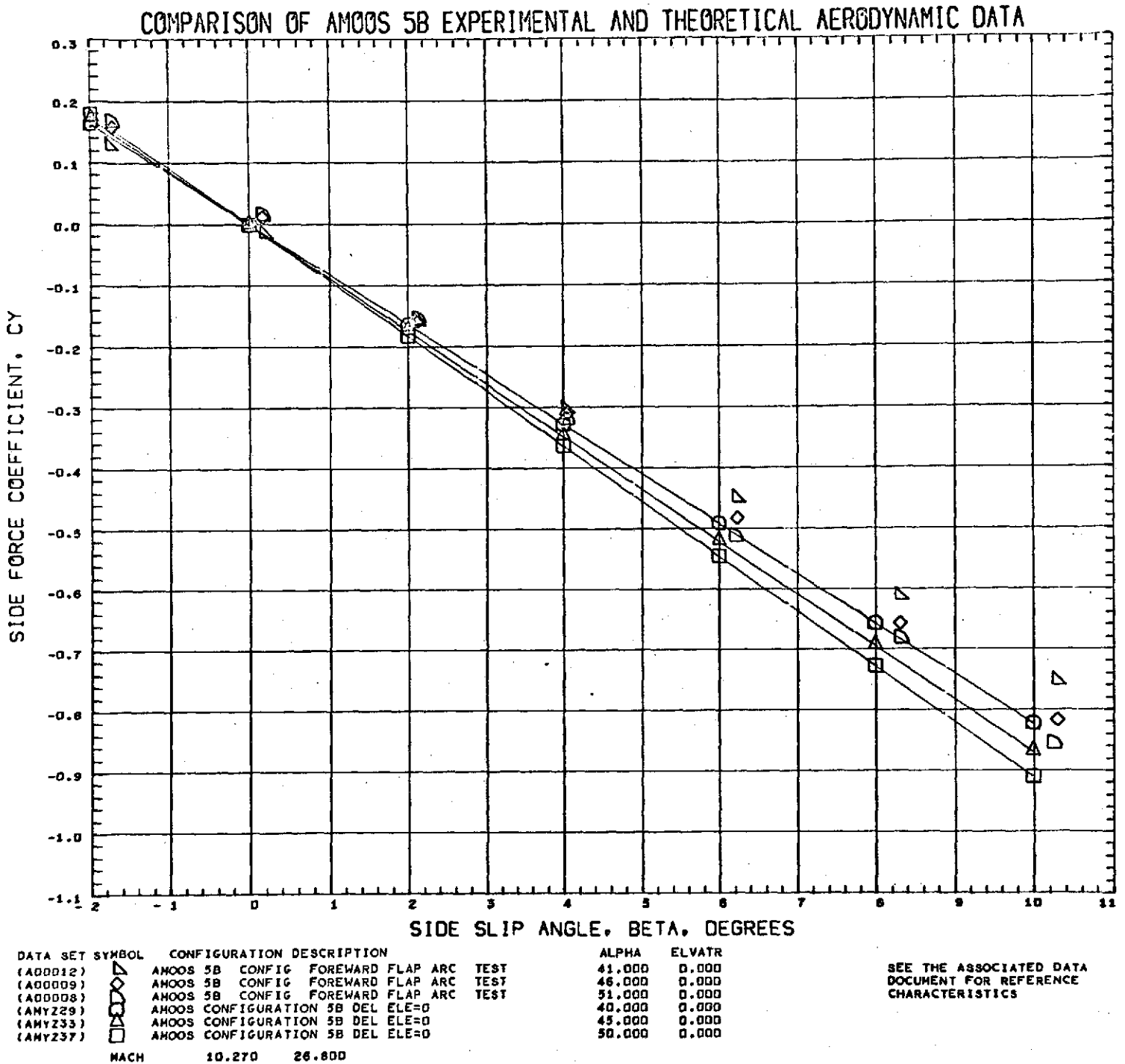


Fig. 9a - Comparison of Theoretical and Experimental Side Force Coefficients for the 5B Configuration with 0° Compression Flap Deflection



COMPARISON OF ANOOS 5B EXPERIMENTAL AND THEORETICAL AERODYNAMIC DATA

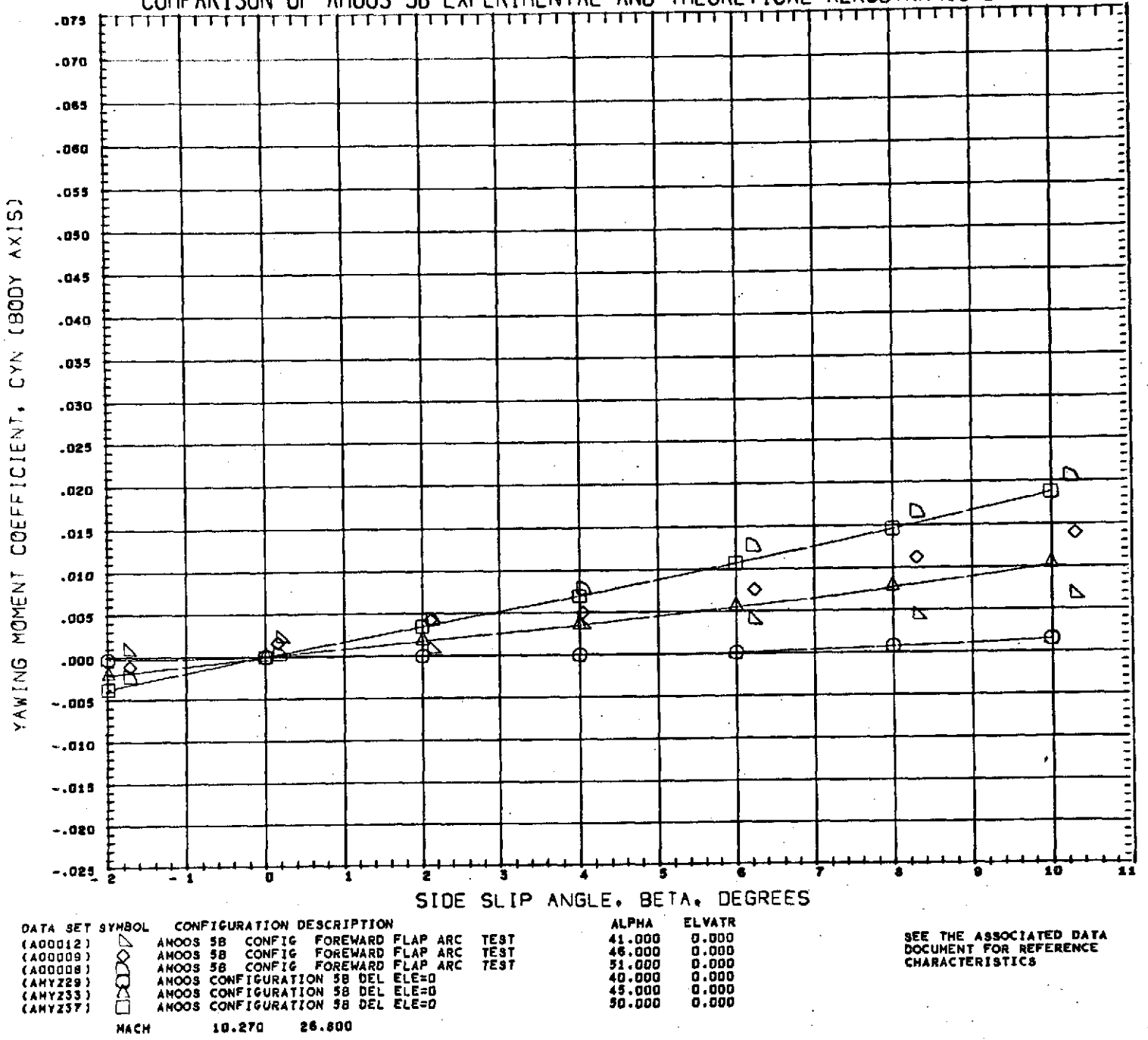
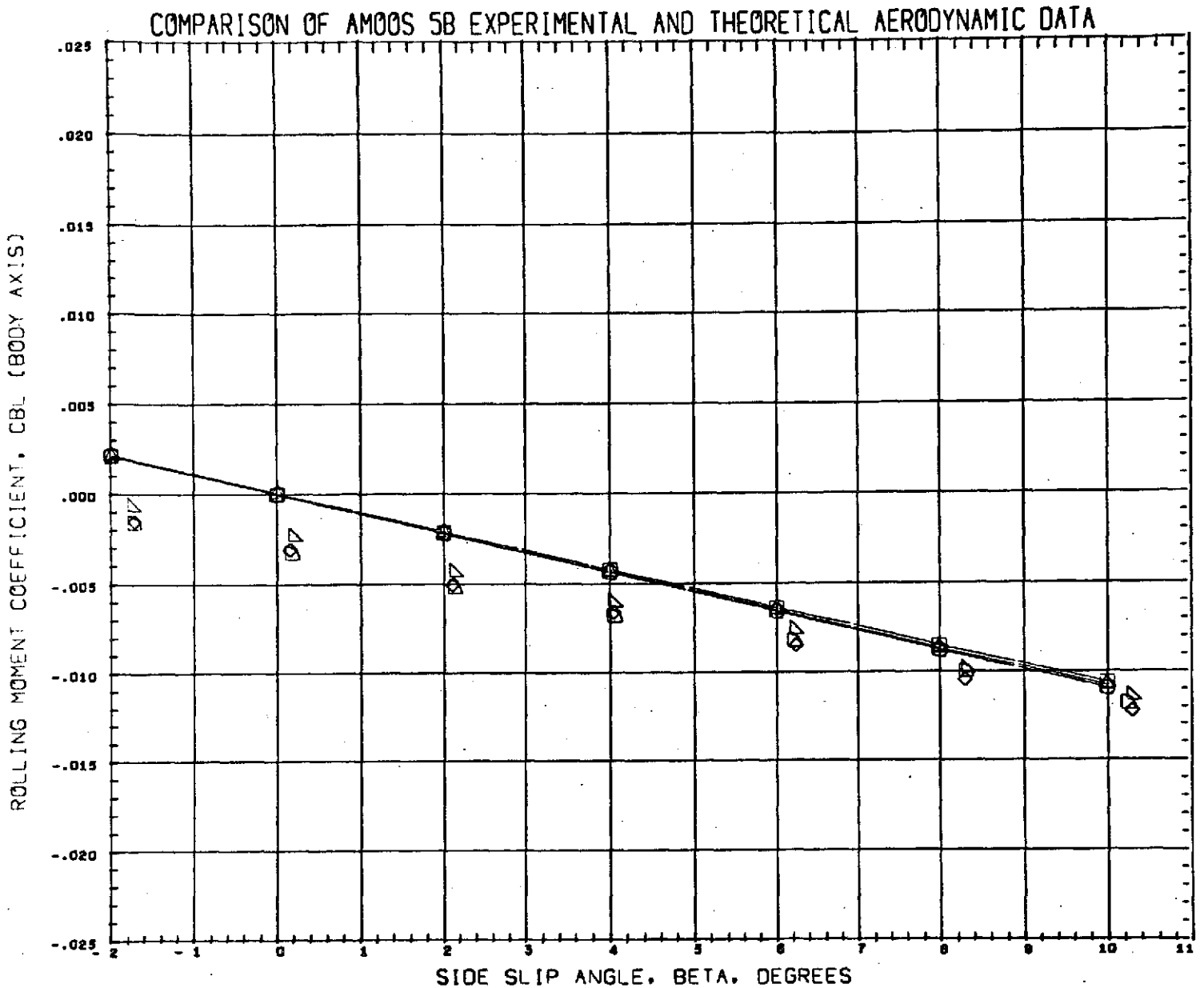


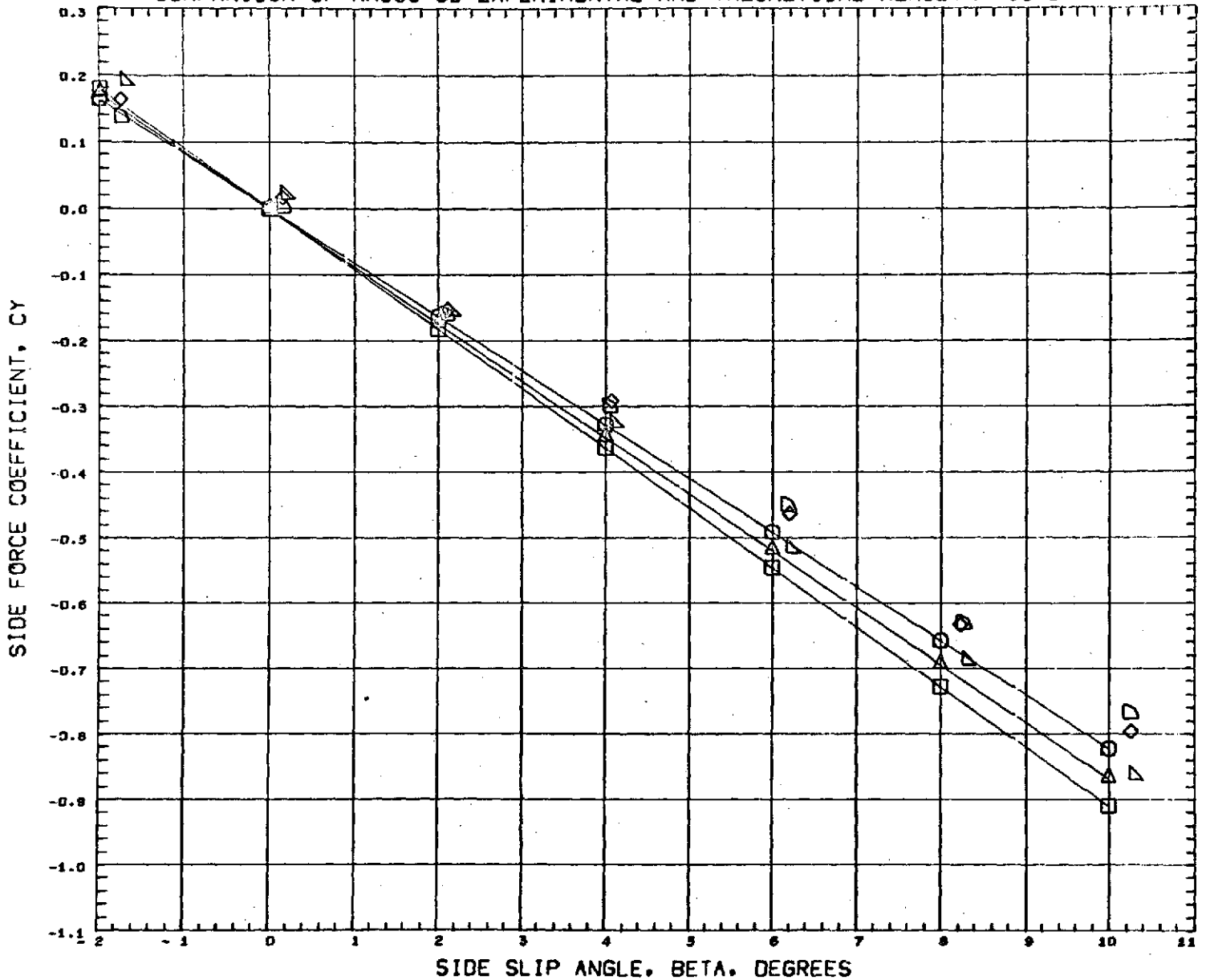
Fig. 9b - Comparison of Theoretical and Experimental Yawing Moment Coefficients for the 5B Configuration with 0° Compression Flap Deflection



DATA SET SYMBOL	CONFIGURATION DESCRIPTION	ALPHA	ELVATR	
(A00012)	AMOOS 5B CONFIG FORWARD FLAP ARC TEST	41.000	0.000	SEE THE ASSOCIATED DATA DOCUMENT FOR REFERENCE CHARACTERISTICS
(A00009)	AMOOS 5B CONFIG FORWARD FLAP ARC TEST	48.000	0.000	
(A00008)	AMOOS 5B CONFIG FORWARD FLAP ARC TEST	51.000	0.000	
(AMY229)	AMOOS CONFIGURATION 5B DEL ELE=0	40.000	0.000	
(AMY233)	AMOOS CONFIGURATION 5B DEL ELE=0	45.000	0.000	
(AMY237)	AMOOS CONFIGURATION 5B DEL ELE=0	50.000	0.000	
MACH	10.270 26.800			

Fig. 9c - Comparison of Theoretical and Experimental Rolling Moment Coefficients for the 5B Configuration with 0° Compression Flap Deflection

COMPARISON OF AMOOS 5B EXPERIMENTAL AND THEORETICAL AERODYNAMIC DATA



DATA SET SYMBOL	CONFIGURATION DESCRIPTION	ALPHA	ELVATR	
(A00007)	AMOOS 5B CONFIG AFT FLAP ARC TEST	51.000	0.000	SEE THE ASSOCIATED DATA DOCUMENT FOR REFERENCE CHARACTERISTICS
(A00010)	AMOOS 5B CONFIG AFT FLAP ARC TEST	46.000	0.000	
(A00011)	AMOOS 5B CONFIG AFT FLAP ARC TEST	41.000	0.000	
(AMY269)	AMOOS CONFIGURATION 5B BAS ROT DEL ELE=0	40.000	0.000	
(AMY273)	AMOOS CONFIGURATION 5B BAS ROT DEL ELE=0	45.000	0.000	
(AMY277)	AMOOS CONFIGURATION 5B BAS ROT DEL ELE=0	50.000	0.000	
MACH	10.270 26.800			

Fig. 9d - Comparison of Theoretical and Experimental Side Force Coefficients for the 5B Configuration with 0° Expansion Flap Deflection.

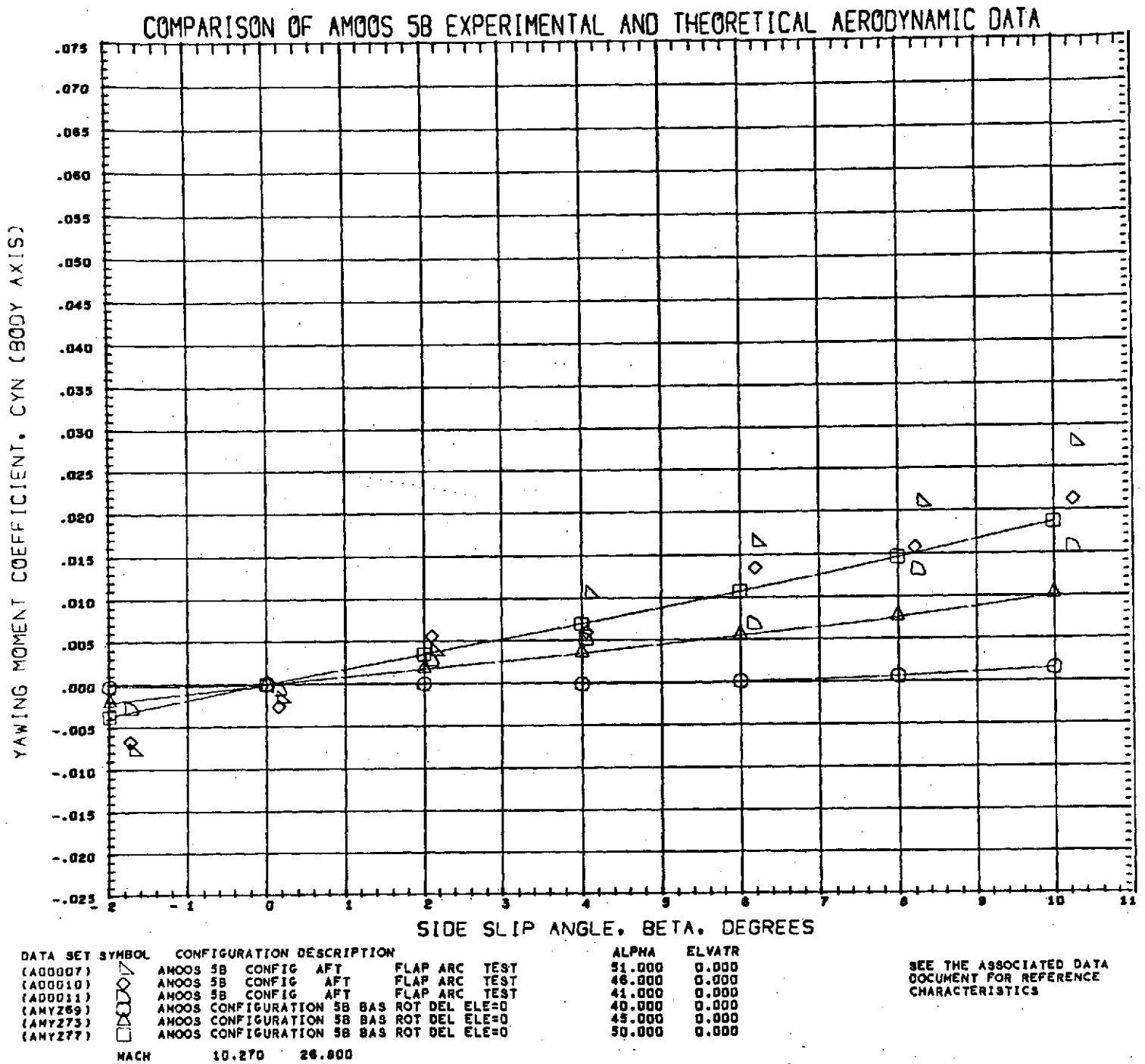
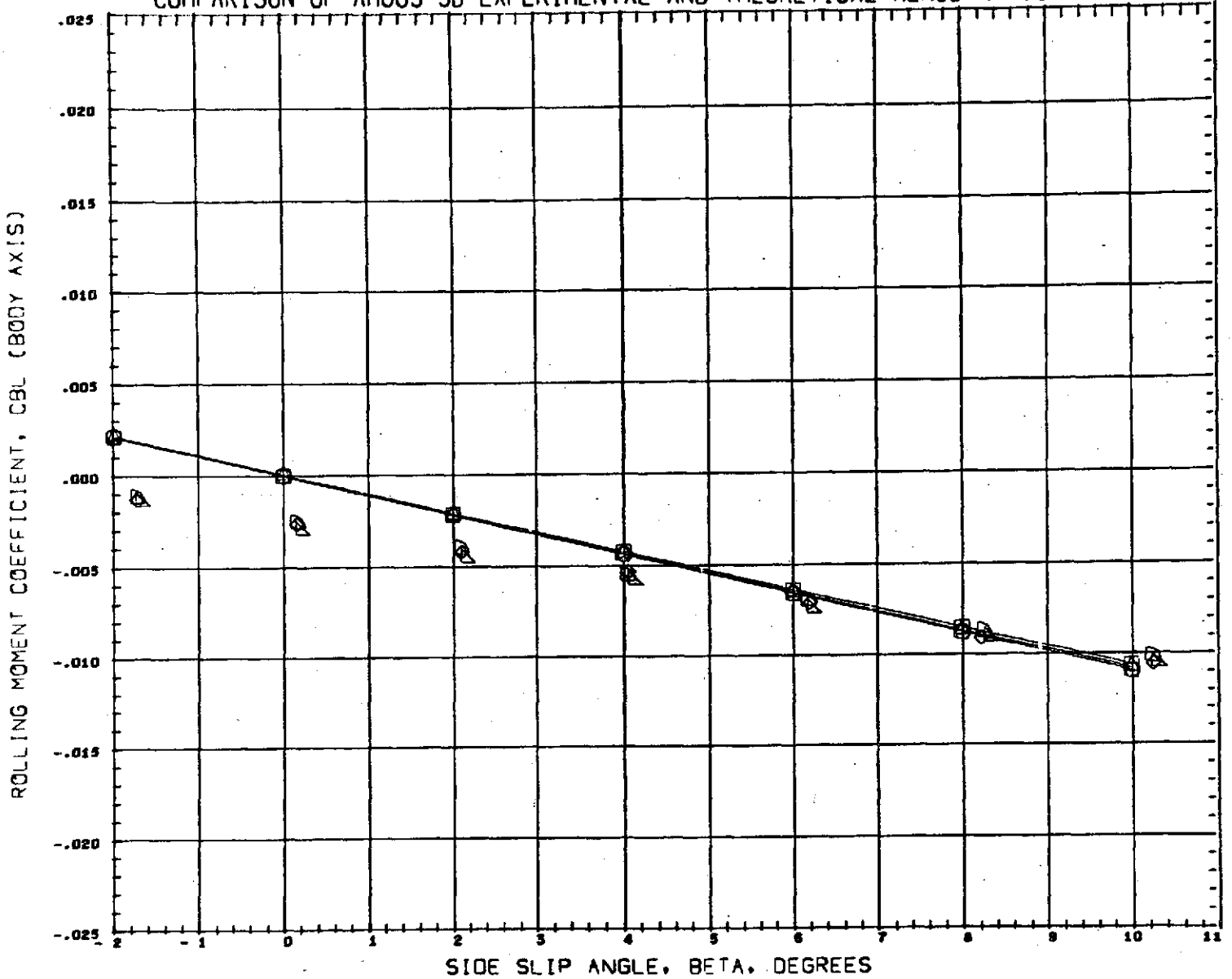


Fig. 9e - Comparison of Theoretical and Experimental Yawing Moment Coefficients for the 5B Configuration with 0° Expansion Flap Deflection

COMPARISON OF AMOOS 5B EXPERIMENTAL AND THEORETICAL AERODYNAMIC DATA



DATA SET SYMBOL	CONFIGURATION DESCRIPTION	ALPHA	ELVATR
(AG0007)	AMOOS 5B CONFIG AFT FLAP ARC TEST	51.000	0.000
(AG0010)	AMOOS 5B CONFIG AFT FLAP ARC TEST	46.000	0.000
(AG0011)	AMOOS 5B CONFIG AFT FLAP ARC TEST	41.000	0.000
(AHY269)	AMOOS CONFIGURATION 5B BAS ROT DEL ELE=0	40.000	0.000
(AHY273)	AMOOS CONFIGURATION 5B BAS ROT DEL ELE=0	45.000	0.000
(AHY277)	AMOOS CONFIGURATION 5B BAS ROT DEL ELE=0	50.000	0.000

MACH      10.270    26.800

SEE THE ASSOCIATED DATA DOCUMENT FOR REFERENCE CHARACTERISTICS

Fig. 9f - Comparison of Theoretical and Experimental Rolling Moment Coefficients for the 5B Configuration with 0° Expansion Flap Deflection



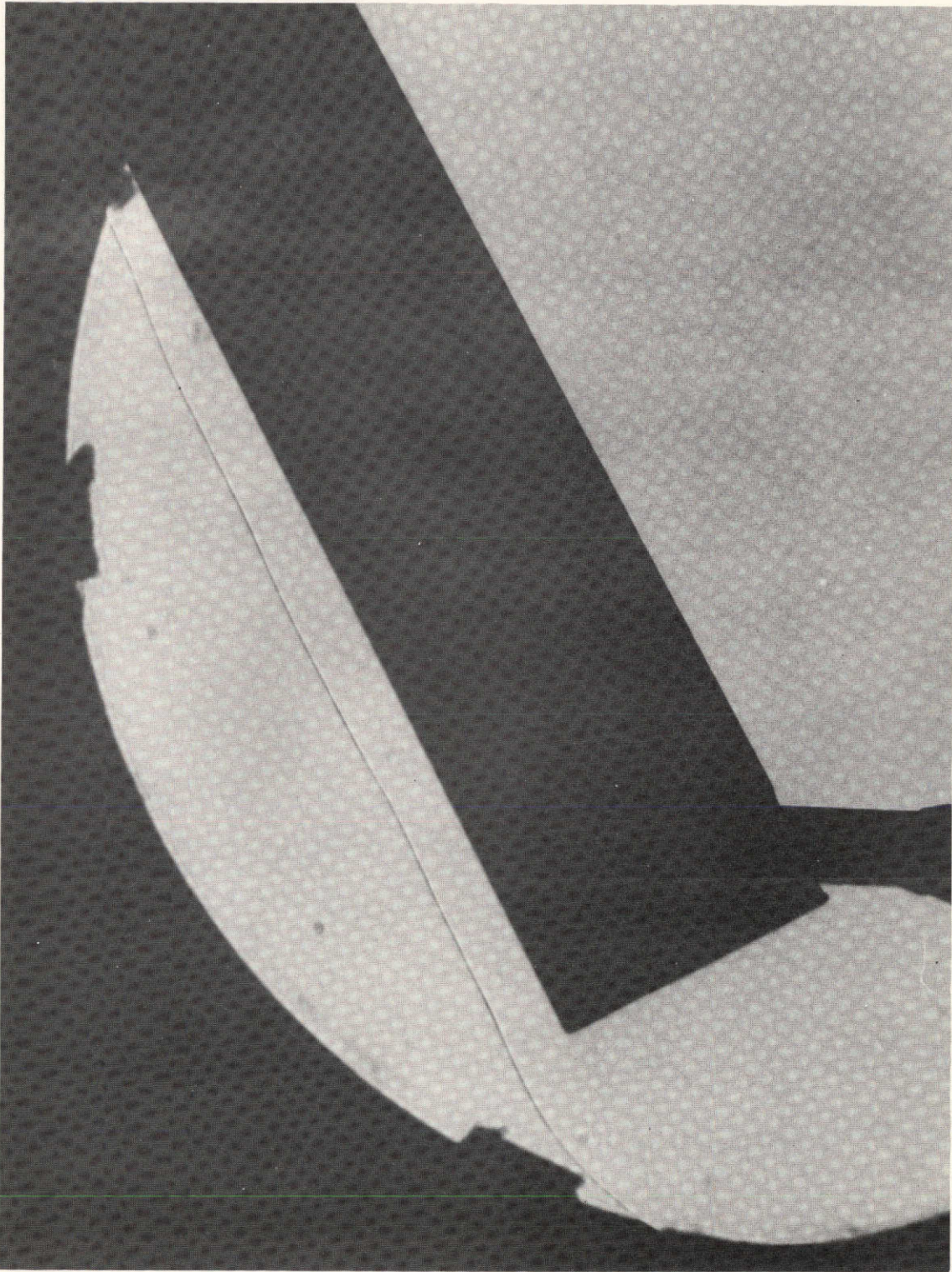
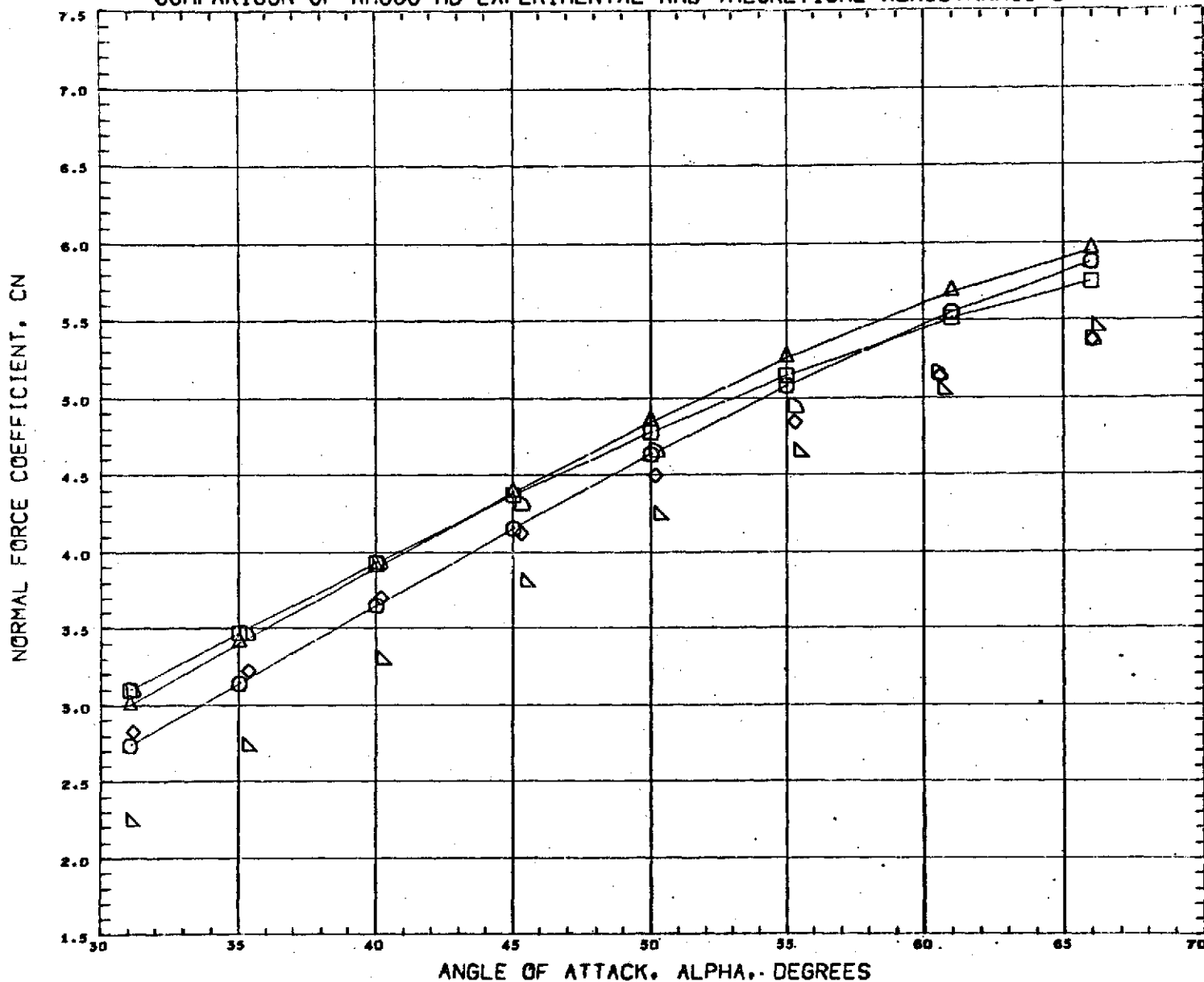


Fig. 10a - Shadowgraph of the Basic (No Flap) HB Configuration  
at an Angle of Attack of  $65^{\circ}$

COMPARISON OF AMOOS HB EXPERIMENTAL AND THEORETICAL AERODYNAMIC DATA



DATA SET SYMBOL	CONFIGURATION DESCRIPTION	ELVATR	BETA	
(A00013)	AMOOS HB CONFIG FORWARD FLAP ARC TEST	0.000	0.000	SEE THE ASSOCIATED DATA DOCUMENT FOR REFERENCE CHARACTERISTICS
(A00015)	AMOOS HB CONFIG FORWARD FLAP ARC TEST	20.000	0.000	
(A00016)	AMOOS HB CONFIG FORWARD FLAP ARC TEST	40.000	0.000	
(AMY205)	AMOOS CONFIGURATION HB DEL ELE=0	0.000	0.000	
(AMY207)	AMOOS CONFIGURATION HB DEL ELE=20	20.000	0.000	
(AMY208)	AMOOS CONFIGURATION HB DEL ELE=40	40.000	0.000	
MACH		10.270	26.800	

Fig. 10b - Comparison of Theoretical and Experimental Normal Force Coefficients for the HB Configuration with Compression Flap Deflections



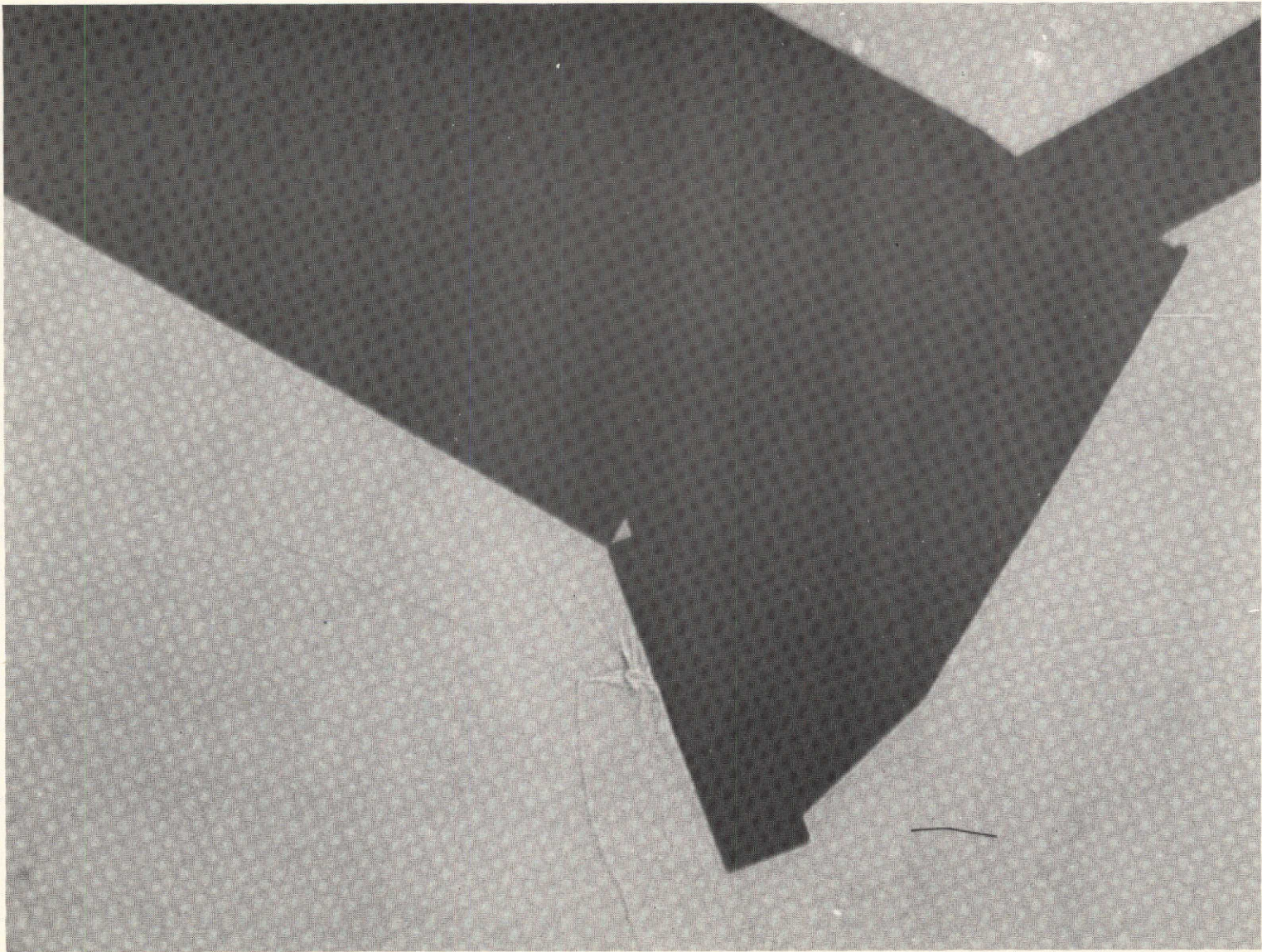


Fig. 10c - Shadowgraph of the HB Model with the Compression Flap Deflected  $40^\circ$  at a Model Angle of Attack of  $30^\circ$



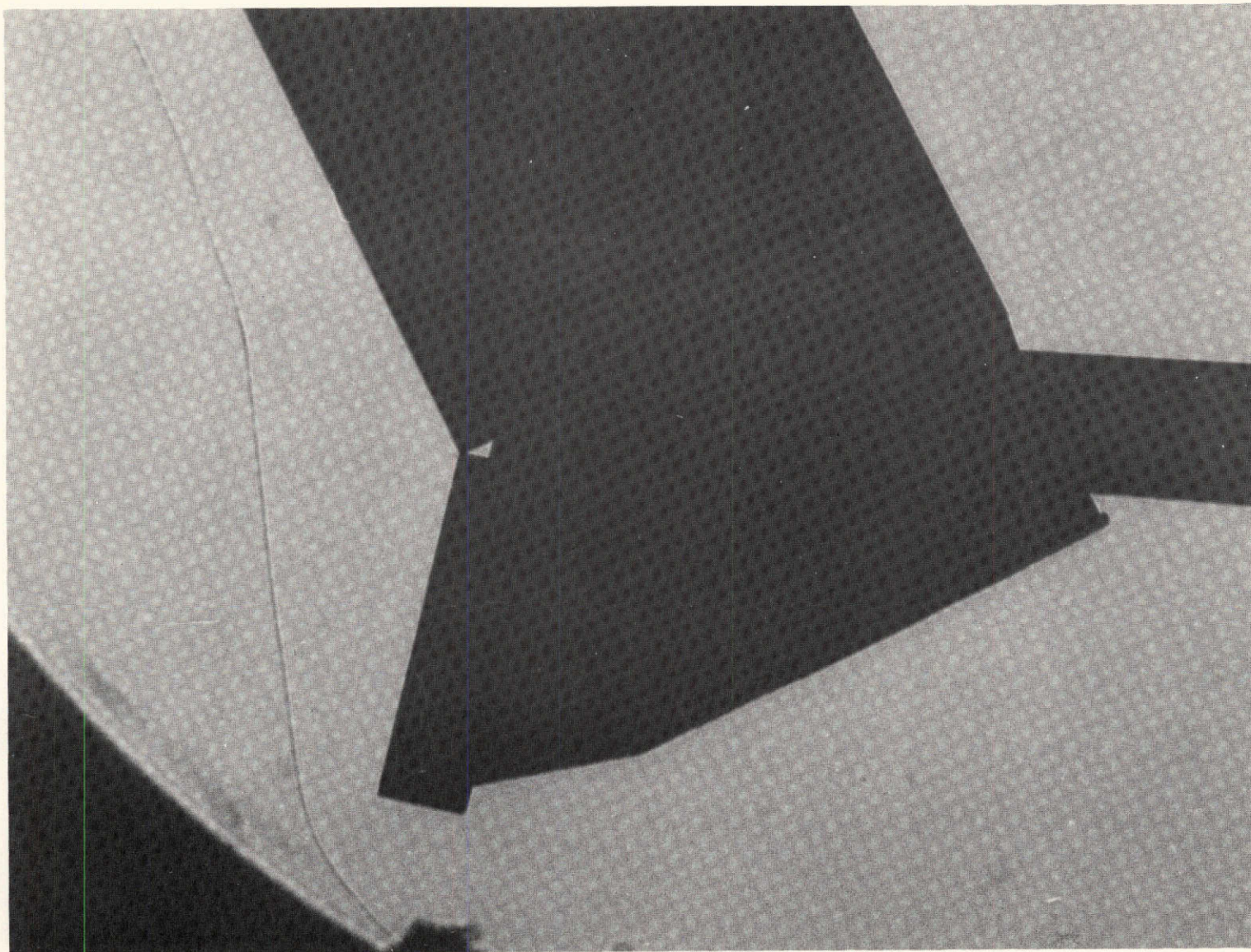
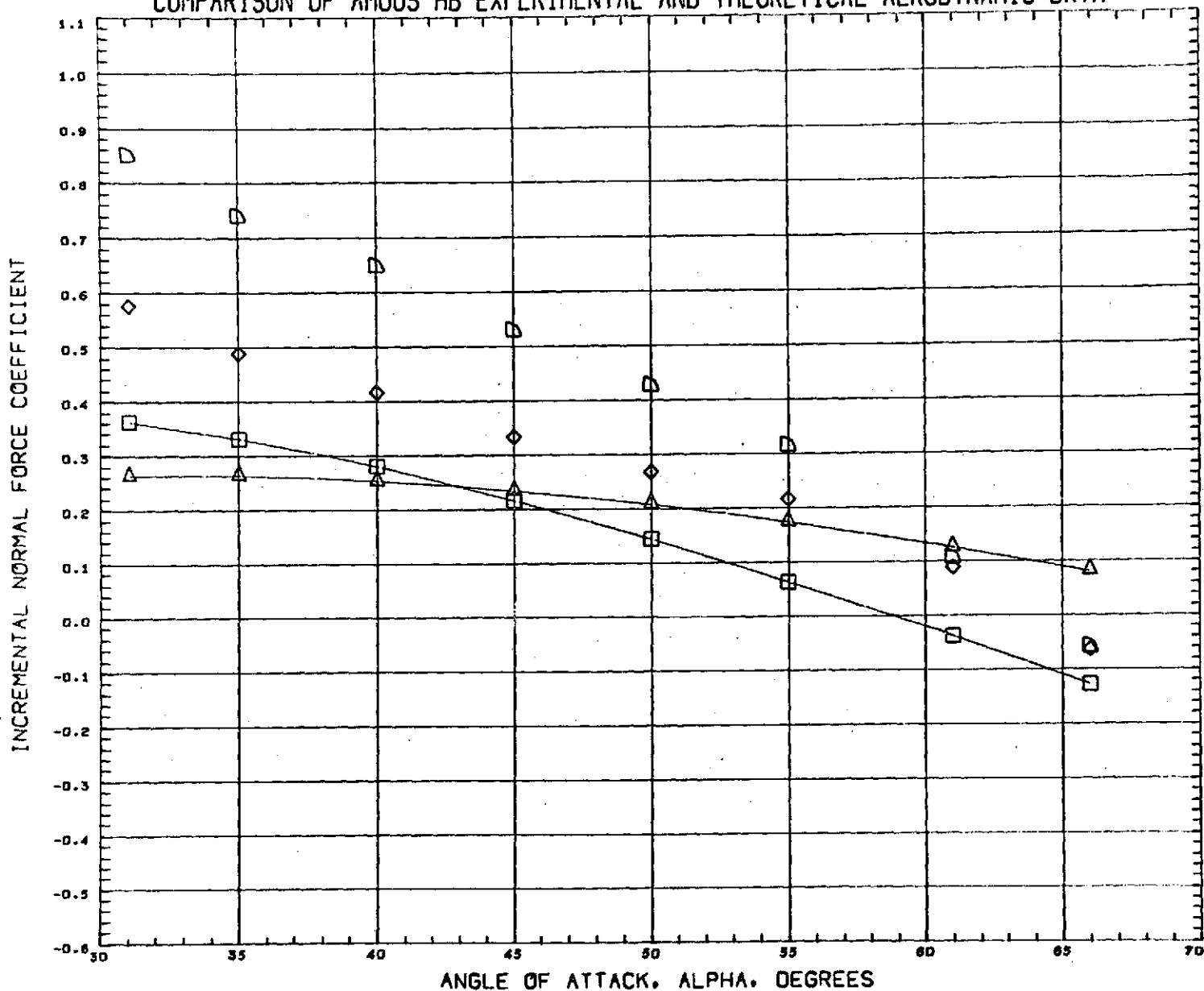


Fig. 10d - Shadowgraph of the HB Model with the Compression Flap Deflected  $40^\circ$  at a Model Angle of Attack of  $65^\circ$

COMPARISON OF AMOOS HB EXPERIMENTAL AND THEORETICAL AERODYNAMIC DATA



DATA SET SYMBOL	CONFIGURATION DESCRIPTION	ELVATR	BETA	
(DLCM07)	AMOOS CONFIGURATION HB DEL ELE=20	20.000	0.000	SEE THE ASSOCIATED DATA DOCUMENT FOR REFERENCE CHARACTERISTICS
(DLCM08)	AMOOS CONFIGURATION HB DEL ELE=40	40.000	0.000	
(DLCM15)	AMOOS HB CONFIG FOREWARD FLAP ARC TEST	20.000	0.000	
(DLCM16)	AMOOS HB CONFIG FOREWARD FLAP ARC TEST	40.000	0.000	

MACH 10.270 26.800

Fig. 10e - Comparison of Theoretical and Experimental Incremental Normal Force Coefficients for the HB Configuration with Compression Flap Deflections

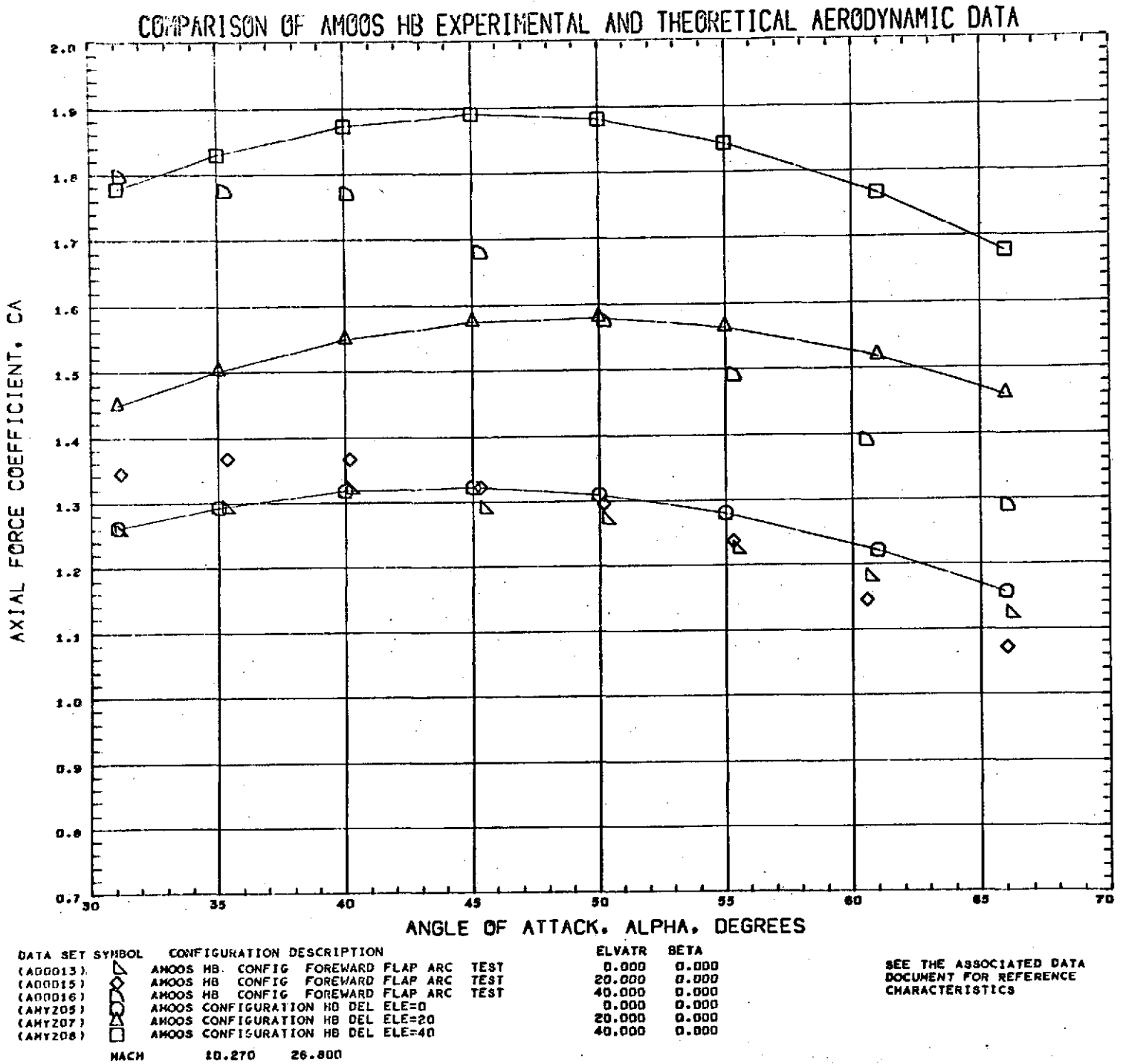
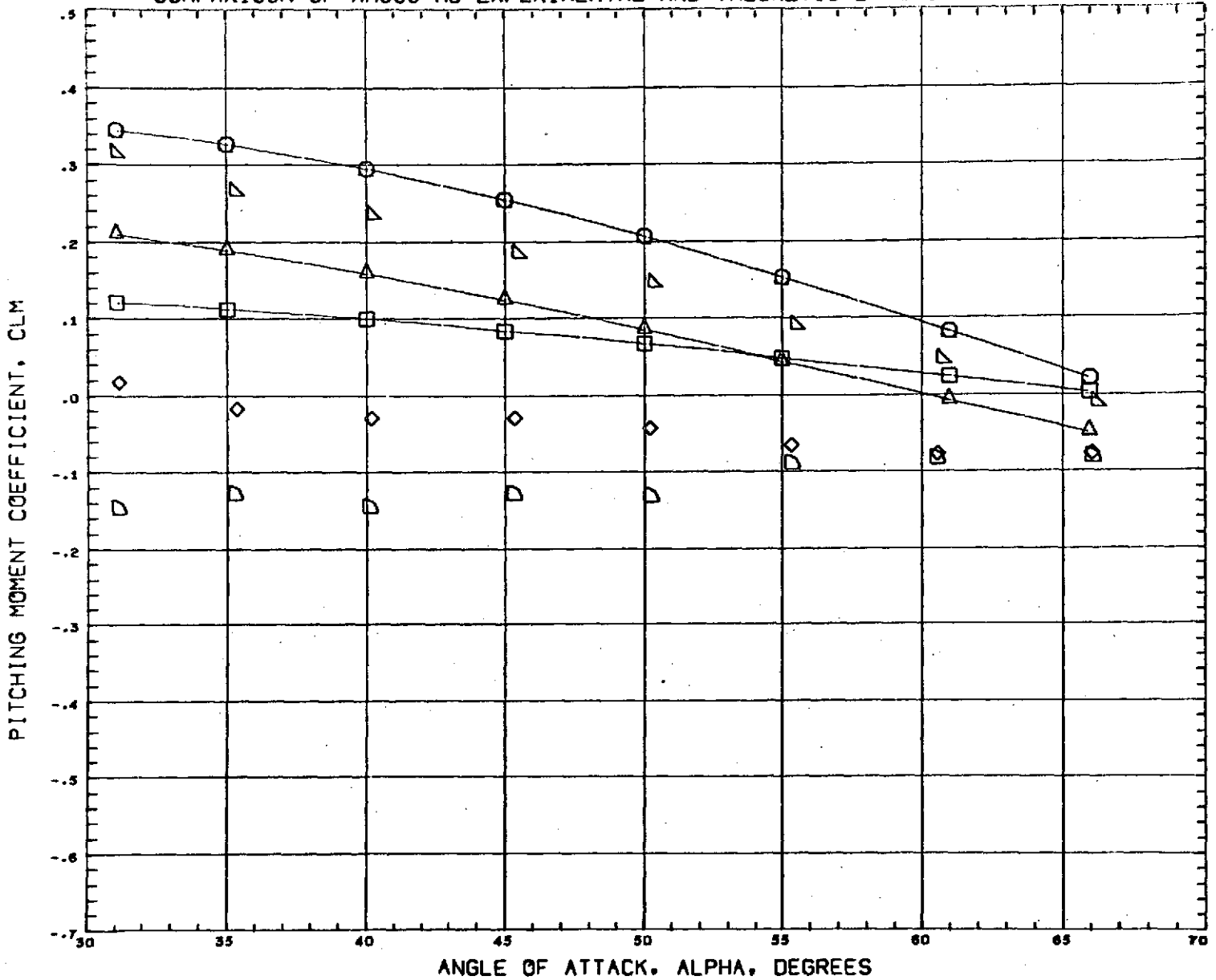


Fig. 10f - Comparison of Theoretical and Experimental Axial Force Coefficients for the HB Configuration with Compression Flap Deflections



COMPARISON OF AMOOS HB EXPERIMENTAL AND THEORETICAL AERODYNAMIC DATA

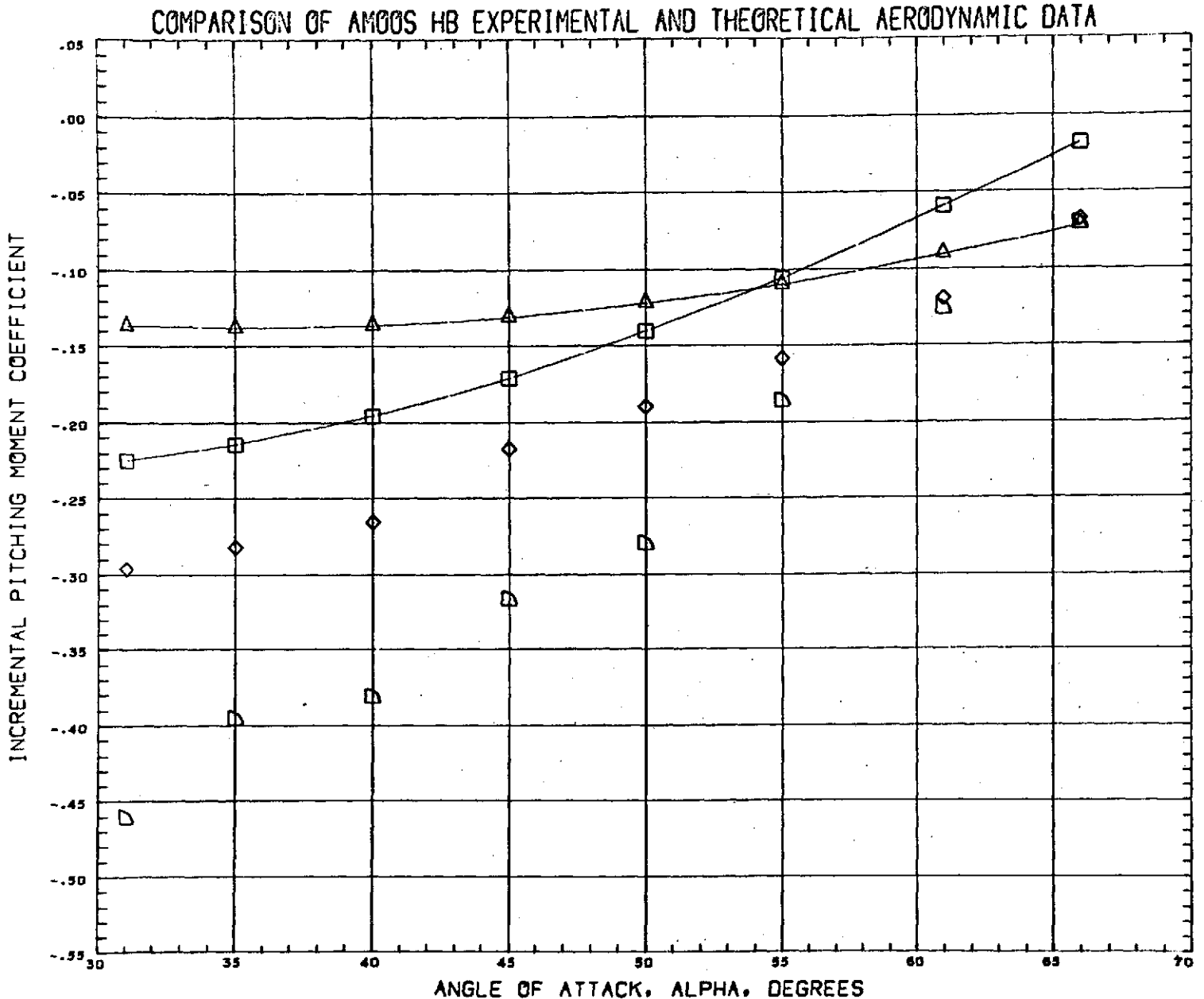


DATA SET SYMBOL	CONFIGURATION DESCRIPTION	ELVATR	BETA
(A00013)	AMOOS HB CONFIG FORWARD FLAP ARC TEST	0.000	0.000
(A00015)	AMOOS HB CONFIG FORWARD FLAP ARC TEST	20.000	0.000
(A00016)	AMOOS HB CONFIG FORWARD FLAP ARC TEST	40.000	0.000
(AMY205)	AMOOS CONFIGURATION HB DEL ELE=0	0.000	0.000
(AMY207)	AMOOS CONFIGURATION HB DEL ELE=20	20.000	0.000
(AMY208)	AMOOS CONFIGURATION HB DEL ELE=40	40.000	0.000

SEE THE ASSOCIATED DATA DOCUMENT FOR REFERENCE CHARACTERISTICS

MACH      10.270      26.800

Fig. 10g - Comparison of Theoretical and Experimental Pitching Moment Coefficients for the HB Configuration with Compression Flap Deflections



DATA SET SYMBOL	CONFIGURATION DESCRIPTION	ELVATR	BETA	
(DLCH07)	AMOOS CONFIGURATION HB DEL ELE=20	20.000	0.000	SEE THE ASSOCIATED DATA DOCUMENT FOR REFERENCE CHARACTERISTICS
(DLCH08)	AMOOS CONFIGURATION HB DEL ELE=40	40.000	0.000	
(DLCH15)	AMOOS HB CONFIG FORWARD FLAP ARC TEST	20.000	0.000	
(DLCH16)	AMOOS HB CONFIG FORWARD FLAP ARC TEST	40.000	0.000	

MACH            10.270    26.800

Fig. 10h - Comparison of Theoretical and Experimental Incremental Pitching Moment Coefficients for the HB Configuration with Compression Flap Deflections

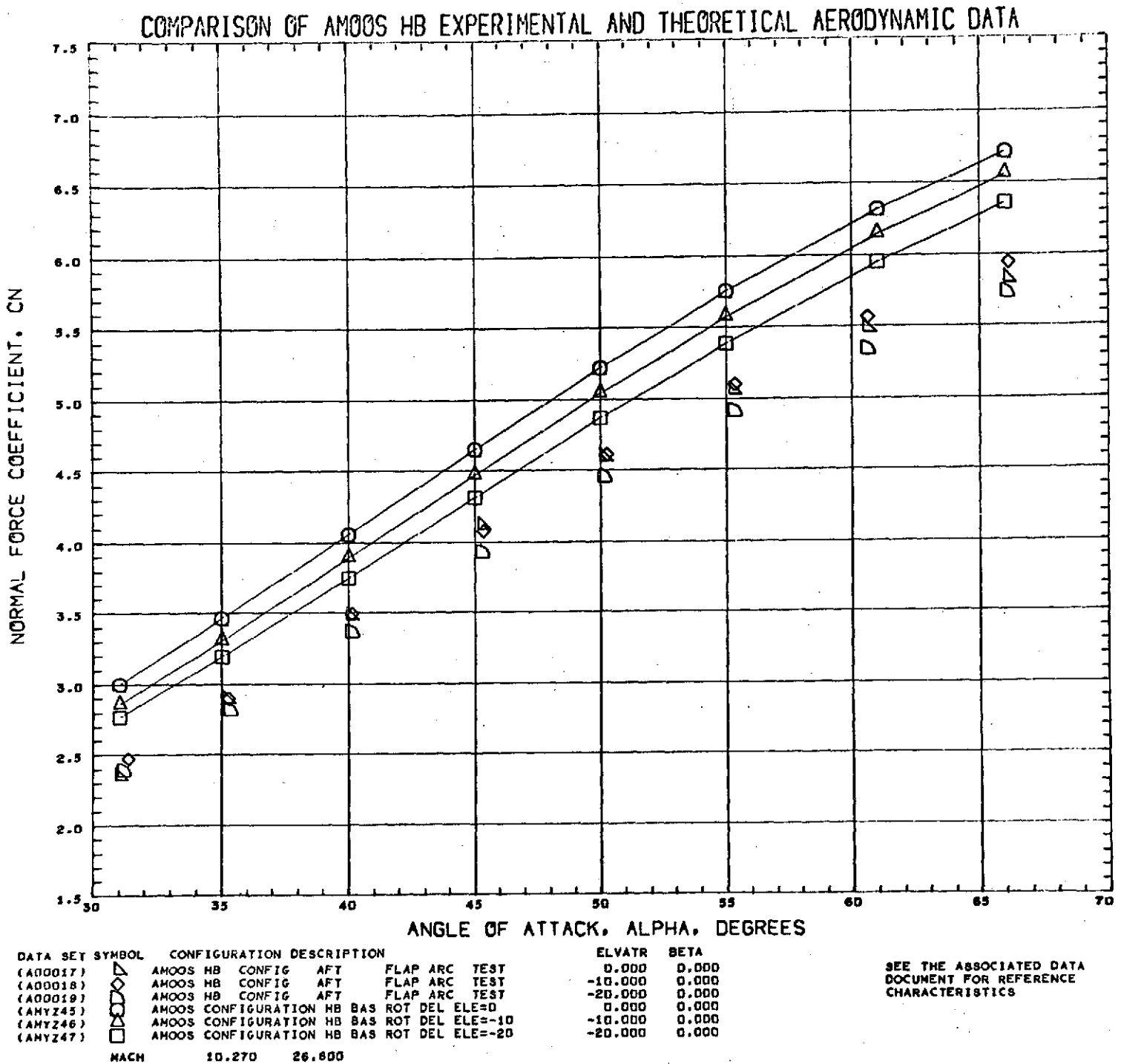
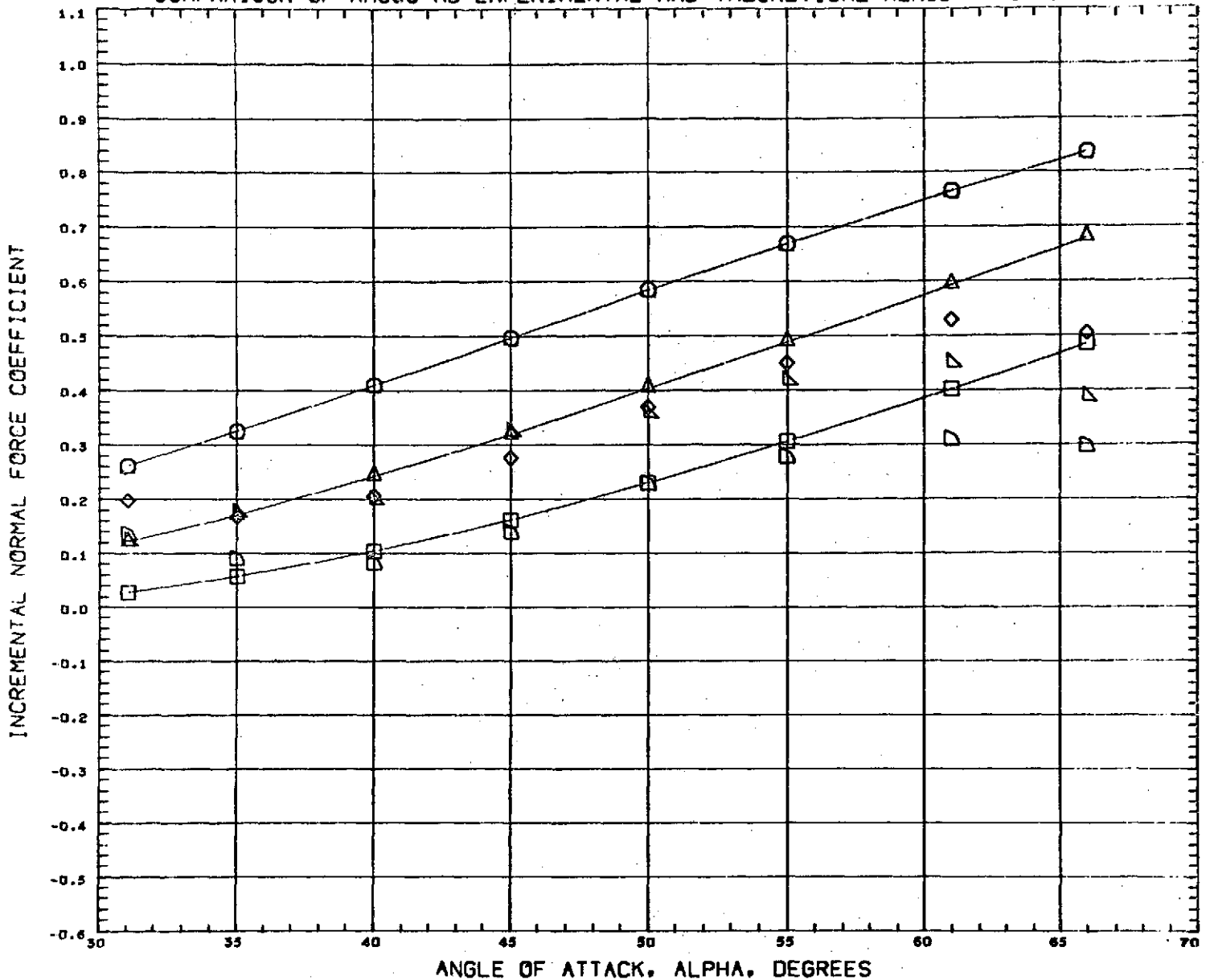


Fig. 10i - Comparison of Theoretical and Experimental Normal Force Coefficients for the HB Configuration with Expansion Flap Deflections

COMPARISON OF AMOOS HB EXPERIMENTAL AND THEORETICAL AERODYNAMIC DATA



DATA SET	SYMBOL	CONFIGURATION DESCRIPTION	ELVATR	BETA	
(DLCH45)	○	AMOOS CONFIGURATION HB BAS ROT DEL ELE=0	0.000	0.000	SEE THE ASSOCIATED DATA DOCUMENT FOR REFERENCE CHARACTERISTICS
(DLCH46)	△	AMOOS CONFIGURATION HB BAS ROT DEL ELE=-10	-10.000	0.000	
(DLCH47)	◇	AMOOS CONFIGURATION HB BAS ROT DEL ELE=-20	-20.000	0.000	
(DLCH17)	□	AMOOS HB CONFIG AFT FLAP ARC TEST	0.000	0.000	
(DLCH18)	◇	AMOOS HB CONFIG AFT FLAP ARC TEST	-10.000	0.000	
(DLCH19)	□	AMOOS HB CONFIG AFT FLAP ARC TEST	-20.000	0.000	
MACH		10.270 26.800			

Fig. 10j - Comparison of Theoretical and Experimental Incremental Normal Force Coefficients for the HB Configuration with Expansion Flap Deflections

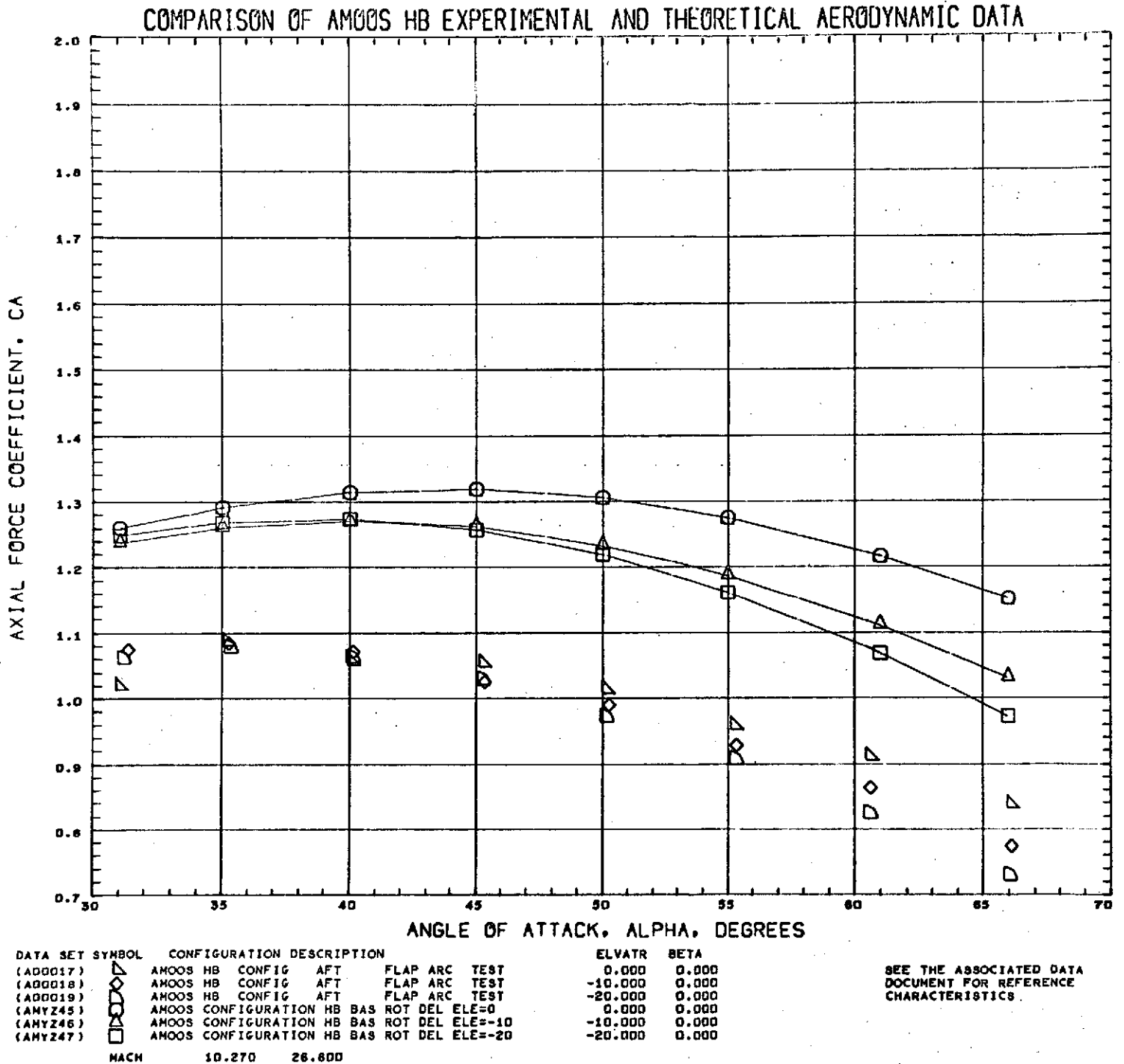
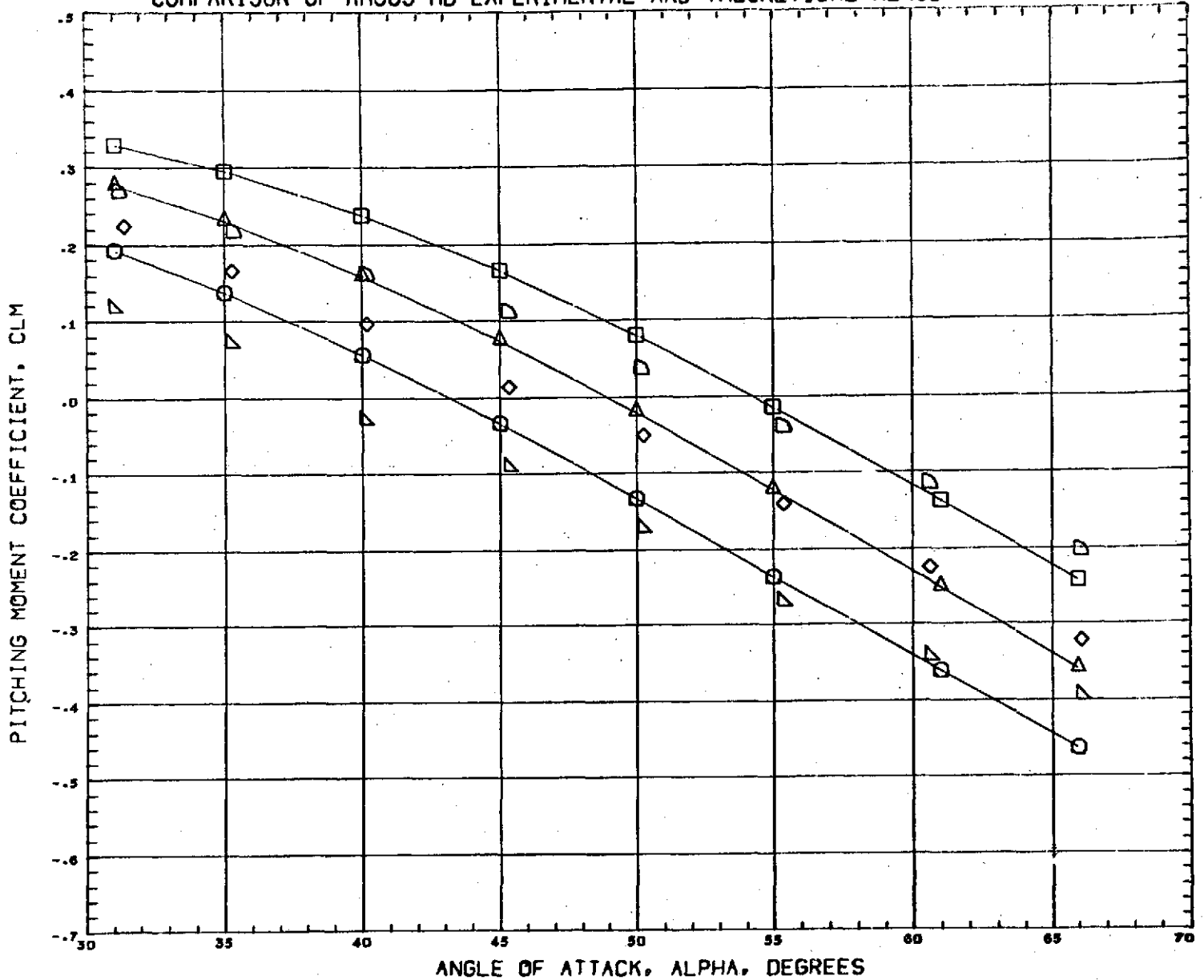


Fig. 10k - Comparison of Theoretical and Experimental Axial Force Coefficients for the HB Configuration with Expansion Flap Deflections



COMPARISON OF AMOOS HB EXPERIMENTAL AND THEORETICAL AERODYNAMIC DATA



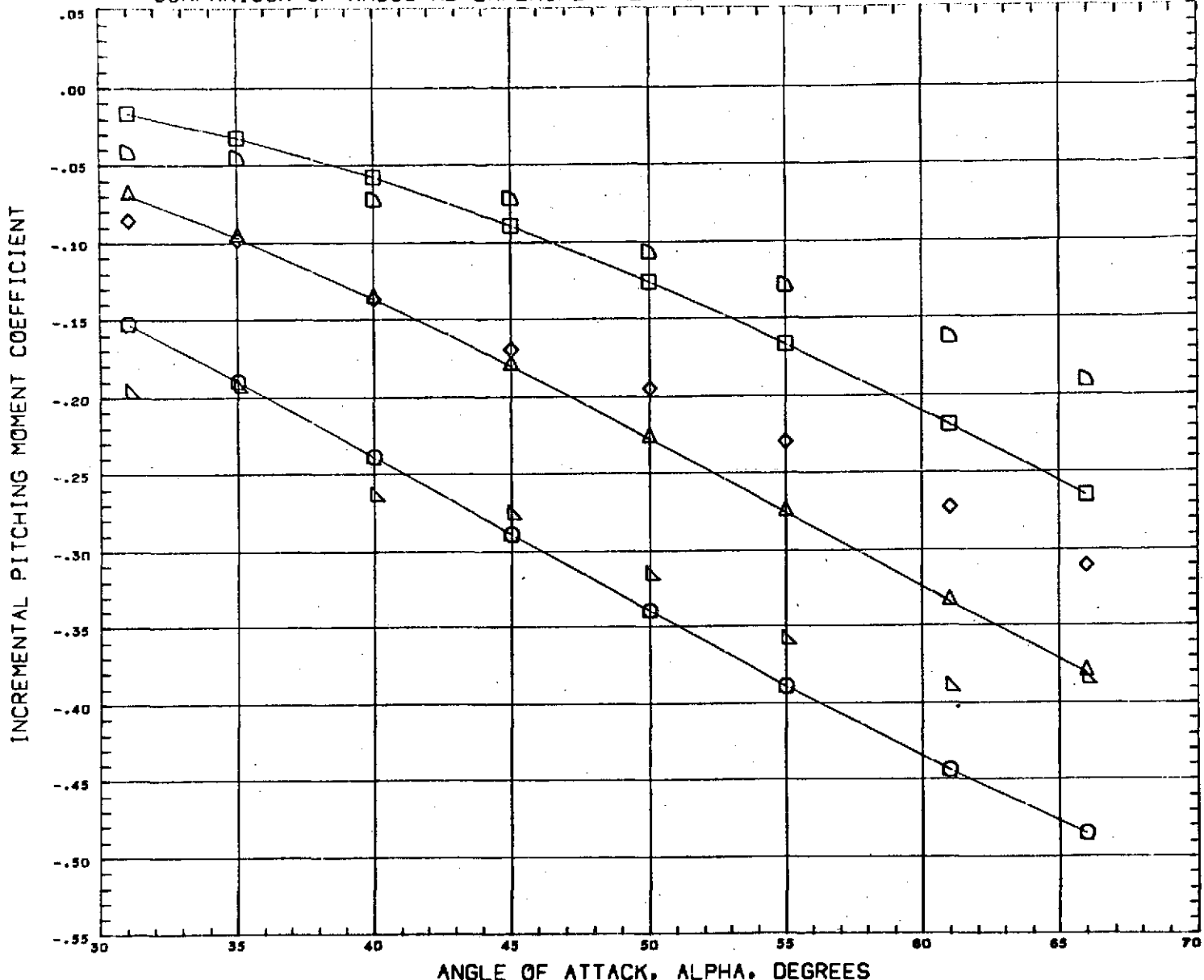
DATA SET SYMBOL	CONFIGURATION DESCRIPTION	ELVATR	BETA
(A00017)	AMOOS HB CONFIG AFT FLAP ARC TEST	0.000	0.000
(A00018)	AMOOS HB CONFIG AFT FLAP ARC TEST	-10.000	0.000
(A00019)	AMOOS HB CONFIG AFT FLAP ARC TEST	-20.000	0.000
(AMY245)	AMOOS CONFIGURATION HB BAS ROT DEL ELE=0	0.000	0.000
(AMY246)	AMOOS CONFIGURATION HB BAS ROT DEL ELE=-10	-10.000	0.000
(AMY247)	AMOOS CONFIGURATION HB BAS ROT DEL ELE=-20	-20.000	0.000

MACH 10.270 26.800

SEE THE ASSOCIATED DATA DOCUMENT FOR REFERENCE CHARACTERISTICS

Fig. 10l - Comparison of Theoretical and Experimental Pitching Moment Coefficients for the HB Configuration with Expansion Flap Deflections

COMPARISON OF AMOOS HB EXPERIMENTAL AND THEORETICAL AERODYNAMIC DATA



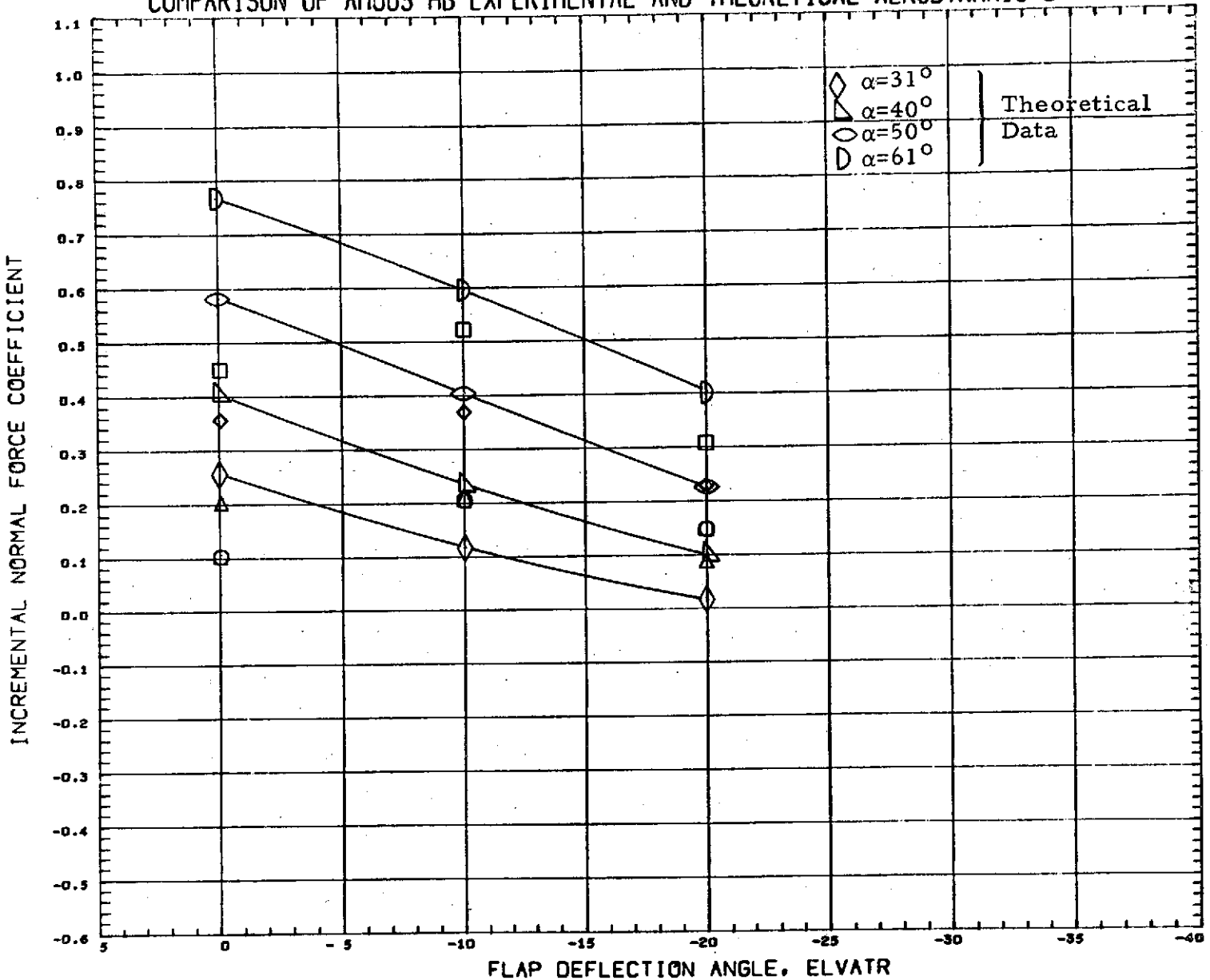
DATA SET SYMBOL	CONFIGURATION DESCRIPTION	ELVATR	BETA
(DLCM45)	AMOOS CONFIGURATION HB BAS ROT DEL ELE=0	0.000	0.000
(DLCM46)	AMOOS CONFIGURATION HB BAS ROT DEL ELE=-10	-10.000	0.000
(DLCM47)	AMOOS CONFIGURATION HB BAS ROT DEL ELE=-20	-20.000	0.000
(DLCM17)	AMOOS HB CONFIG AFT FLAP ARC TEST	0.000	0.000
(DLCM18)	AMOOS HB CONFIG AFT FLAP ARC TEST	-10.000	0.000
(DLCM19)	AMOOS HB CONFIG AFT FLAP ARC TEST	-20.000	0.000

MACH 10.270 26.800

SEE THE ASSOCIATED DATA DOCUMENT FOR REFERENCE CHARACTERISTICS

Fig. 10m - Comparison of Theoretical and Experimental Incremental Pitching Moment Coefficients for the HB Configuration with Expansion Flap Deflections

COMPARISON OF AMOOS HB EXPERIMENTAL AND THEORETICAL AERODYNAMIC DATA

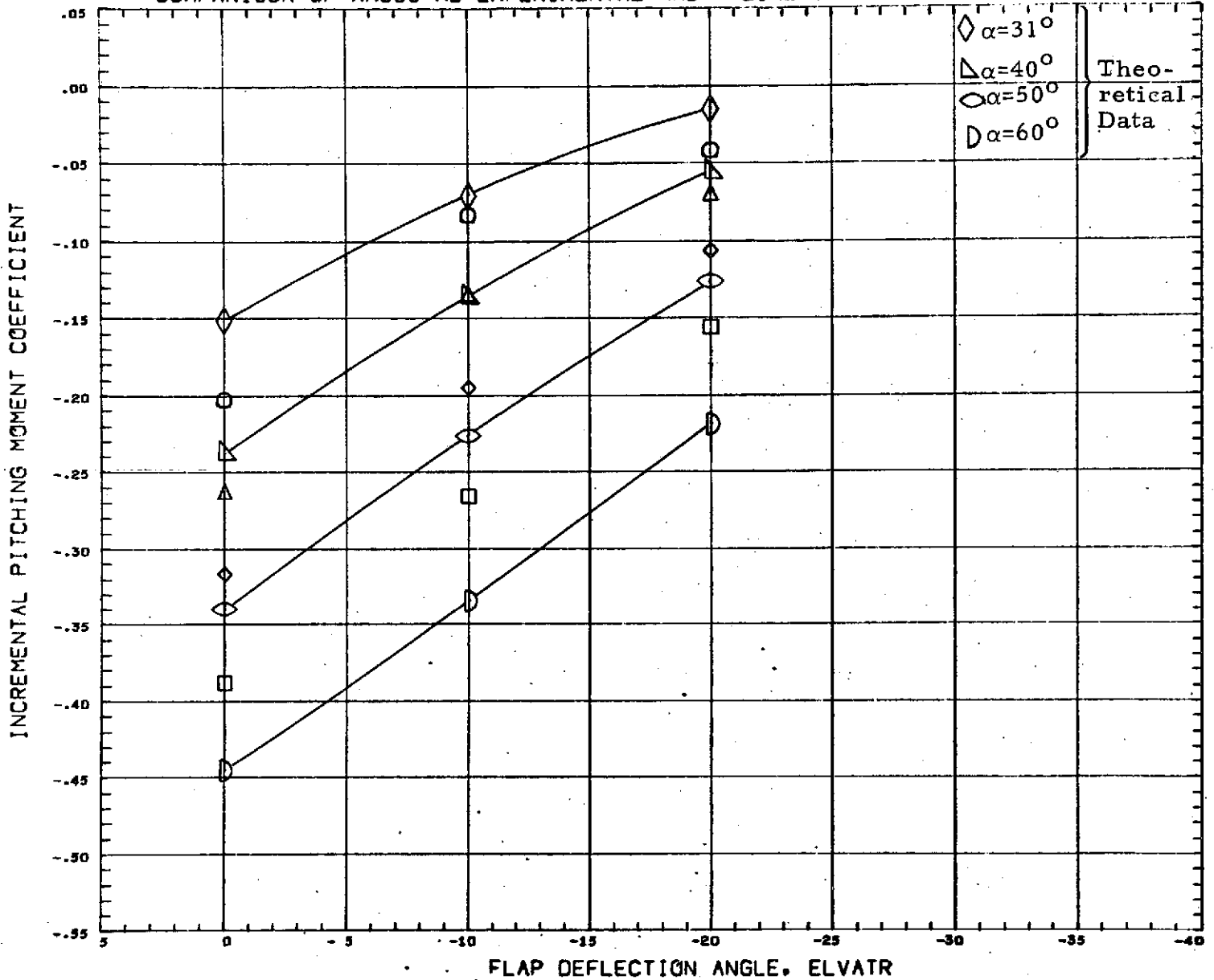


SYMBOL	ALPHA	PARAMETRIC VALUES				DATA SOURCE				REFERENCE INFORMATION		
		MACH	10.270	BETA	0.000	DATASET	ELVATR	DATASET	ELVATR	REFS	SCALE	UNIT
◇	30.000					DMCH17	0.000	DMCH18	- 10.000	168.948	0.000	Sq FT
△	40.000	RN/L	1.200			DMCH19	- 20.000	DMCH20	- 40.000	58.667	0.000	FT
○	50.000	PSTAT	0.022							58.667	0.000	FT
□	60.000	TSTAT	93.000	DYN PR	1.630					37.333	0.000	FT
										0.000	0.000	FT
										0.000	0.000	FY
										SCALE	0.000	

DATA HIST. CODE 1\*CI

Fig. 10n - Plot of Incremental Normal Force Coefficients as Functions of Expansion Flap Deflection Angles for the HB Configuration

COMPARISON OF AMOOS HB EXPERIMENTAL AND THEORETICAL AERODYNAMIC DATA



SYMBOL	ALPHA	PARAMETRIC VALUES				DATA SOURCE				REFERENCE INFORMATION		
		MACH	10.270	BETA	0.000	DATASET	ELVATR	DATASET	ELVATR	REFS		
◇	30.000									168.948	Sq	FT
△	40.000	RN/L	1.200							58.667	FT	
○	50.000	PSTAT	0.022			DNCH17	0.000	DNCH18	- 10.000	58.667	FT	
□	60.000	TSTAT	93.000	DYN PR	1.630	DNCH19	- 20.000	DNCH20	- 40.000	37.333	FT	
										YMRP	0.000	FT
										ZMRP	0.000	FT
										SCALE	0.000	

DATA HIST. CODE I&CI

Fig. 10o - Plot of Incremental Pitching Moment Coefficients as Functions of Expansion Flap Deflection Angles for the HB Configuration



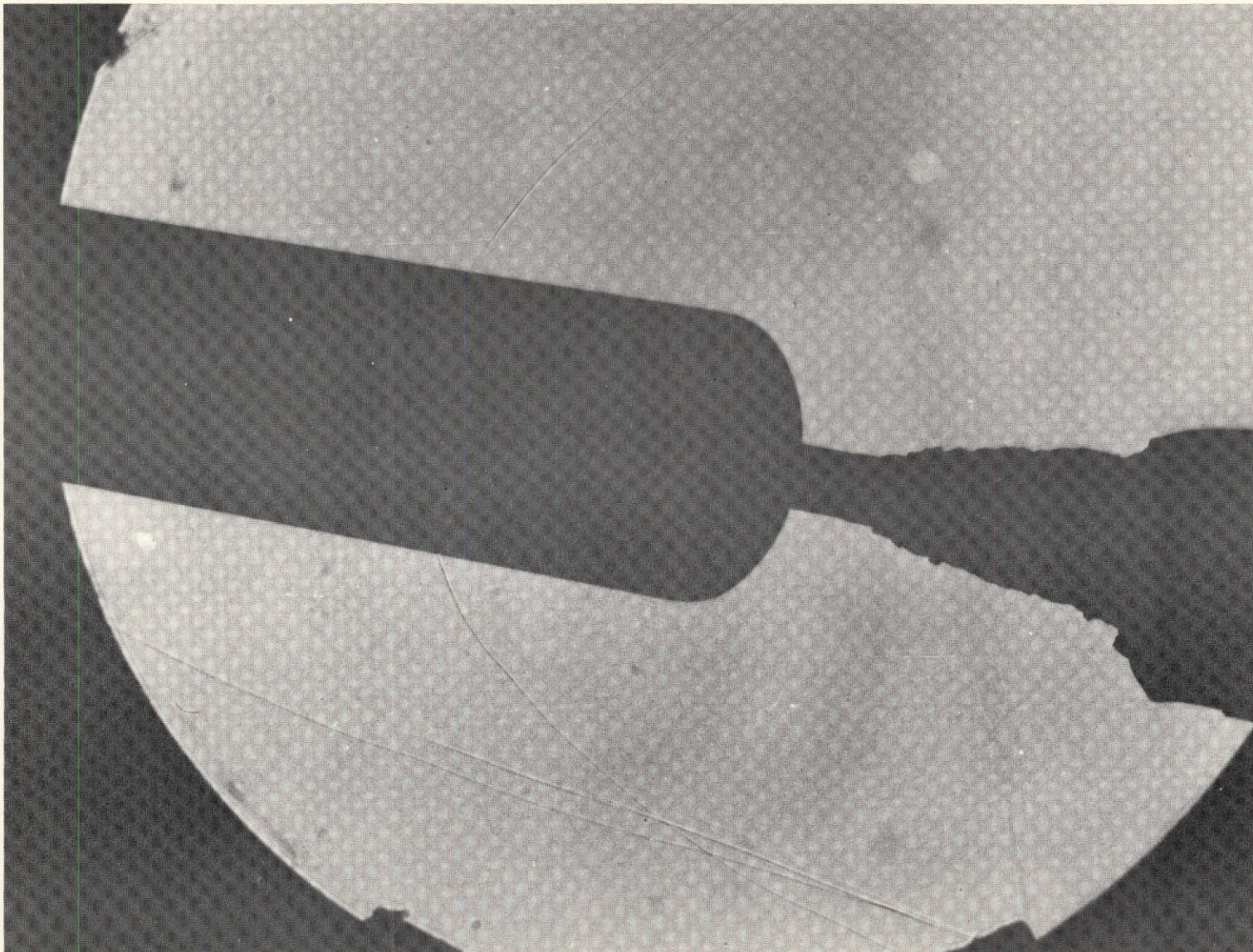
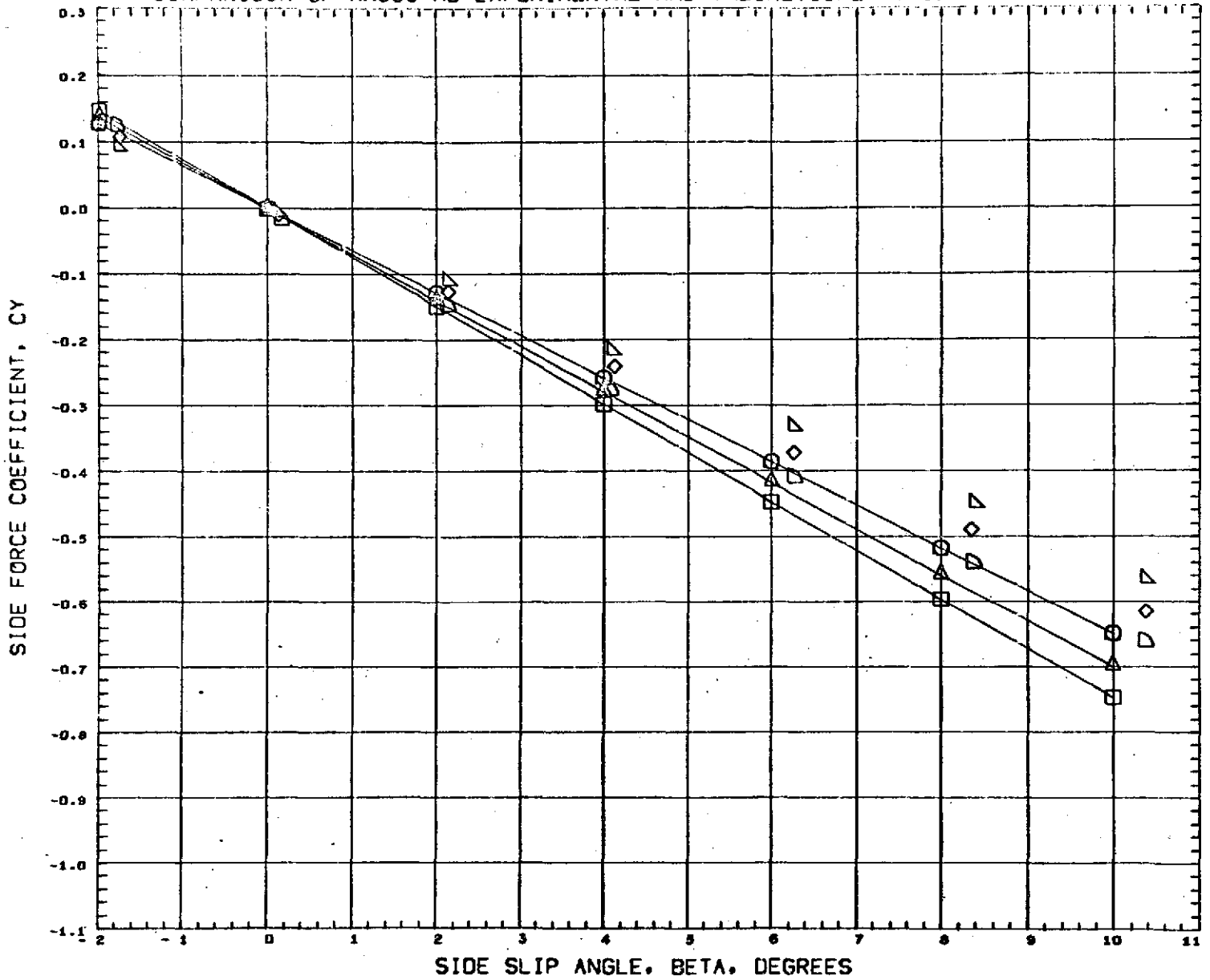


Fig. 11a - Shadowgraph of the HB Model at a Model Sideslip Angle of  $10^{\circ}$  with the Compression Flap Deflected

COMPARISON OF AMOOS HB EXPERIMENTAL AND THEORETICAL AERODYNAMIC DATA



DATA SET	SYMBOL	CONFIGURATION DESCRIPTION	ALPHA	ELVATR	
(A00030)	△	AMOOS HB CONFIG FORWARD FLAP ARC TEST	40.000	0.000	SEE THE ASSOCIATED DATA DOCUMENT FOR REFERENCE CHARACTERISTICS
(A00027)	◇	AMOOS HB CONFIG FORWARD FLAP ARC TEST	45.000	0.000	
(A00023)	□	AMOOS HB CONFIG FORWARD FLAP ARC TEST	50.000	0.000	
(AMYZ09)	○	AMOOS CONFIGURATION HB DEL ELE=0	40.000	0.000	
(AMYZ13)	○	AMOOS CONFIGURATION HB DEL ELE=0	45.000	0.000	
(AMYZ17)	□	AMOOS CONFIGURATION HB DEL ELE=0	50.000	0.000	
MACH		10.270 26.800			

Fig. 11b - Comparison of Theoretical and Experimental Side Force Coefficients for the HB Configuration with the Compression Flap Deflected 0° at the Angles of Attack of 40°, 45° and 50°

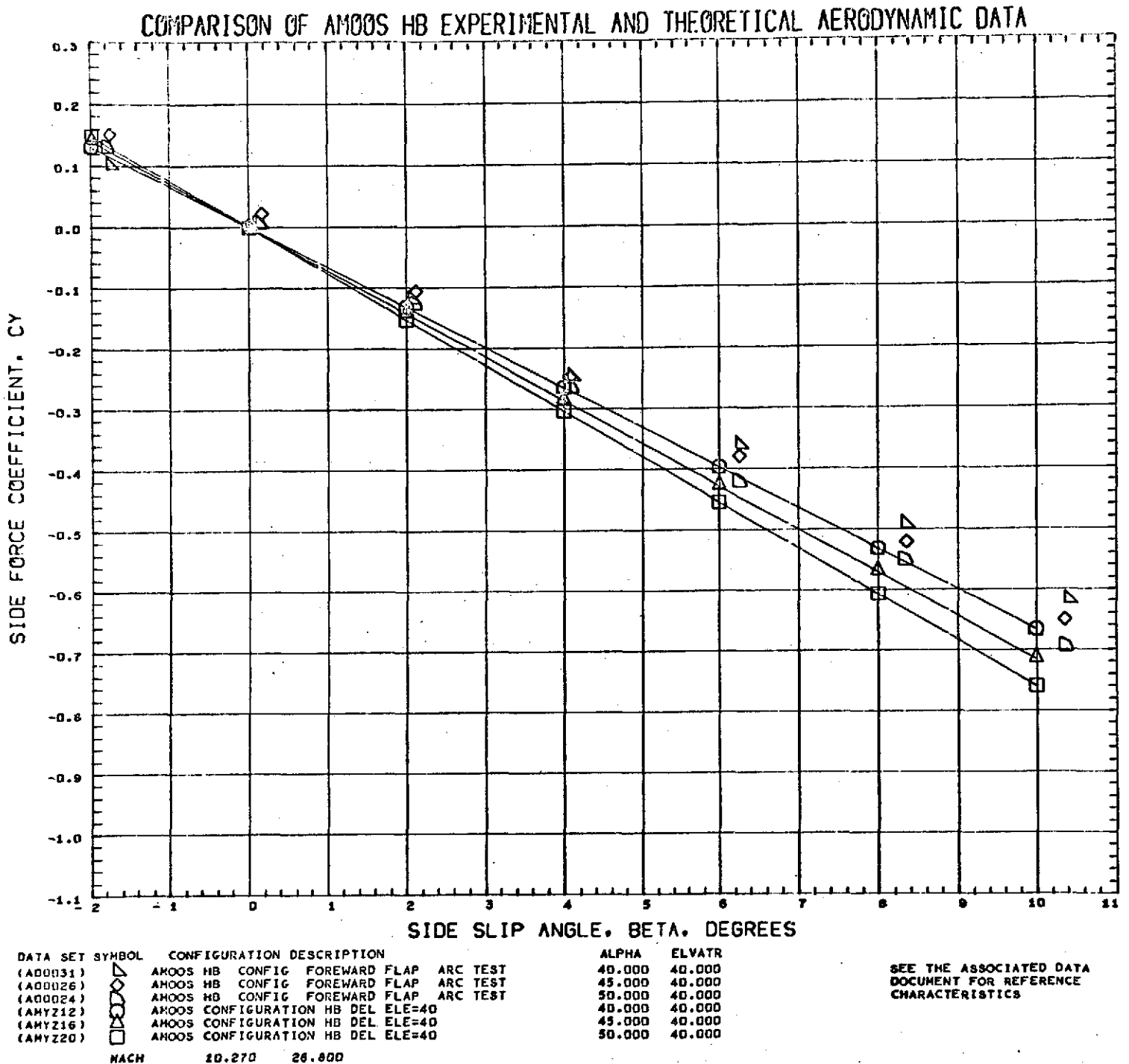
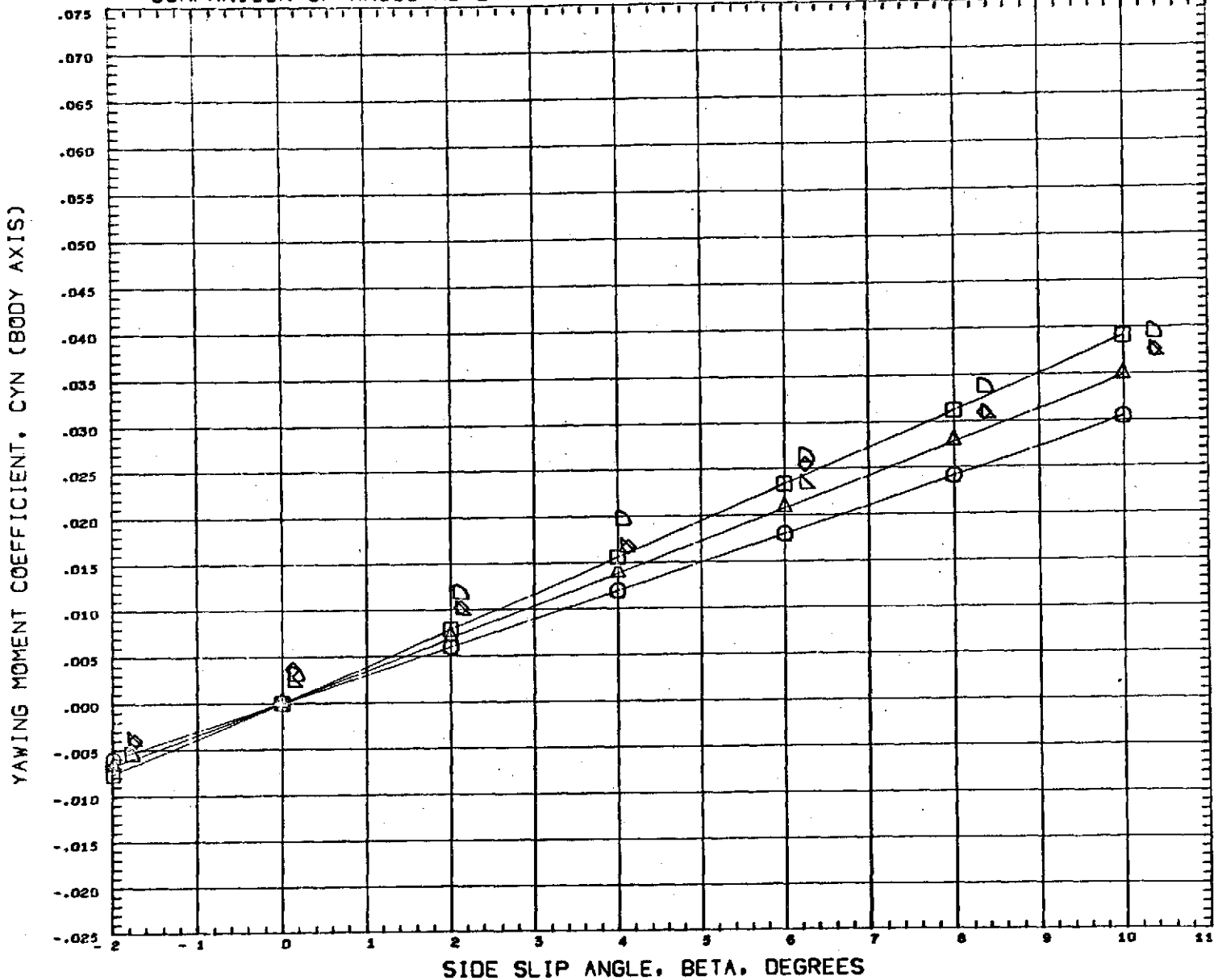


Fig. 11c - Comparison of Theoretical and Experimental Side Force Coefficients for the HB Configuration with the Compression Flap Deflected 40° at the Angles of Attack of 40°, 45° and 50°



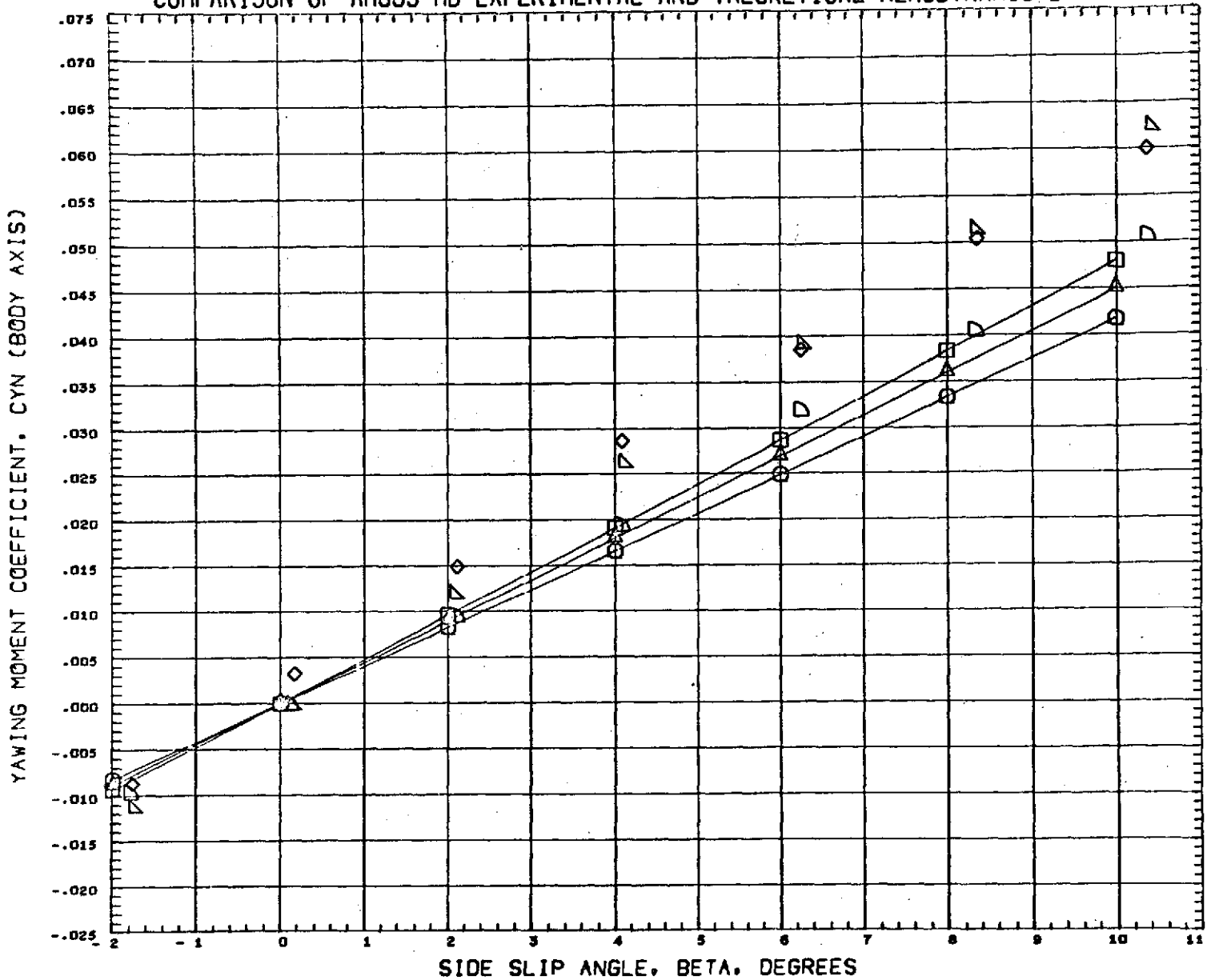
COMPARISON OF AMOOS HB EXPERIMENTAL AND THEORETICAL AERODYNAMIC DATA



DATA SET SYMBOL	CONFIGURATION DESCRIPTION	ALPHA	ELVATR	
(A00030)	AMOOS HB CONFIG FORWARD FLAP ARC TEST	40.000	0.000	SEE THE ASSOCIATED DATA DOCUMENT FOR REFERENCE CHARACTERISTICS
(A00027)	AMOOS HB CONFIG FORWARD FLAP ARC TEST	45.000	0.000	
(A00023)	AMOOS HB CONFIG FORWARD FLAP ARC TEST	50.000	0.000	
(AMZ09)	AMOOS CONFIGURATION HB DEL ELE=0	40.000	0.000	
(AMZ13)	AMOOS CONFIGURATION HB DEL ELE=0	45.000	0.000	
(AMZ17)	AMOOS CONFIGURATION HB DEL ELE=0	50.000	0.000	
MACH	10.270 26.800			

Fig. 11d - Comparison of Theoretical and Experimental Yawing Moment Coefficients for the HB Configuration with the Compression Flap Deflected 0° at the Angles of Attack of 40°, 45° and 50°

COMPARISON OF AMOOS HB EXPERIMENTAL AND THEORETICAL AERODYNAMIC DATA



DATA SET SYMBOL	CONFIGURATION DESCRIPTION	ALPHA	ELVATR	
(A00031)	AMOOS HB CONFIG FORWARD FLAP ARC TEST	40.000	40.000	SEE THE ASSOCIATED DATA DOCUMENT FOR REFERENCE CHARACTERISTICS
(A00026)	AMOOS HB CONFIG FORWARD FLAP ARC TEST	45.000	40.000	
(A00024)	AMOOS HB CONFIG FORWARD FLAP ARC TEST	50.000	40.000	
(ANYZ12)	AMOOS CONFIGURATION HB DEL ELE=40	40.000	40.000	
(ANYZ16)	AMOOS CONFIGURATION HB DEL ELE=40	45.000	40.000	
(ANYZ20)	AMOOS CONFIGURATION HB DEL ELE=40	50.000	40.000	
MACH	10.270 26.800			

Fig. 11e - Comparison of Theoretical and Experimental Yawing Moment Coefficients for the HB Configuration with the Compression Flap Deflected 40° at the Angles of Attack of 40°, 45° and 50°

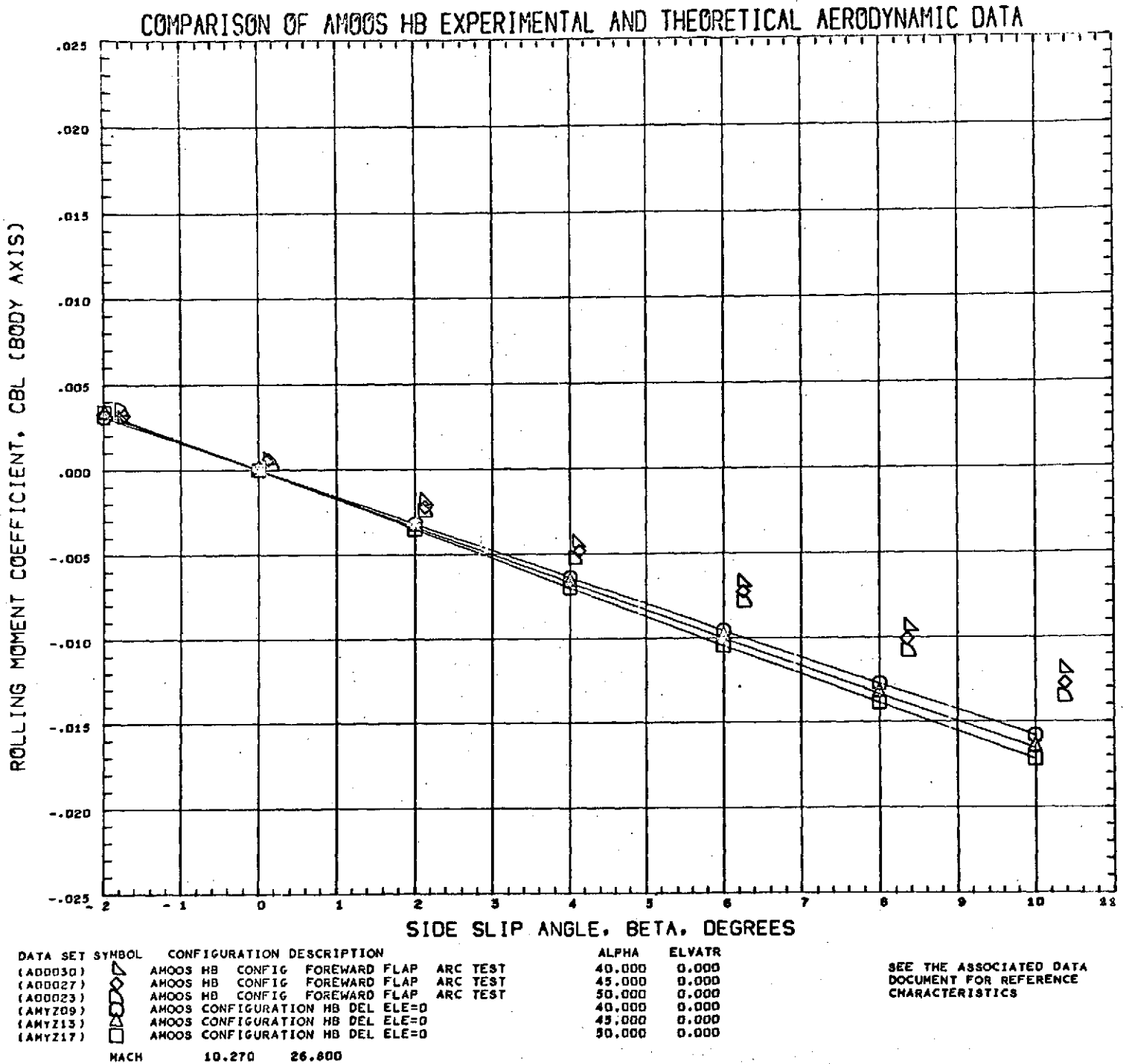
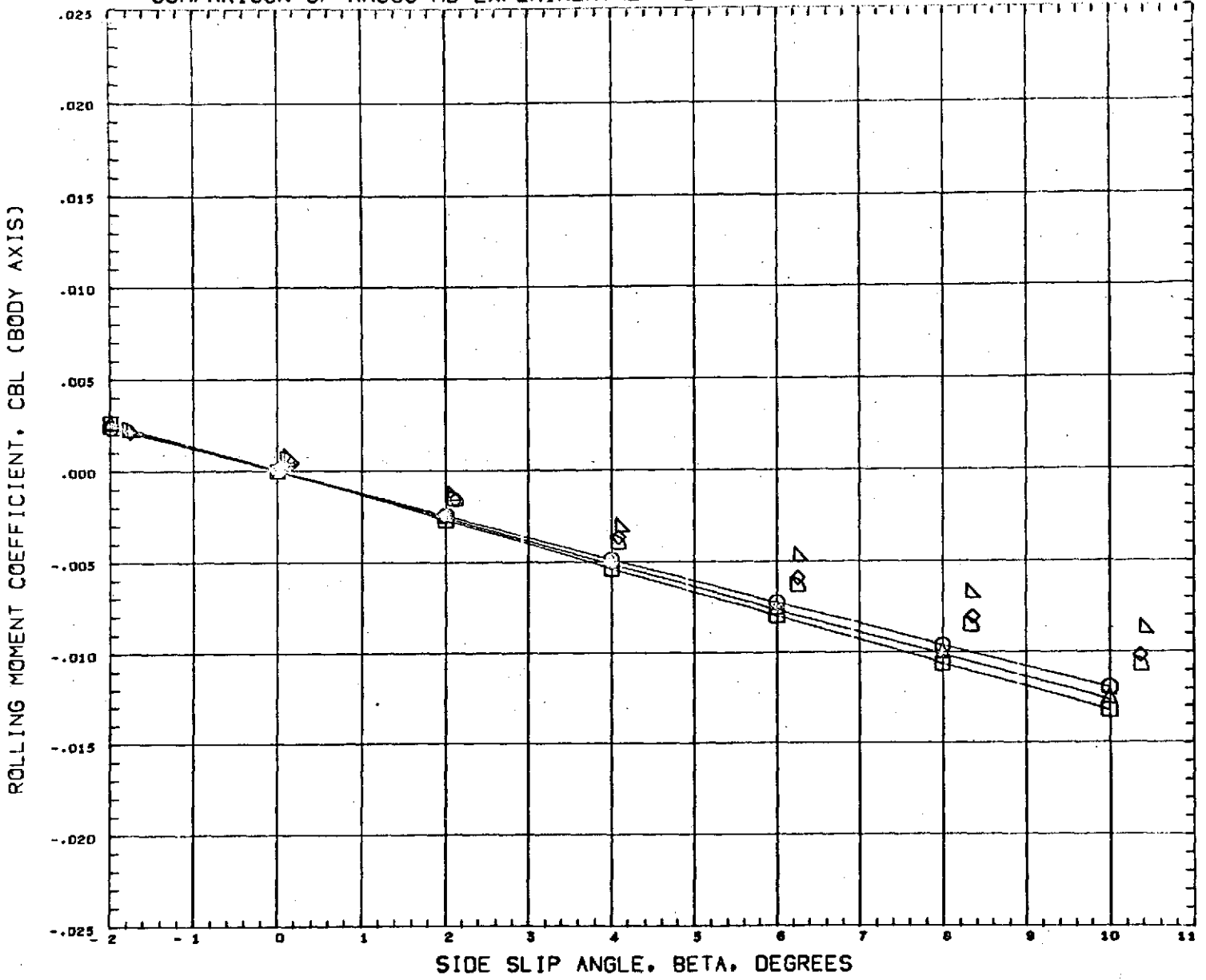


Fig. 11f - Comparison of Theoretical and Experimental Rolling Moment Coefficients for the HB Configuration with the Compression Flap Deflected 0° at the Angles of Attack of 40°, 45° and 50°

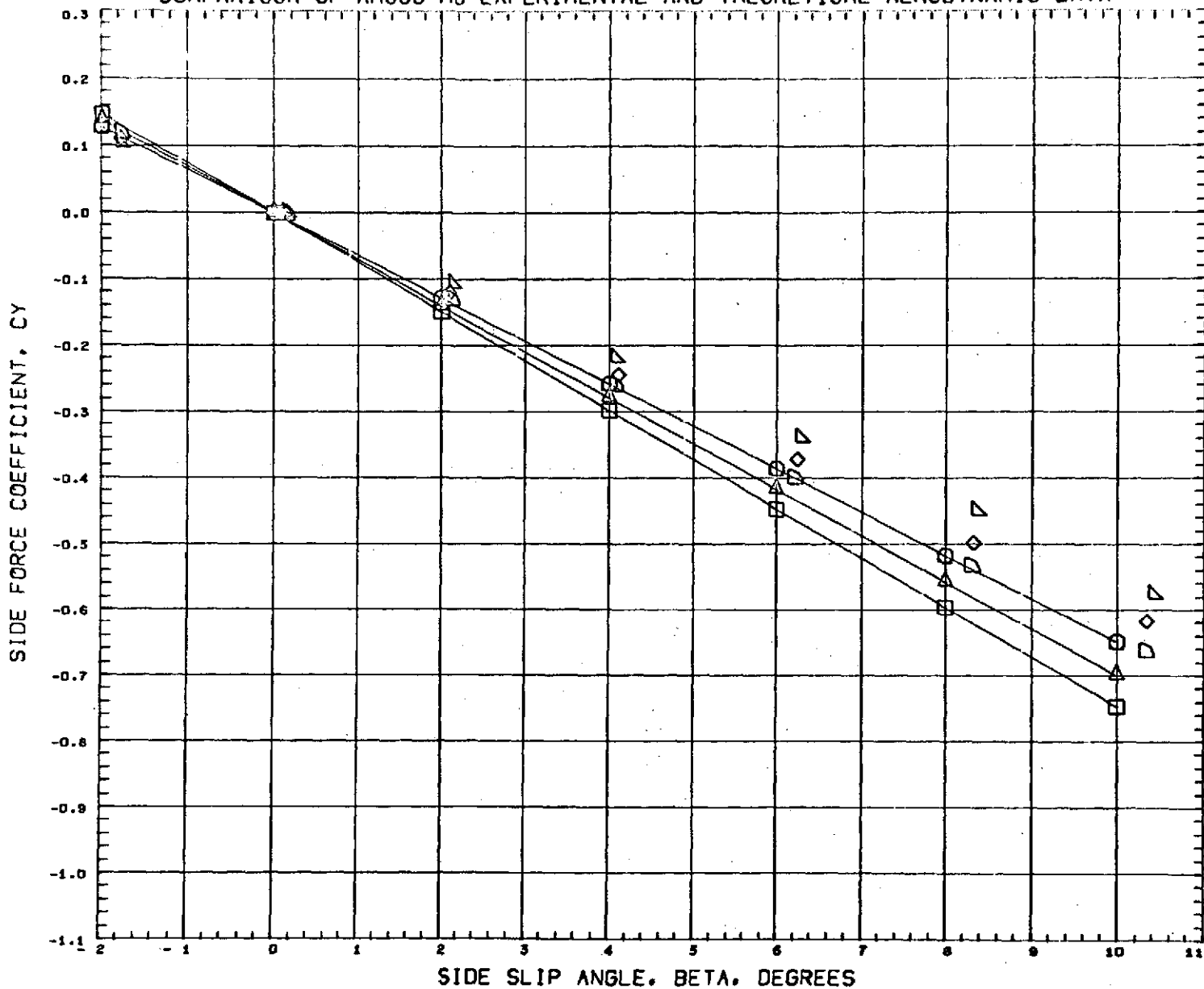
COMPARISON OF AMOOS HB EXPERIMENTAL AND THEORETICAL AERODYNAMIC DATA



DATA SET SYMBOL	CONFIGURATION DESCRIPTION	ALPHA	ELVATR	
(A00031)	AMOOS HB CONFIG FORWARD FLAP ARC TEST	40.000	40.000	SEE THE ASSOCIATED DATA DOCUMENT FOR REFERENCE CHARACTERISTICS
(A00026)	AMOOS HB CONFIG FORWARD FLAP ARC TEST	45.000	40.000	
(A00024)	AMOOS HB CONFIG FORWARD FLAP ARC TEST	50.000	40.000	
(AMY212)	AMOOS CONFIGURATION HB DEL ELE=40	40.000	40.000	
(AMY216)	AMOOS CONFIGURATION HB DEL ELE=40	45.000	40.000	
(AMY220)	AMOOS CONFIGURATION HB DEL ELE=40	50.000	40.000	
MACH	10.270 26.800			

Fig. 11g - Comparison of Theoretical and Experimental Rolling Moment Coefficients for the HB Configuration with the Compression Flap Deflected 40° at the Angles of Attack of 40°, 45° and 50°

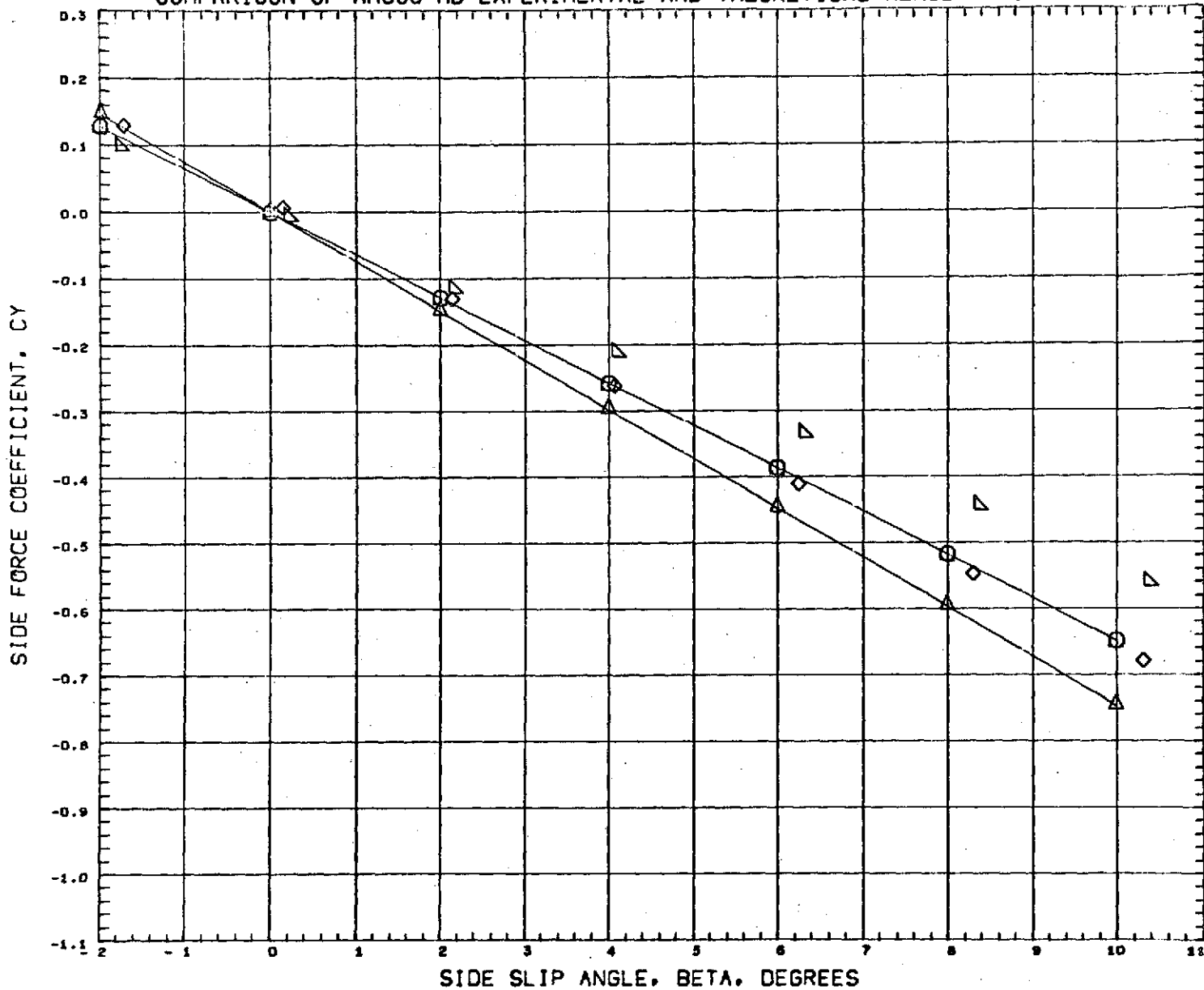
COMPARISON OF AMOOS HB EXPERIMENTAL AND THEORETICAL AERODYNAMIC DATA



DATA SET	SYMBOL	CONFIGURATION DESCRIPTION	ALPHA	ELVATR	
(A00029)	△	AMOOS HB CONFIG AFT FLAP ARC TEST	40.000	0.000	SEE THE ASSOCIATED DATA DOCUMENT FOR REFERENCE CHARACTERISTICS
(A00026)	◇	AMOOS HB CONFIG AFT FLAP ARC TEST	45.000	0.000	
(A00022)	□	AMOOS HB CONFIG AFT FLAP ARC TEST	50.000	0.000	
(AMY249)	○	AMOOS CONFIGURATION HB BAS ROT DEL ELE=0	40.000	0.000	
(AMY253)	○	AMOOS CONFIGURATION HB BAS ROT DEL ELE=0	45.000	0.000	
(AMY257)	○	AMOOS CONFIGURATION HB BAS ROT DEL ELE=0	50.000	0.000	
MACH		10.270 26.800			

Fig. 12a - Comparison of Theoretical and Experimental Side Force Coefficients for the HB Configuration with an Expansion Flap Deflection of 0° at the Angles of Attack of 40°, 45° and 50°

COMPARISON OF AMOOS HB EXPERIMENTAL AND THEORETICAL AERODYNAMIC DATA



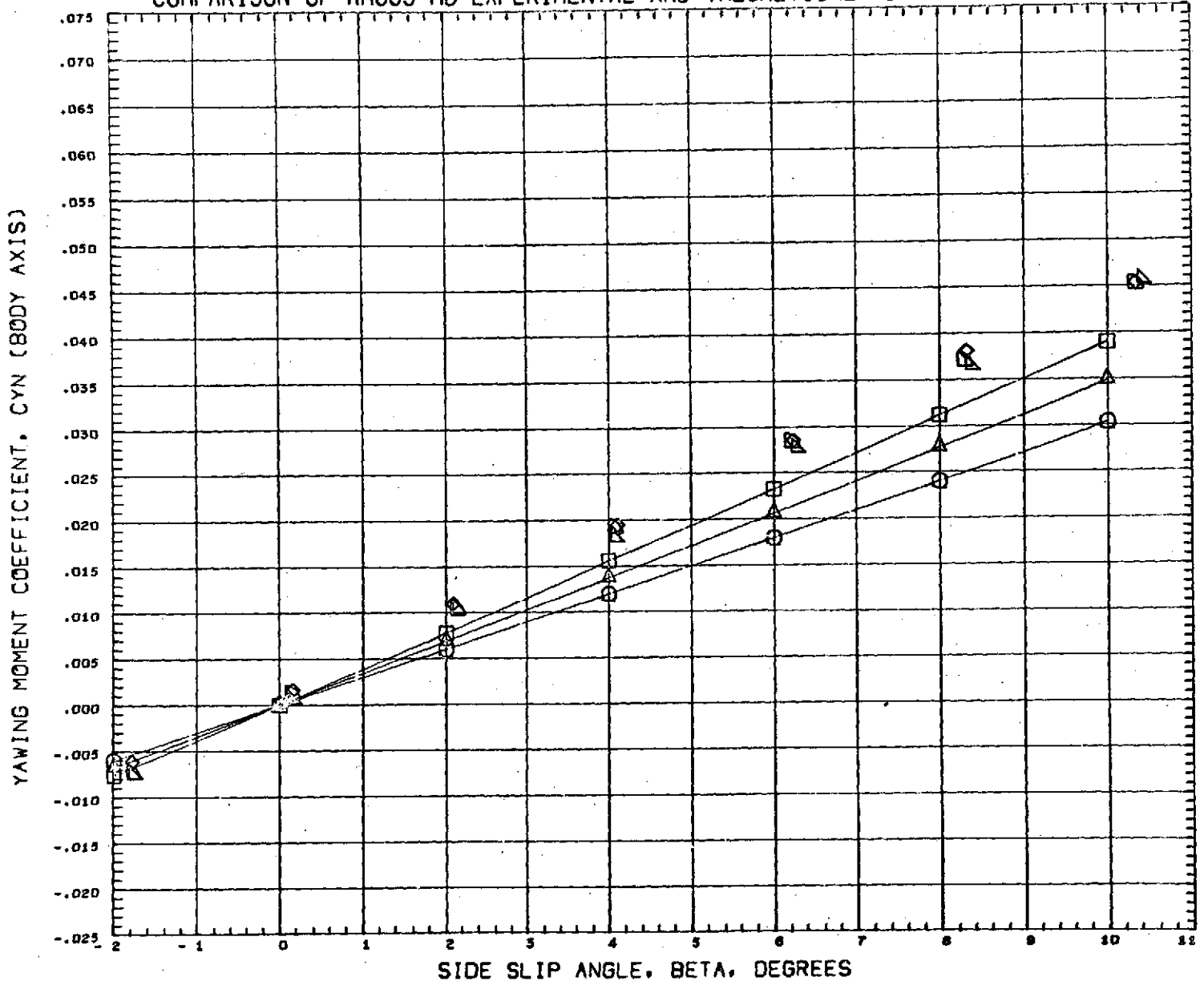
DATA SET SYMBOL	CONFIGURATION DESCRIPTION	ALPHA	ELVATR
(A00032)	AMOOS HB CONFIG AFT FLAP ARC TEST	40.000	-40.000
(A00021)	AMOOS HB CONFIG AFT FLAP ARC TEST	51.000	-40.000
(A00025)	AMOOS CONFIGURATION HB BAS ROT DEL ELE=-40	40.000	-40.000
(A00026)	AMOOS CONFIGURATION HB BAS ROT DEL ELE=-40	50.000	-40.000

SEE THE ASSOCIATED DATA DOCUMENT FOR REFERENCE CHARACTERISTICS

MACH 10.270 26.800

Fig. 12b - Comparison of Theoretical and Experimental Side Force Coefficients for the HB Configuration with an Expansion Flap Deflection of  $-40^\circ$  at the Angles of Attack of  $40^\circ$  and  $50^\circ$

COMPARISON OF AMOOS HB EXPERIMENTAL AND THEORETICAL AERODYNAMIC DATA

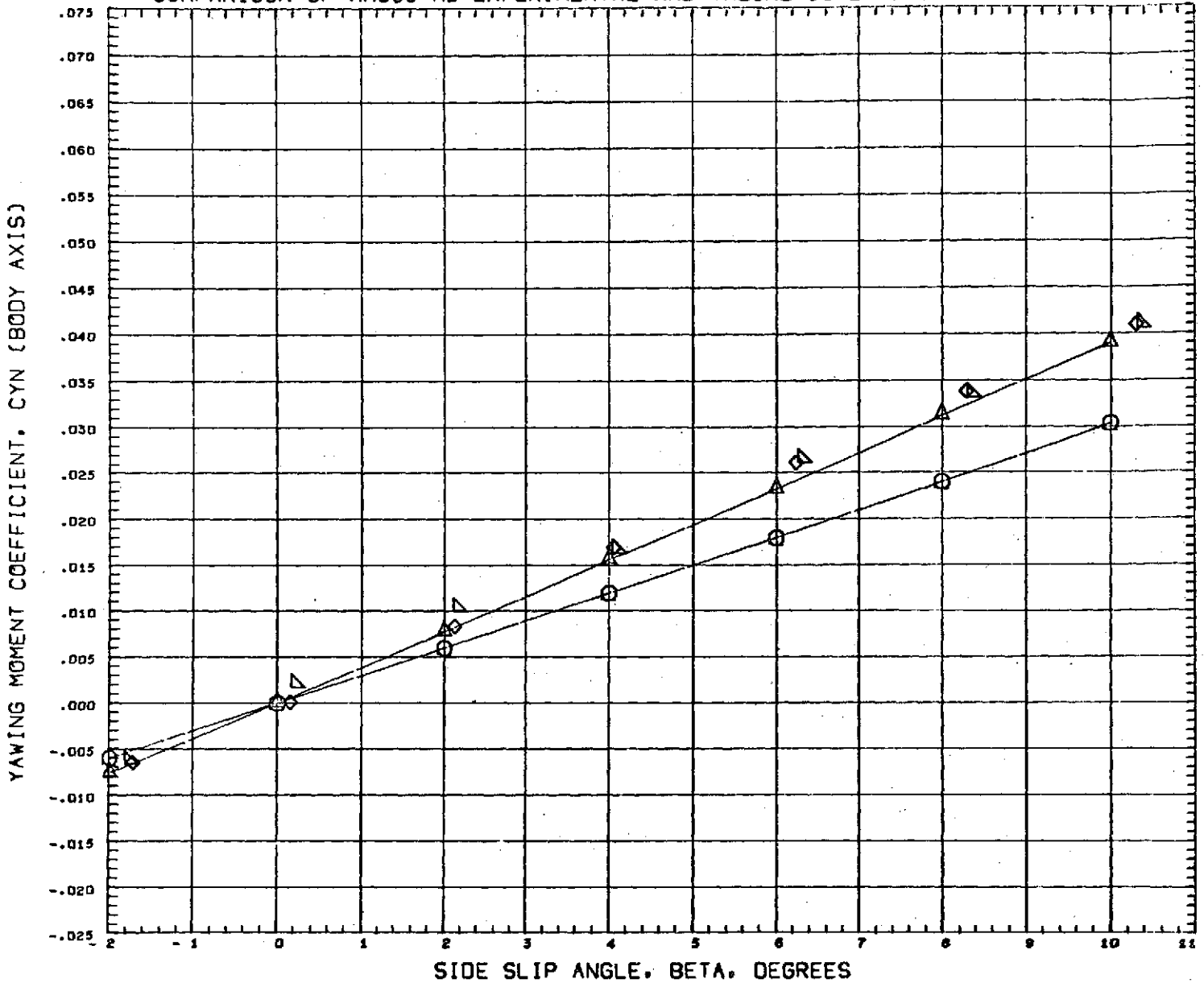


DATA SET SYMBOL	CONFIGURATION DESCRIPTION	ALPHA	ELVATR	
(A00029)	AMOOS HB CONFIG AFT FLAP ARC TEST	40.000	0.000	SEE THE ASSOCIATED DATA DOCUMENT FOR REFERENCE CHARACTERISTICS
(A00028)	AMOOS HB CONFIG AFT FLAP ARC TEST	45.000	0.000	
(A00022)	AMOOS HB CONFIG AFT FLAP ARC TEST	50.000	0.000	
(AMY249)	AMOOS CONFIGURATION HB BAS ROT DEL ELE=0	40.000	0.000	
(AMY253)	AMOOS CONFIGURATION HB BAS ROT DEL ELE=0	45.000	0.000	
(AMY257)	AMOOS CONFIGURATION HB BAS ROT DEL ELE=0	50.000	0.000	
MACH 10.270 26.800				

Fig. 12c - Comparison of Theoretical and Experimental Yawing Moment Coefficients for the HB Configuration with an Expansion Flap Deflection of 0° at the Angles of Attack of 40°, 45° and 50°



COMPARISON OF AMOOS HB EXPERIMENTAL AND THEORETICAL AERODYNAMIC DATA



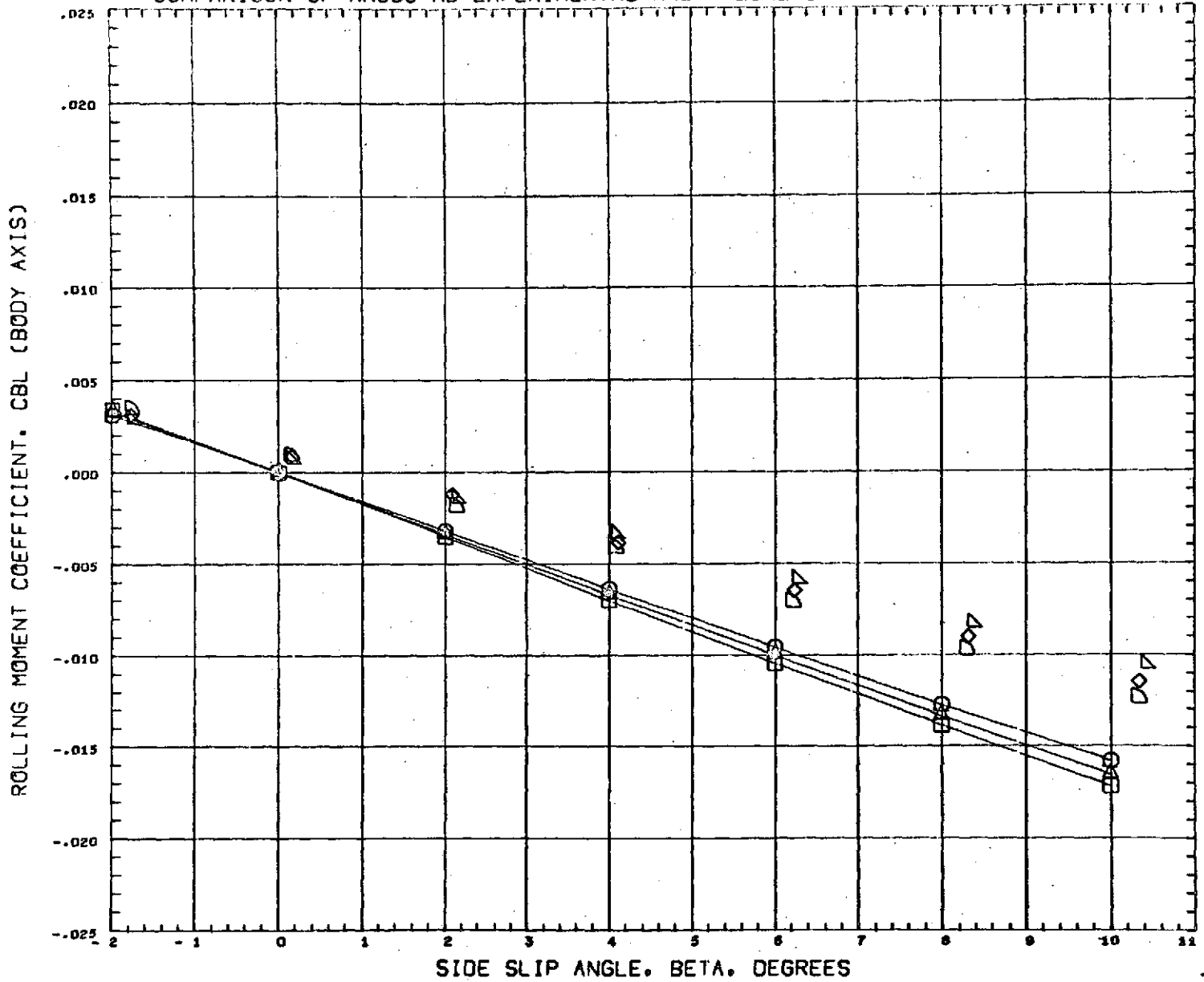
DATA SET SYMBOL	CONFIGURATION DESCRIPTION	ALPHA	ELVATR
(A00032)	AMOOS HB CONFIG AFT FLAP ARC TEST	40.000	-40.000
(A00021)	AMOOS HB CONFIG AFT FLAP ARC TEST	51.000	-40.000
(AMY252)	AMOOS CONFIGURATION HB BAS ROT DEL ELE=-40	40.000	-40.000
(AMY260)	AMOOS CONFIGURATION HB BAS ROT DEL ELE=-40	50.000	-40.000

SEE THE ASSOCIATED DATA DOCUMENT FOR REFERENCE CHARACTERISTICS

MACH 10.270 26.800

Fig. 12d - Comparison of Theoretical and Experimental Yawing Moment Coefficients for the HB Configuration with an Expansion Flap Deflection of  $-40^\circ$  at the Angles of Attack of  $40^\circ$  and  $50^\circ$

COMPARISON OF AMOOS HB EXPERIMENTAL AND THEORETICAL AERODYNAMIC DATA



DATA SET SYMBOL	CONFIGURATION DESCRIPTION	ALPHA	ELVATR
(A00029)	AMOOS HB CONFIG AFT FLAP ARC TEST	40.000	0.000
(A00028)	AMOOS HB CONFIG AFT FLAP ARC TEST	45.000	0.000
(A00022)	AMOOS HB CONFIG AFT FLAP ARC TEST	50.000	0.000
(AMZ49)	AMOOS CONFIGURATION HB BAS ROT DEL ELE=0	40.000	0.000
(AMZ53)	AMOOS CONFIGURATION HB BAS ROT DEL ELE=0	45.000	0.000
(AMZ57)	AMOOS CONFIGURATION HB BAS ROT DEL ELE=0	50.000	0.000

MACH 10.270 26.800

SEE THE ASSOCIATED DATA DOCUMENT FOR REFERENCE CHARACTERISTICS

Fig. 12e - Comparison of Theoretical and Experimental Rolling Moment Coefficients for the HB Configuration with an Expansion Flap Deflection of 0° at the Angles of Attack of 40°, 45° and 50°

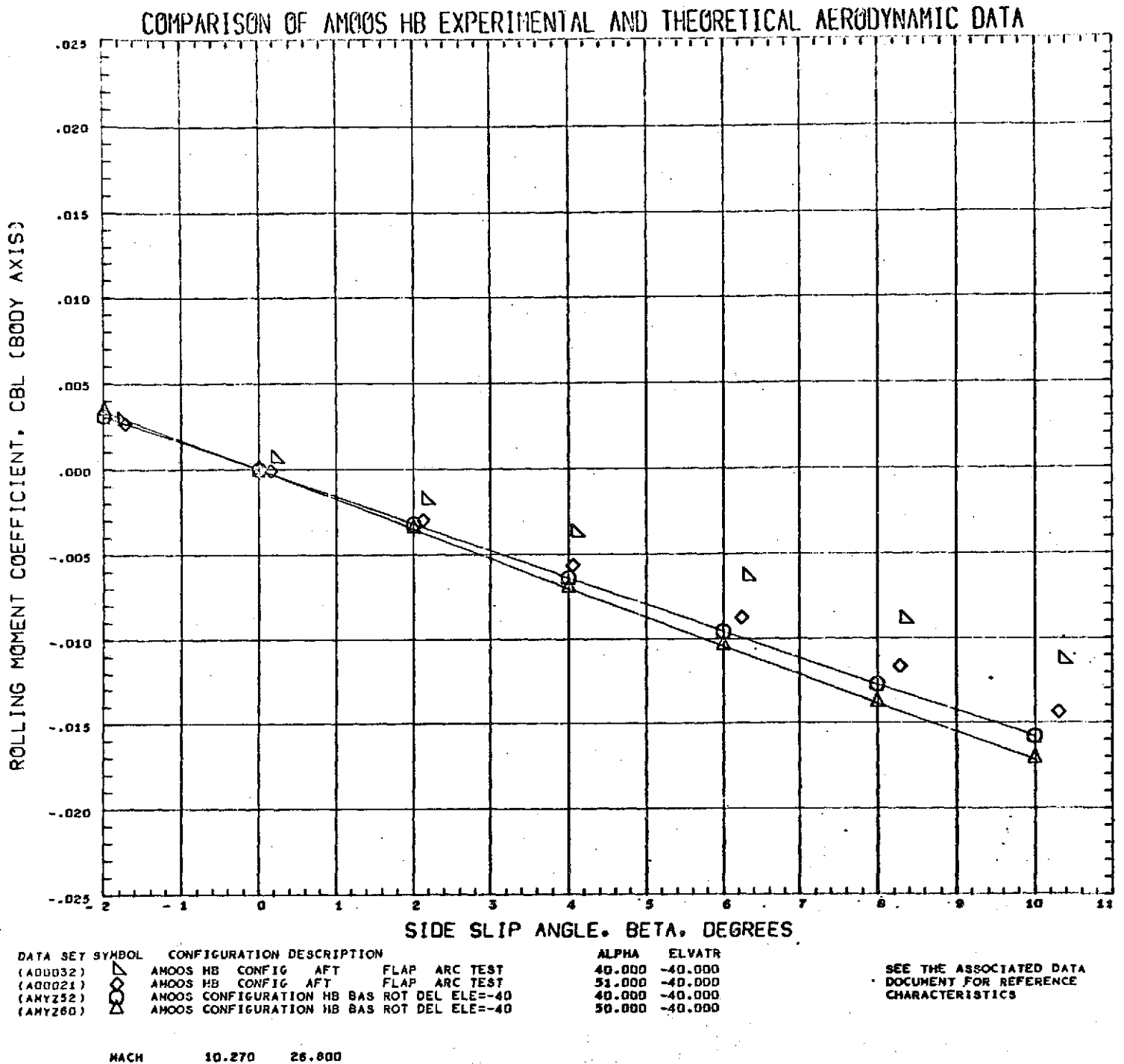
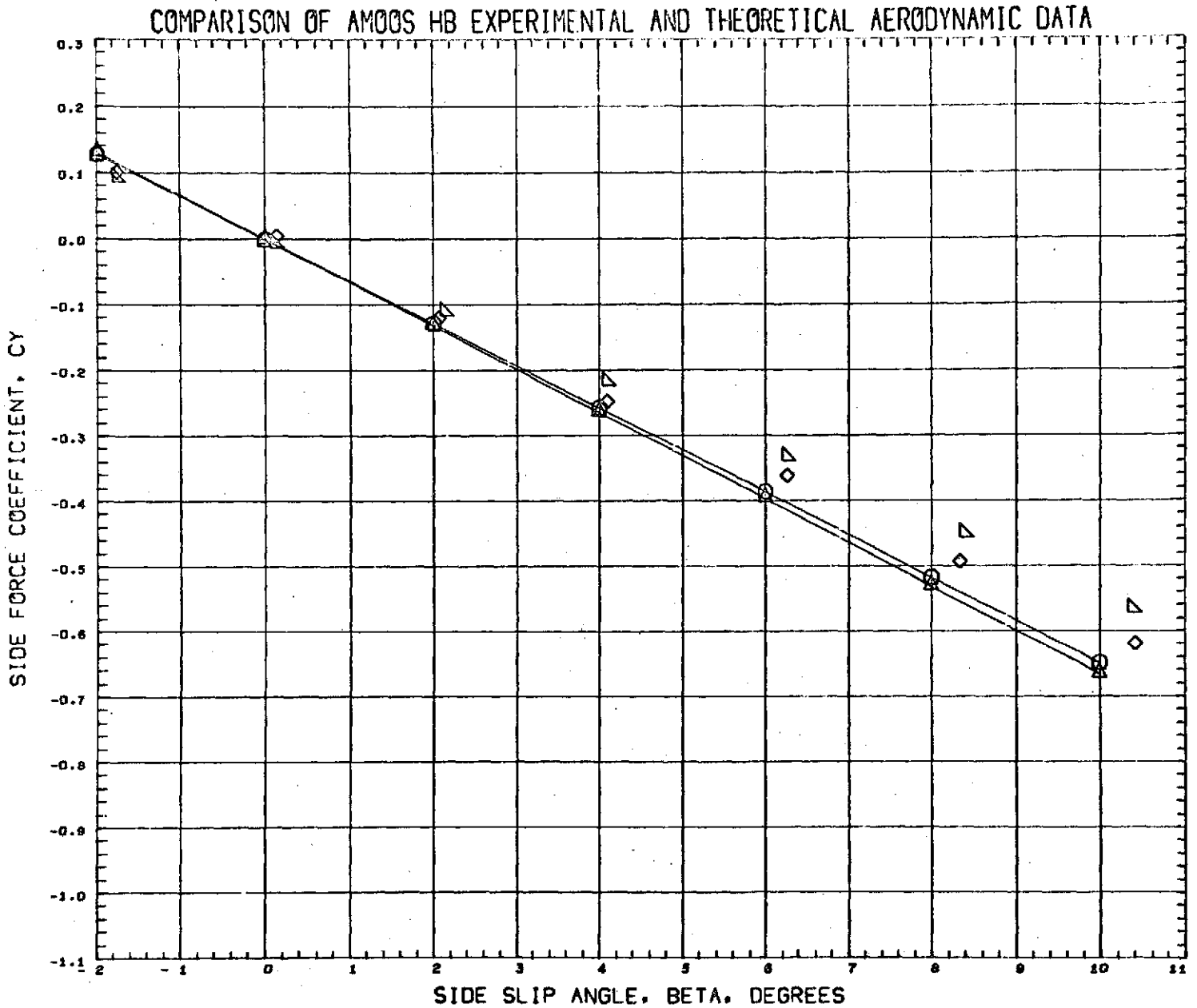


Fig. 12f - Comparison of Theoretical and Experimental Rolling Moment Coefficients for the HB Configuration with an Expansion Flap Deflection of  $-40^\circ$  at the Angles of Attack of  $40^\circ$  and  $50^\circ$



DATA SET SYMBOL	CONFIGURATION DESCRIPTION	ALPHA	ELVATR
(A00030)	ANOOS HB CONFIG FORWARD FLAP ARC TEST	40.000	0.000
(A00031)	ANOOS HB CONFIG FORWARD FLAP ARC TEST	40.000	40.000
(AMY209)	ANOOS CONFIGURATION HB DEL ELE=0	40.000	0.000
(AMY212)	ANOOS CONFIGURATION HB DEL ELE=40	40.000	40.000

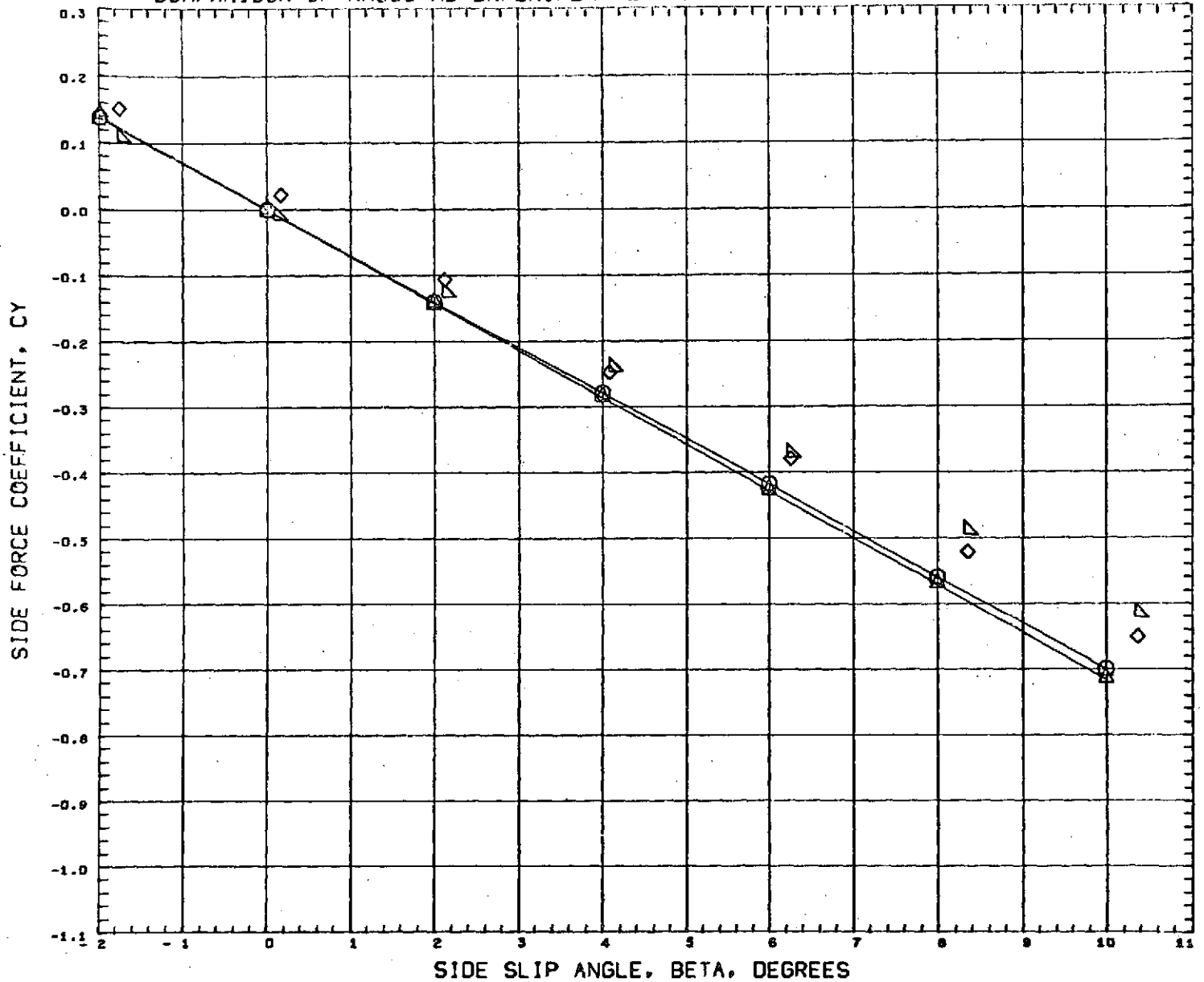
SEE THE ASSOCIATED DATA DOCUMENT FOR REFERENCE CHARACTERISTICS

MACH      10.270      26.800

Fig. 13a - Comparison of Theoretical and Experimental Side Force Coefficients for the HB Configuration with Compression Flap Deflections of 0° and 40° at an Angle of Attack of 40°

C-2

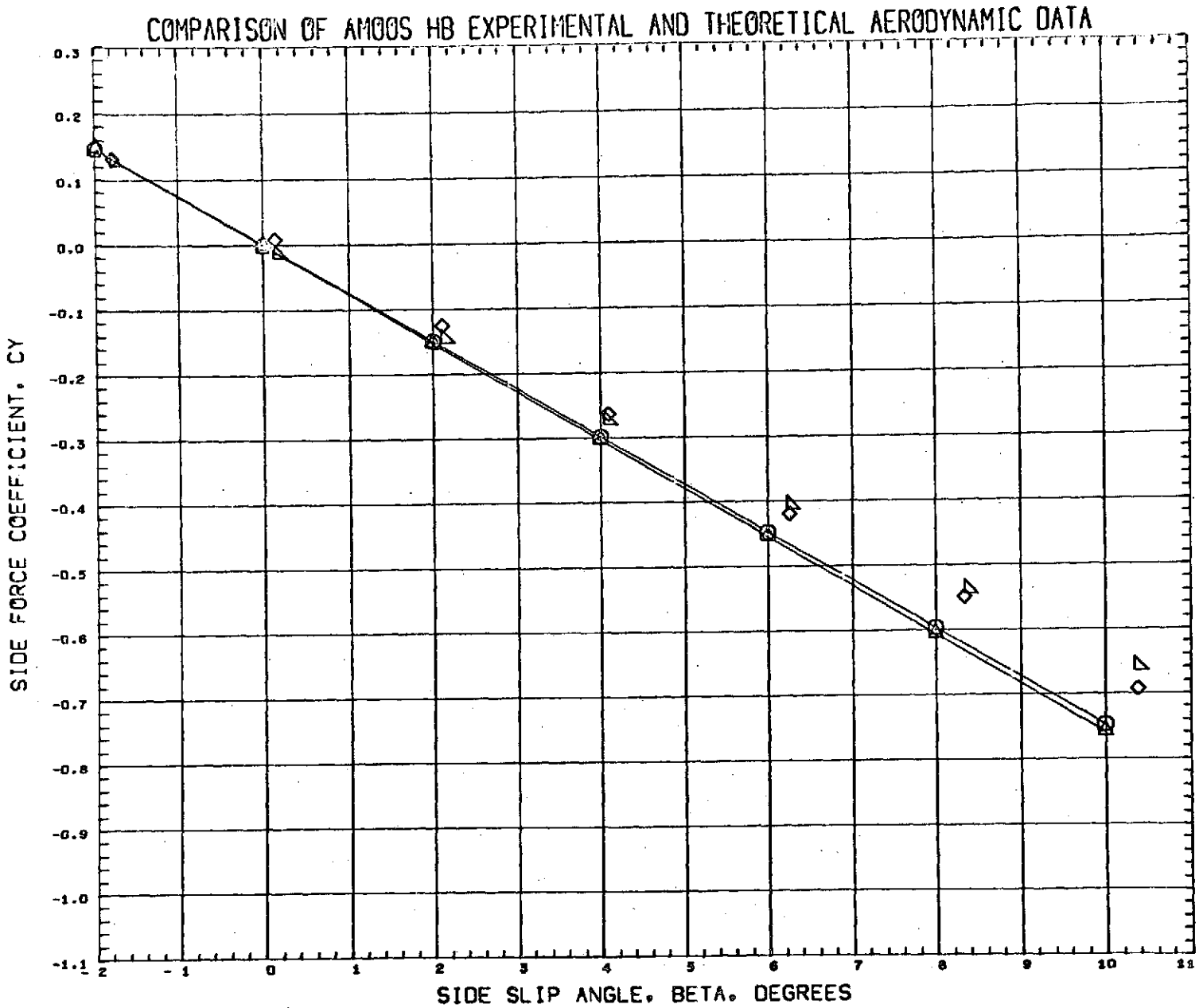
COMPARISON OF AMOOS HB EXPERIMENTAL AND THEORETICAL AERODYNAMIC DATA



DATA SET SYMBOL	CONFIGURATION DESCRIPTION	ALPHA	ELVATR	
(A00027)	AMOOS HB CONFIG FORWARD FLAP ARC TEST	45.000	0.000	SEE THE ASSOCIATED DATA DOCUMENT FOR REFERENCE CHARACTERISTICS
(A00026)	AMOOS HB CONFIG FORWARD FLAP ARC TEST	45.000	40.000	
(AMY213)	AMOOS CONFIGURATION HB DEL ELE=0	45.000	0.000	
(AMY218)	AMOOS CONFIGURATION HB DEL ELE=40	45.000	40.000	

MACH 10.270 26.800

Fig. 13b - Comparison of Theoretical and Experimental Side Force Coefficients for the HB Configuration with Compression Flap Deflections of 0° and 40° at an Angle of Attack of 45°

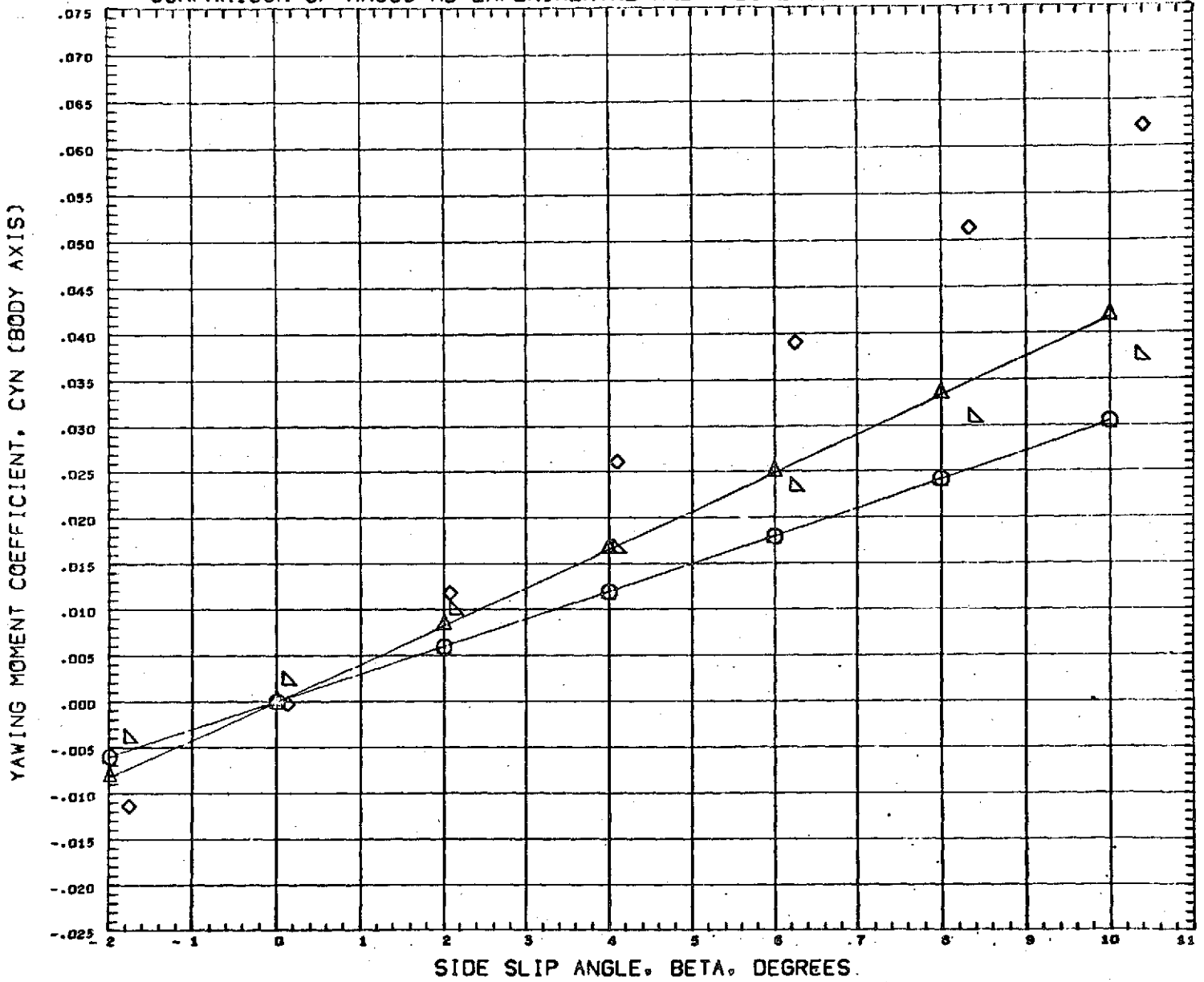


DATA SET	SYMBOL	CONFIGURATION DESCRIPTION	ALPHA	ELVATR	
(A00023)	△	AMOOS HB CONFIG FORWARD FLAP ARC TEST	50.000	0.000	SEE THE ASSOCIATED DATA DOCUMENT FOR REFERENCE CHARACTERISTICS
(A00024)	◇	AMOOS HB CONFIG FORWARD FLAP ARC TEST	50.000	40.000	
(AMYZ17)	○	AMOOS CONFIGURATION HB DEL ELE=0	50.000	0.000	
(AMYZ20)	○	AMOOS CONFIGURATION HB DEL ELE=40	50.000	40.000	

MACH      10.270      26.800

Fig. 13c - Comparison of Theoretical and Experimental Side Force Coefficients for the HB Configuration with Compression Flap Deflections of 0° and 40° at an Angle of Attack of 50°

COMPARISON OF AMOOS HB EXPERIMENTAL AND THEORETICAL AERODYNAMIC DATA

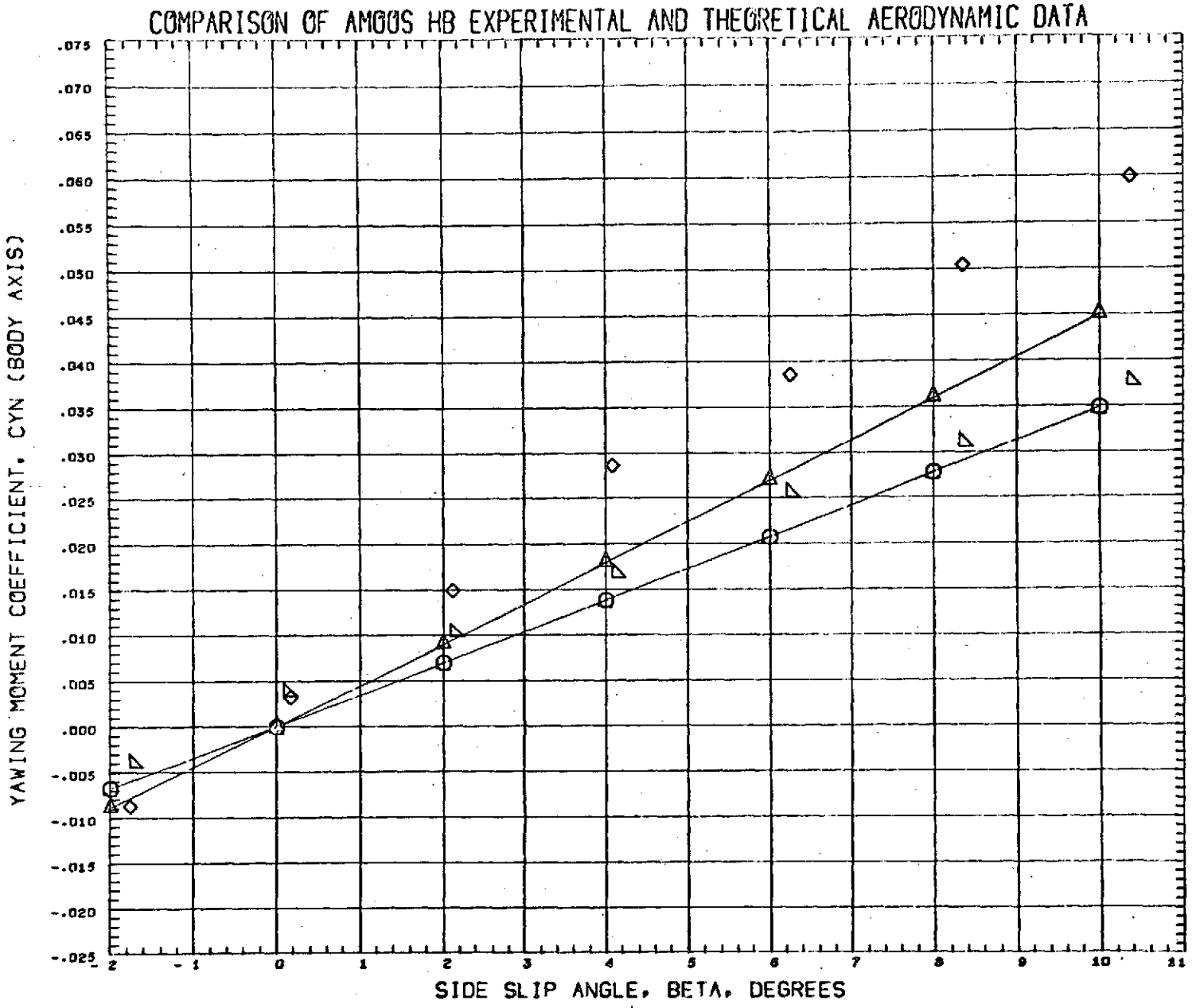


DATA SET SYMBOL	CONFIGURATION DESCRIPTION	ALPHA	ELVATR	
{A00030}	AMOOS HB CONFIG FORWARD FLAP ARC TEST	40.000	0.000	SEE THE ASSOCIATED DATA DOCUMENT FOR REFERENCE CHARACTERISTICS
{A00031}	AMOOS HB CONFIG FORWARD FLAP ARC TEST	40.000	40.000	
{AMY209}	AMOOS CONFIGURATION HB DEL ELE=0	40.000	0.000	
{AMY212}	AMOOS CONFIGURATION HB DEL ELE=40	40.000	40.000	

MACH 10.270 26.800

Fig. 13d - Comparison of Theoretical and Experimental Yawing Moment Coefficients for the HB Configuration with Compression Flap Deflections of 0° and 40° at an Angle of Attack of 40°

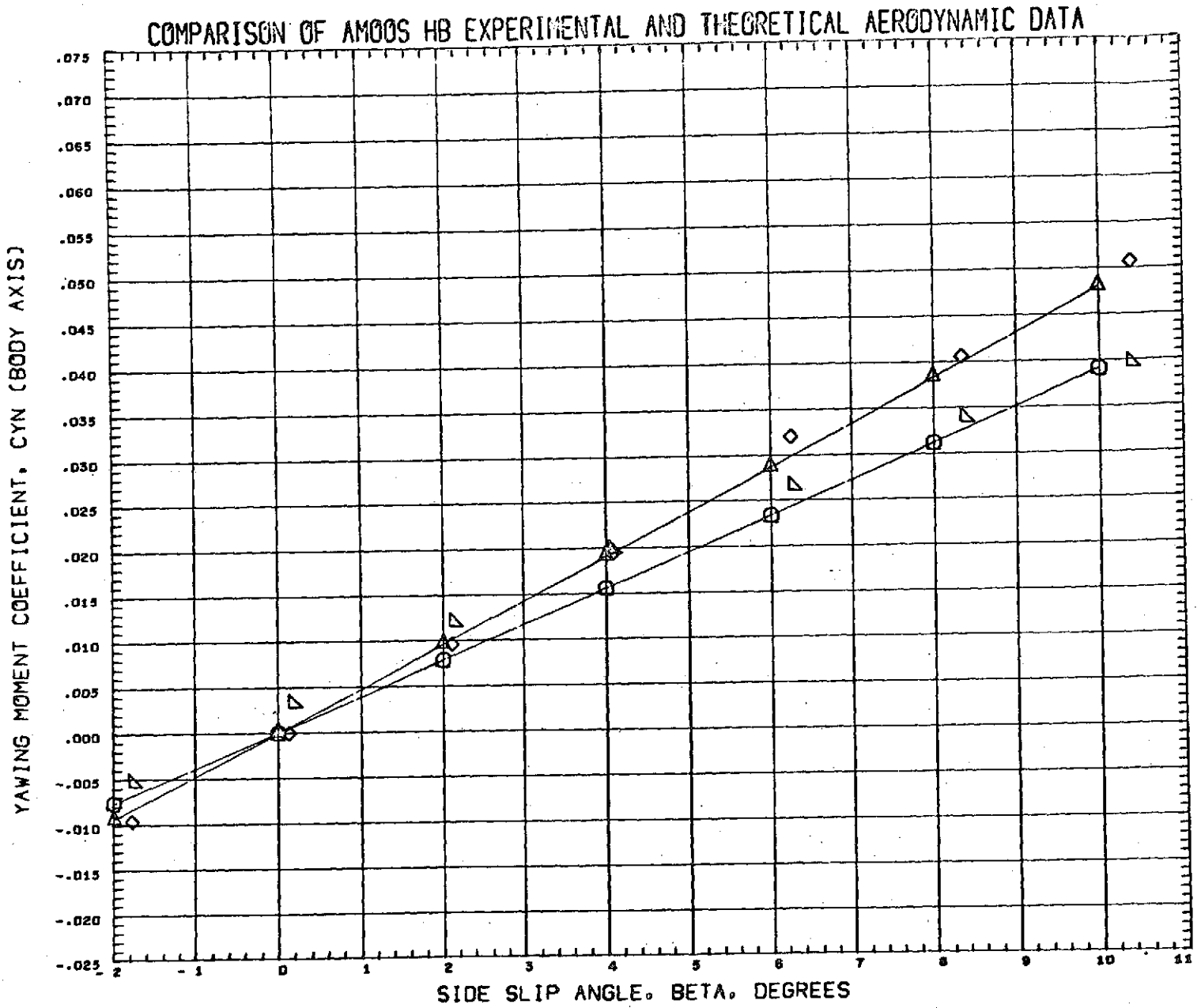




DATA SET SYMBOL	CONFIGURATION DESCRIPTION	ALPHA	ELVATR	
(A00027)	AMOOS HB CONFIG FORWARD FLAP ARC TEST	45.000	0.000	SEE THE ASSOCIATED DATA DOCUMENT FOR REFERENCE CHARACTERISTICS
(A00026)	AMOOS HB CONFIG FORWARD FLAP ARC TEST	45.000	40.000	
(AMY213)	AMOOS CONFIGURATION HB DEL ELE=0	45.000	0.000	
(AMY216)	AMOOS CONFIGURATION HB DEL ELE=40	45.000	40.000	

MACH      10.270      26.800

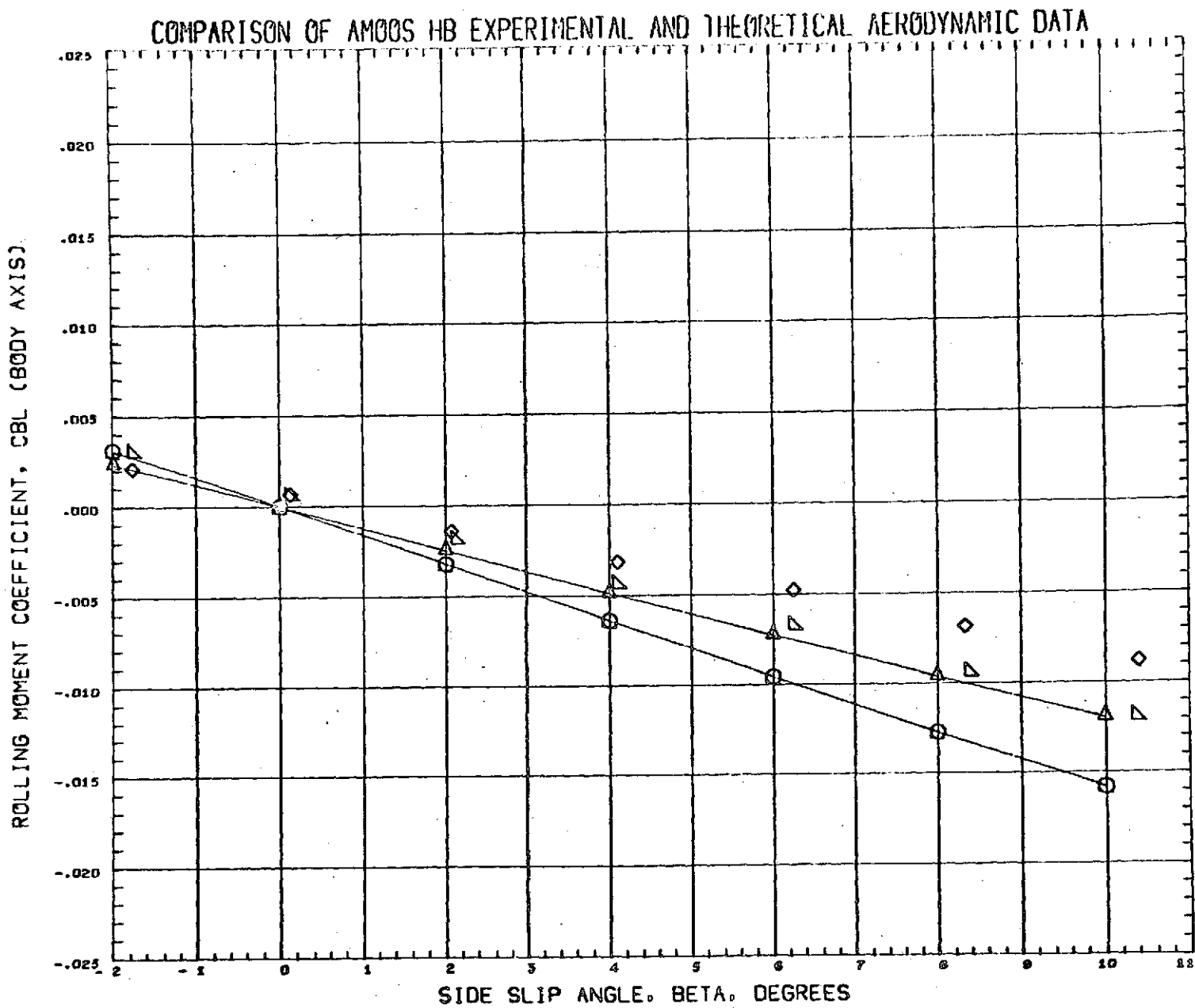
Fig. 13e - Comparison of Theoretical and Experimental Yawing Moment Coefficients for the HB Configuration with Compression Flap Deflections of 0° and 40° at an Angle of Attack of 45°



DATA SET	SYMBOL	CONFIGURATION DESCRIPTION	ALPHA	ELVATR	
(A00023)	△	AMOOS HB CONFIG FORWARD FLAP ARC TEST	50.000	0.000	SEE THE ASSOCIATED DATA DOCUMENT FOR REFERENCE CHARACTERISTICS
(A00024)	○	AMOOS HB CONFIG FORWARD FLAP ARC TEST	50.000	40.000	
(AMY217)	△	AMOOS CONFIGURATION HB DEL ELE=0	50.000	0.000	
(AMY220)	○	AMOOS CONFIGURATION HB DEL ELE=40	50.000	40.000	

MACH      10.270      26.800

Fig. 13f - Comparison of Theoretical and Experimental Yawing Moment Coefficients for the HB Configuration with Compression Flap Deflections of 0° and 40° at an Angle of Attack of 50°

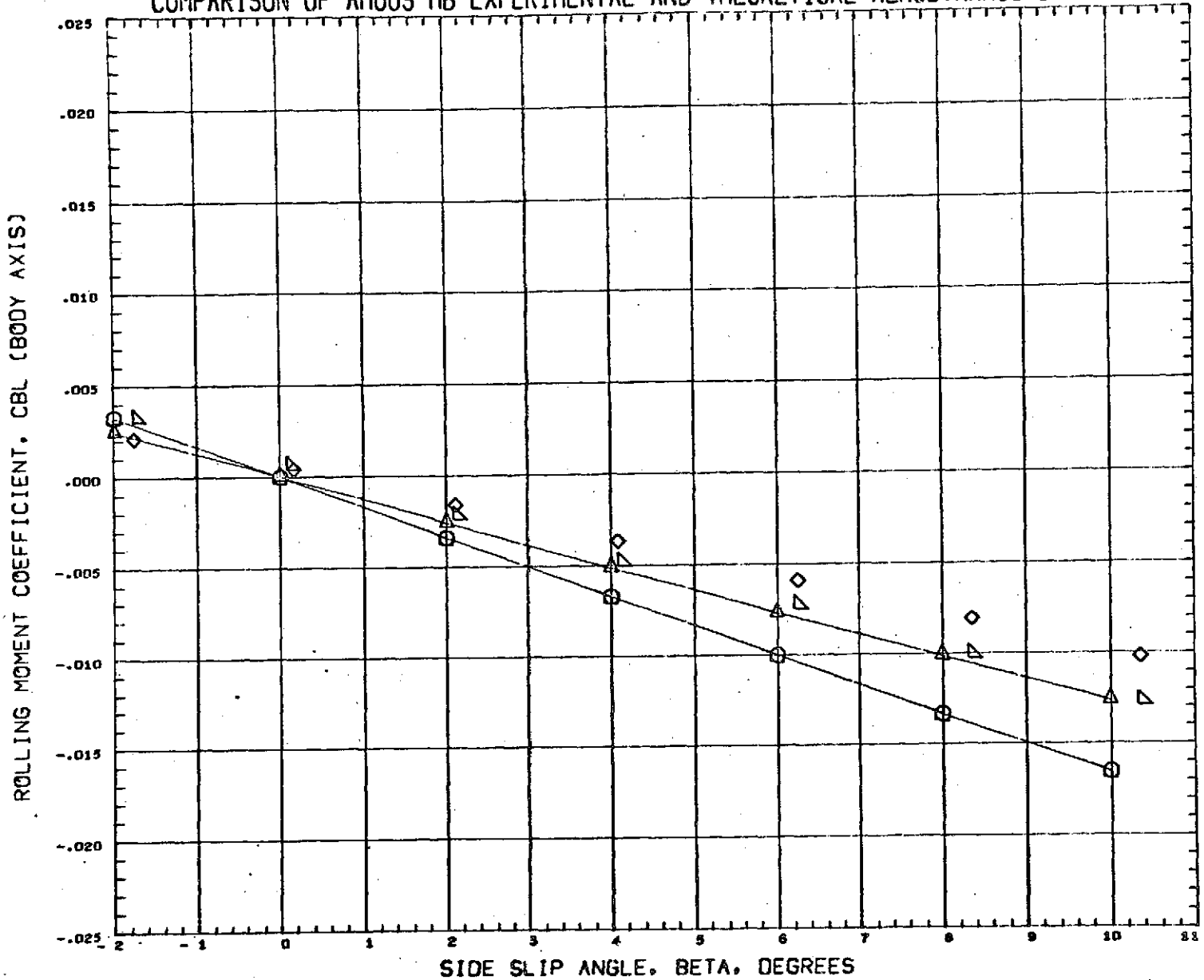


DATA SET SYMBOL	CONFIGURATION DESCRIPTION	ALPHA	ELVATR	
(A00030)	AMOOS HB CONFIG FORWARD FLAP ARC TEST	40.000	0.000	SEE THE ASSOCIATED DATA DOCUMENT FOR REFERENCE CHARACTERISTICS
(A00031)	AMOOS HB CONFIG FORWARD FLAP ARC TEST	40.000	40.000	
(AMYZ09)	AMOOS CONFIGURATION HB DEL ELE=0	40.000	0.000	
(AMYZ12)	AMOOS CONFIGURATION HB DEL ELE=40	40.000	40.000	

MACH      10.270      26.800

Fig. 13g - Comparison of Theoretical and Experimental Rolling Moment Coefficients for the HB Configuration with Compression Flap Deflections of 0° and 40° at an Angle of Attack of 40°

COMPARISON OF AMOOS HB EXPERIMENTAL AND THEORETICAL AERODYNAMIC DATA

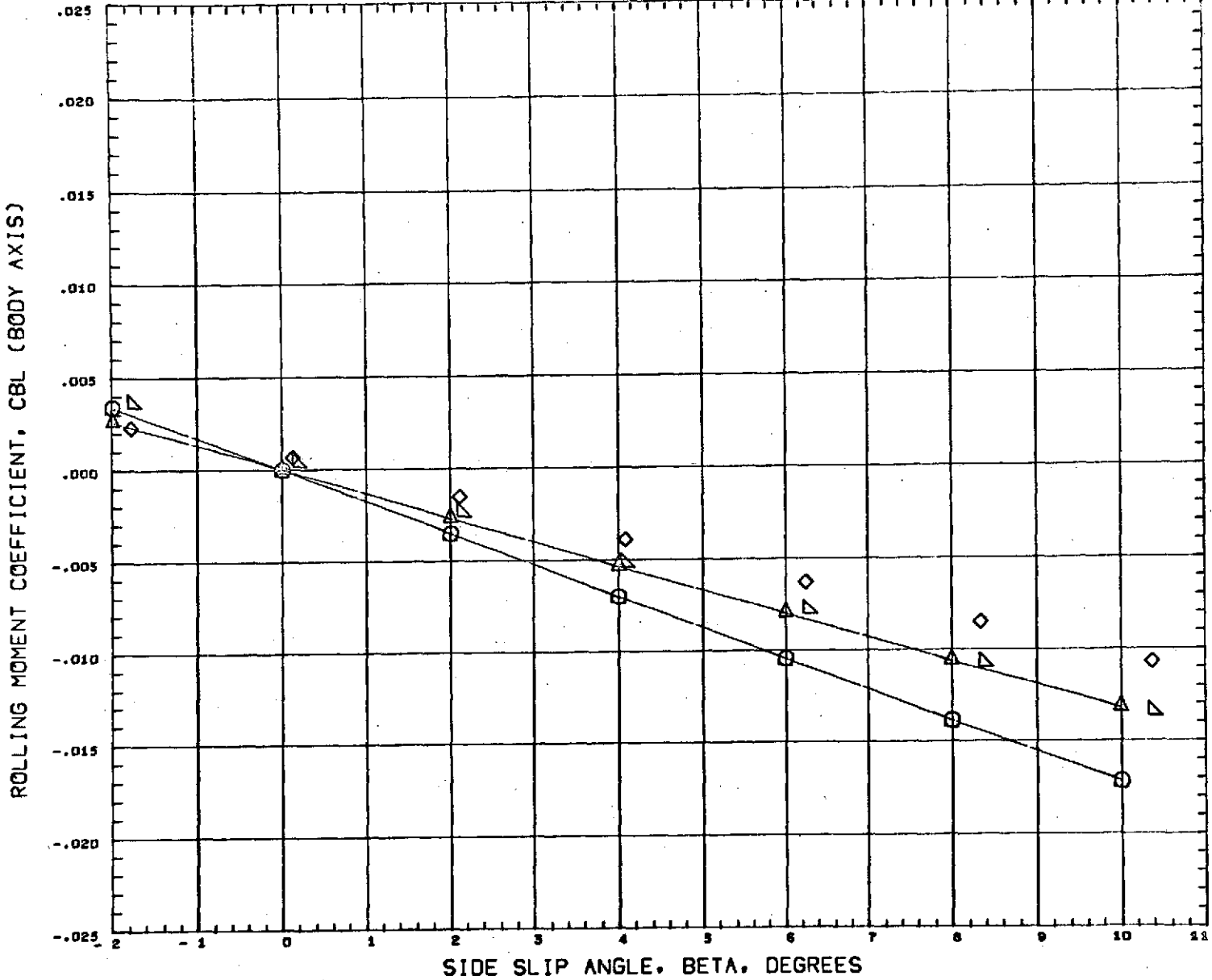


DATA SET SYMBOL	CONFIGURATION DESCRIPTION	ALPHA	ELVATR	
(A00027)	AMOOS HB CONFIG FORWARD FLAP ARC TEST	45.000	0.000	SEE THE ASSOCIATED DATA DOCUMENT FOR REFERENCE CHARACTERISTICS
(A00026)	AMOOS HB CONFIG FORWARD FLAP ARC TEST	45.000	40.000	
(AMYZ13)	AMOOS CONFIGURATION HB DEL ELE=0	45.000	0.000	
(AMYZ16)	AMOOS CONFIGURATION HB DEL ELE=40	45.000	40.000	

MACH 10.270 26.800

Fig. 13h - Comparison of Theoretical and Experimental Rolling Moment Coefficients for the HB Configuration with Compression Flap Deflections of 0° and 40° at an Angle of Attack of 45°

COMPARISON OF AMOOS HB EXPERIMENTAL AND THEORETICAL AERODYNAMIC DATA

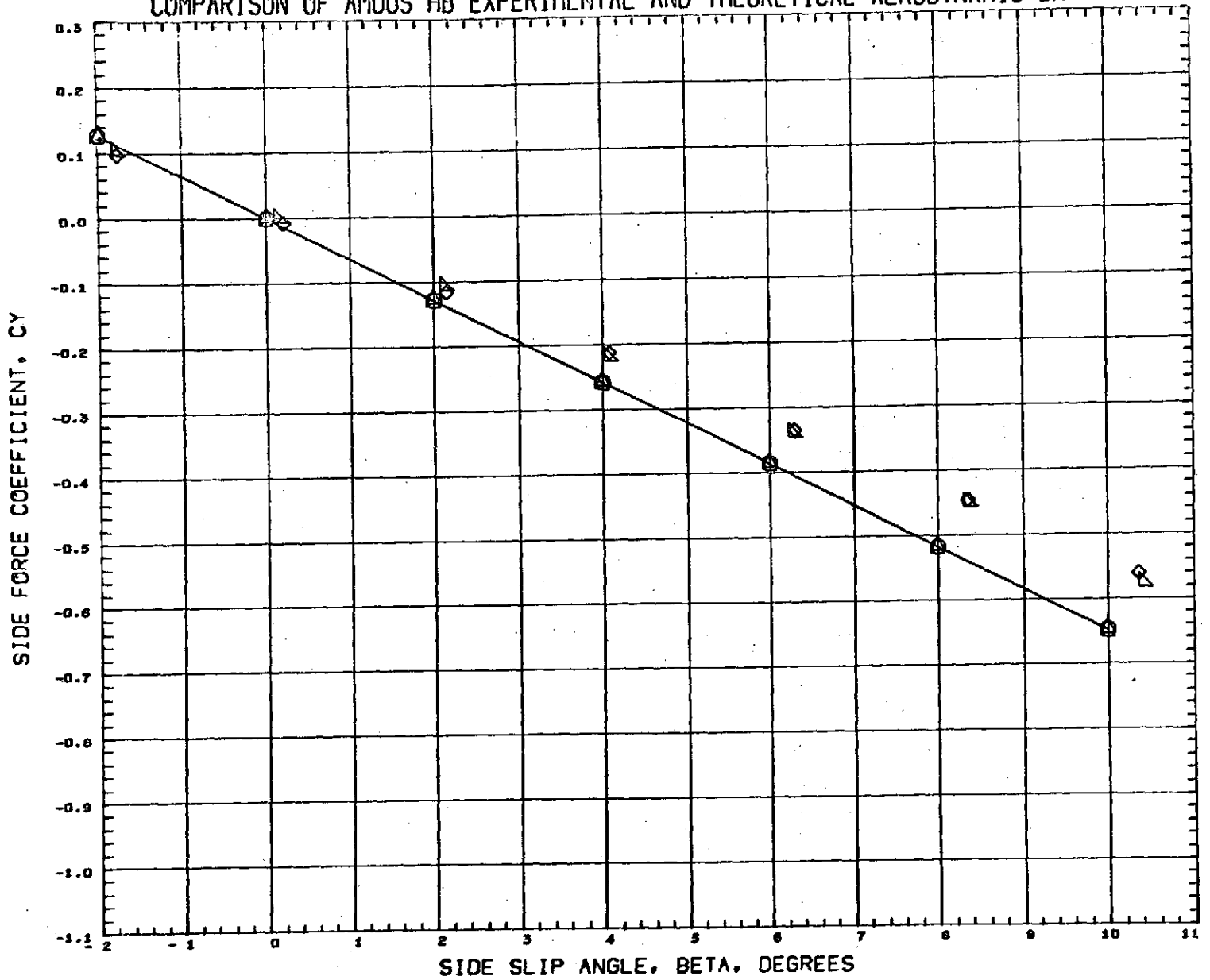


DATA SET SYMBOL	CONFIGURATION DESCRIPTION	ALPHA	ELVATR	
(A00023)	AMOOS HB CONFIG FORWARD FLAP ARC TEST	50.000	0.000	SEE THE ASSOCIATED DATA DOCUMENT FOR REFERENCE CHARACTERISTICS
(A00024)	AMOOS HB CONFIG FORWARD FLAP ARC TEST	50.000	40.000	
(AMZ17)	AMOOS CONFIGURATION HB DEL ELE=0	50.000	0.000	
(AMZ20)	AMOOS CONFIGURATION HB DEL ELE=40	50.000	40.000	

MACH 10.270 26.800

Fig. 13i - Comparison of Theoretical and Experimental Rolling Moment Coefficients for the HB Configuration with Compression Flap Deflections of 0° and 40° at an Angle of Attack of 50°

COMPARISON OF AMOOS HB EXPERIMENTAL AND THEORETICAL AERODYNAMIC DATA

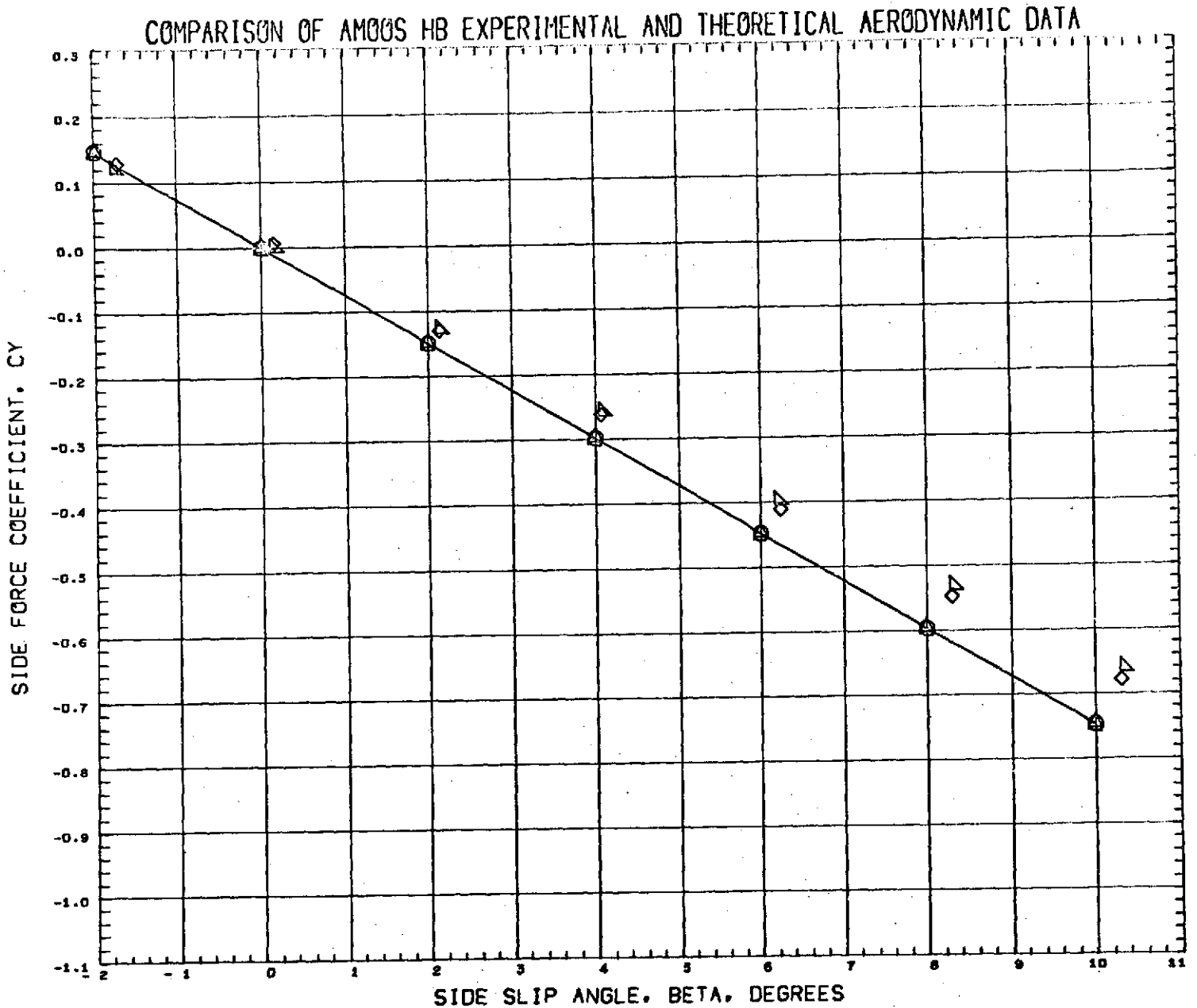


DATA SET SYMBOL	CONFIGURATION DESCRIPTION	ALPHA	ELVATR
(A00029)	AMOOS HB CONFIG AFT FLAP ARC TEST	40.000	0.000
(A00032)	AMOOS HB CONFIG AFT FLAP ARC TEST	40.000	-40.000
(AMY249)	AMOOS CONFIGURATION HB BAS ROT DEL ELE=0	40.000	0.000
(AMY252)	AMOOS CONFIGURATION HB BAS ROT DEL ELE=-40	40.000	-40.000

SEE THE ASSOCIATED DATA DOCUMENT FOR REFERENCE CHARACTERISTICS

MACH 10.270 28.800

Fig. 13j - Comparison of Theoretical and Experimental Side Force Coefficients for the HB Configuration with Expansion Flap Deflections of 0° and -40° at an Angle of Attack of 40°



DATA SET SYMBOL	CONFIGURATION DESCRIPTION	ALPHA	ELVATR
{A00022}	AMOOS HB CONFIG AFT FLAP ARC TEST	50.000	0.000
{A00021}	AMOOS HB CONFIG AFT FLAP ARC TEST	51.000	-40.000
{AMY257}	AMOOS CONFIGURATION HB BAS ROT DEL ELE=0	50.000	0.000
{AMY260}	AMOOS CONFIGURATION HB BAS ROT DEL ELE=-40	50.000	-40.000

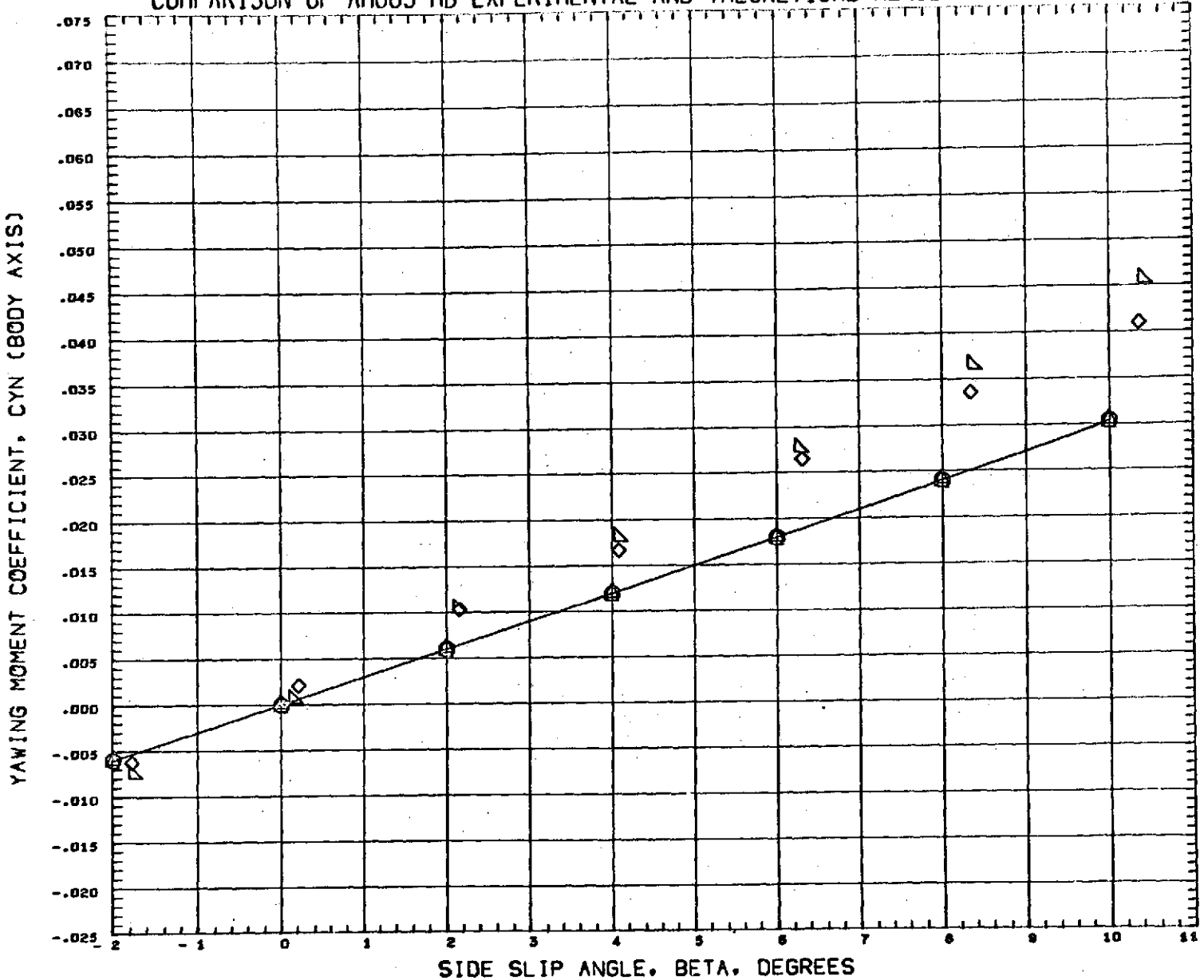
SEE THE ASSOCIATED DATA DOCUMENT FOR REFERENCE CHARACTERISTICS

MACH 10.270 26.800

Fig. 13k - Comparison of Theoretical and Experimental Side Force Coefficients for the HB Configuration with Expansion Flap Deflections of 0° and -40° at an Angle of Attack of 50°



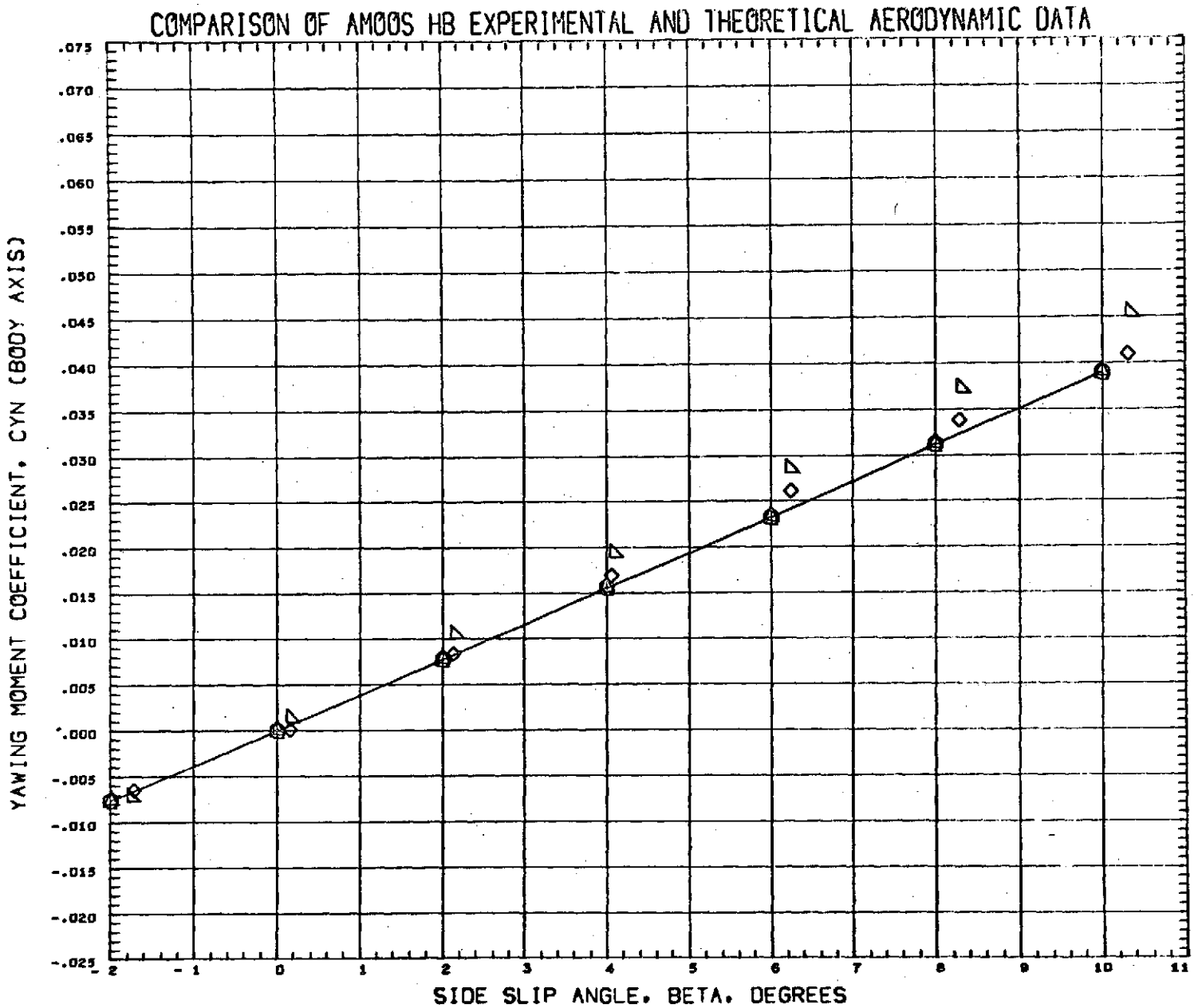
COMPARISON OF AMOOS HB EXPERIMENTAL AND THEORETICAL AERODYNAMIC DATA



DATA SET SYMBOL	CONFIGURATION DESCRIPTION	ALPHA	ELVATR	
(A00029)	AMOOS HB CONFIG AFT FLAP ARC TEST	40.000	0.000	SEE THE ASSOCIATED DATA DOCUMENT FOR REFERENCE CHARACTERISTICS
(A00032)	AMOOS HB CONFIG AFT FLAP ARC TEST	40.000	-40.000	
(A00049)	AMOOS CONFIGURATION HB BAS ROT DEL ELE=0	40.000	0.000	
(A00052)	AMOOS CONFIGURATION HB BAS ROT DEL ELE=-40	40.000	-40.000	

MACH 10.270 26.800

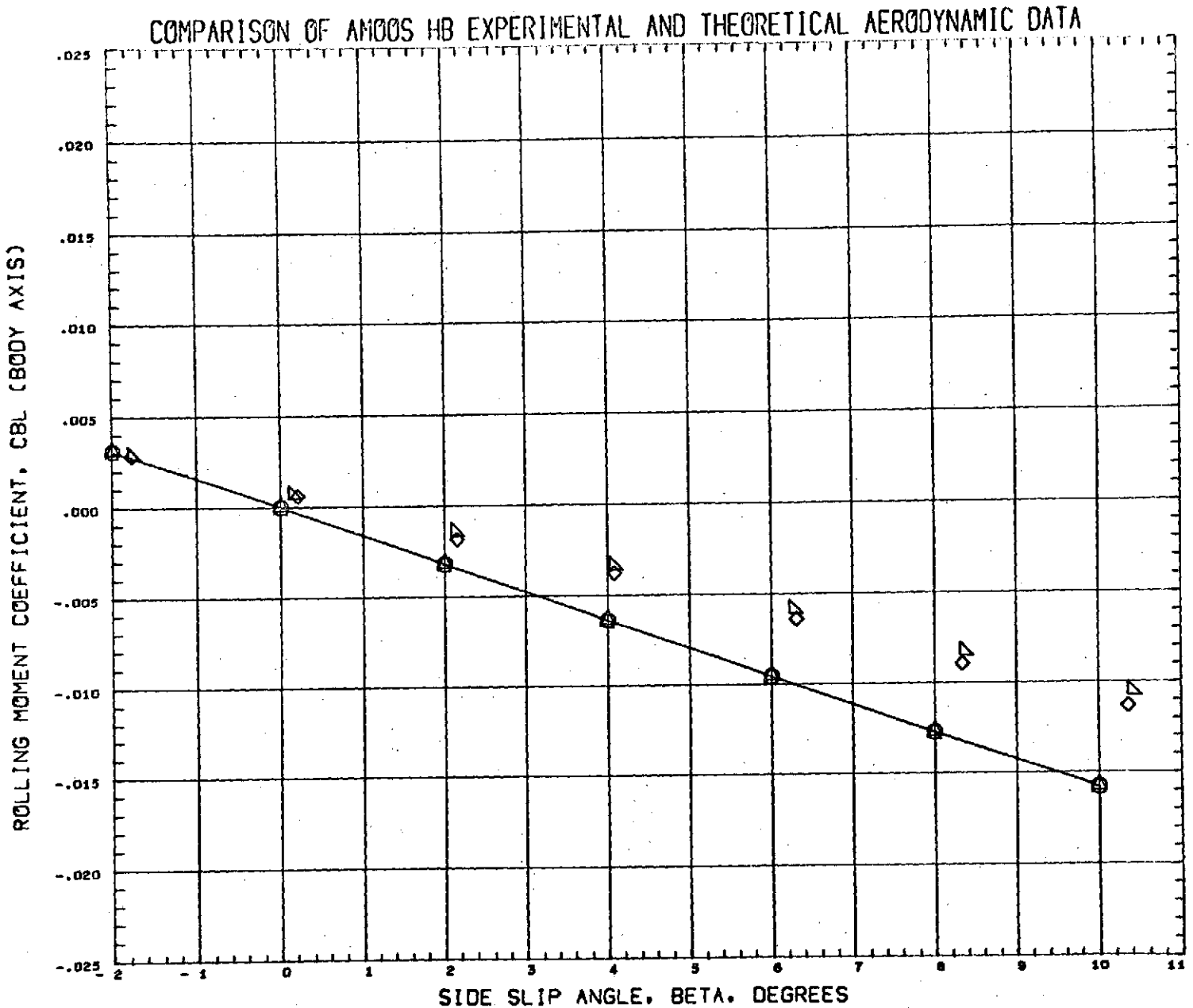
Fig. 131 - Comparison of Theoretical and Experimental Yawing Moment Coefficients for the HB Configuration with Expansion Flap Deflections of 0° and -40° at an Angle of Attack of 40°



DATA SET SYMBOL	CONFIGURATION DESCRIPTION	ALPHA	ELVATR	
(A00022)	AMOOS HB CONFIG AFT FLAP ARC TEST	50.000	0.000	SEE THE ASSOCIATED DATA DOCUMENT FOR REFERENCE CHARACTERISTICS
(A00021)	AMOOS HB CONFIG AFT FLAP ARC TEST	51.000	-40.000	
(AMY257)	AMOOS CONFIGURATION HB BAS ROT DEL ELE=0	50.000	0.000	
(AMY260)	AMOOS CONFIGURATION HB BAS ROT DEL ELE=-40	50.000	-40.000	

MACH      10.270      26.800

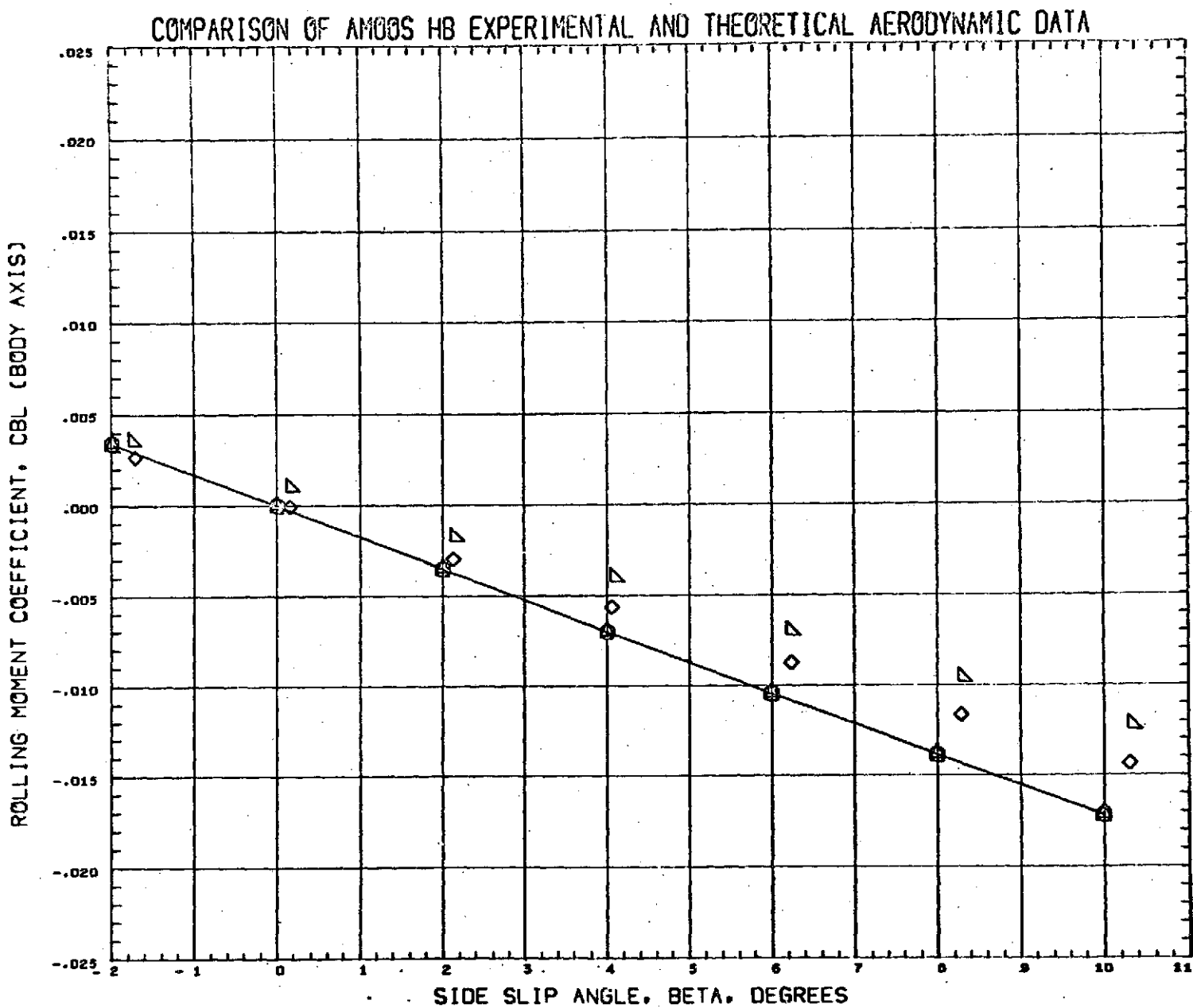
Fig. 13m - Comparison of Theoretical and Experimental Yawing Moment Coefficients for the HB Configuration with Expansion Flap Deflections of 0° and -40° at an Angle of Attack of 50°



DATA SET SYMBOL	CONFIGURATION DESCRIPTION	ALPHA	ELVATR	
(A00029)	AMOOS HB CONFIG AFT FLAP ARC TEST	40.000	0.000	SEE THE ASSOCIATED DATA DOCUMENT FOR REFERENCE CHARACTERISTICS
(A00032)	AMOOS HB CONFIG AFT FLAP ARC TEST	40.000	-40.000	
(ANYZ49)	AMOOS CONFIGURATION HB BAS ROT DEL ELE=0	40.000	0.000	
(ANYZ52)	AMOOS CONFIGURATION HB BAS ROT DEL ELE=-40	40.000	-40.000	

MACH      10.270      26.600

Fig. 13n - Comparison of Theoretical and Experimental Rolling Moment Coefficients for the HB Configuration with Expansion Flap Deflections of 0° and -40° at an Angle of Attack of 40°

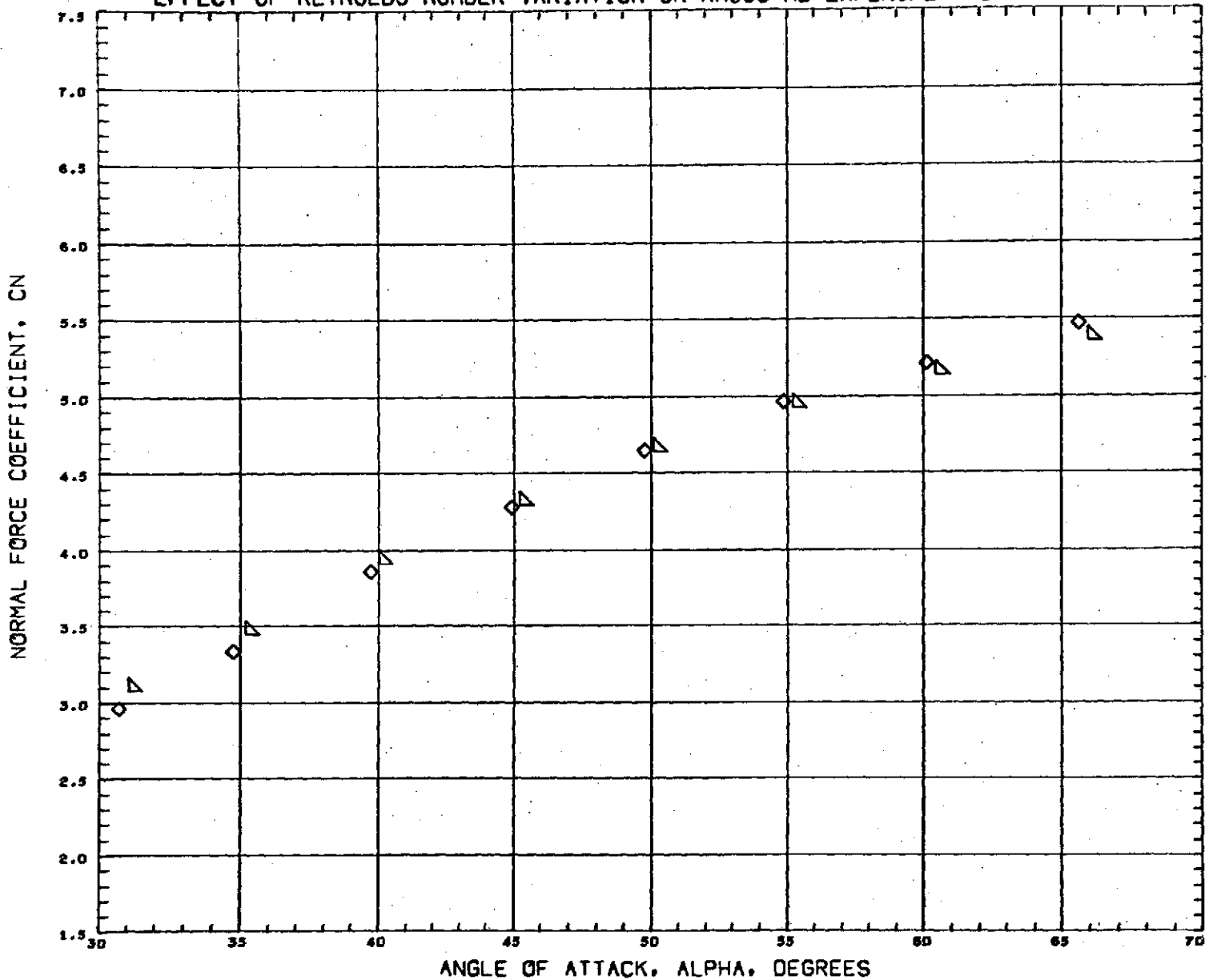


DATA SET SYMBOL	CONFIGURATION DESCRIPTION	ALPHA	ELVATR	
(A00022)	AMOOS HB CONFIG AFT FLAP ARC TEST	50.000	0.000	SEE THE ASSOCIATED DATA DOCUMENT FOR REFERENCE CHARACTERISTICS
(A00021)	AMOOS HB CONFIG AFT FLAP ARC TEST	51.000	-40.000	
(AMY257)	AMOOS CONFIGURATION HB SAS ROT DEL ELE=0	50.000	0.000	
(AMY260)	AMOOS CONFIGURATION HB SAS ROT DEL ELE=-40	50.000	-40.000	

MACH      10.270      26.800

Fig. 130 - Comparison of Theoretical and Experimental Rolling Moment Coefficients for the HB Configuration with Expansion Flap Deflections of 0° and -40° at an Angle of Attack of 50°

EFFECT OF REYNOLDS NUMBER VARIATION ON AMOOS HB EXPERIMENTAL DATA



DATA SET SYMBOL	CONFIGURATION DESCRIPTION	ALPHA	ELVATR	RN/L
(A00016)	△ AMOOS HB CONFIG FORWARD FLAP ARC TEST	40.000	1.200	
(A00025)	◇ AMOOS HB CONFIG FORWARD FLAP ARC TEST	40.000	0.600	

SEE THE ASSOCIATED DATA DOCUMENT FOR REFERENCE CHARACTERISTICS

MACH 10.270

Fig. 14a - Comparison of Normal Force Coefficients for the HB Configuration with the Compression Flap Deflected 40° at Two Different Reynolds Numbers

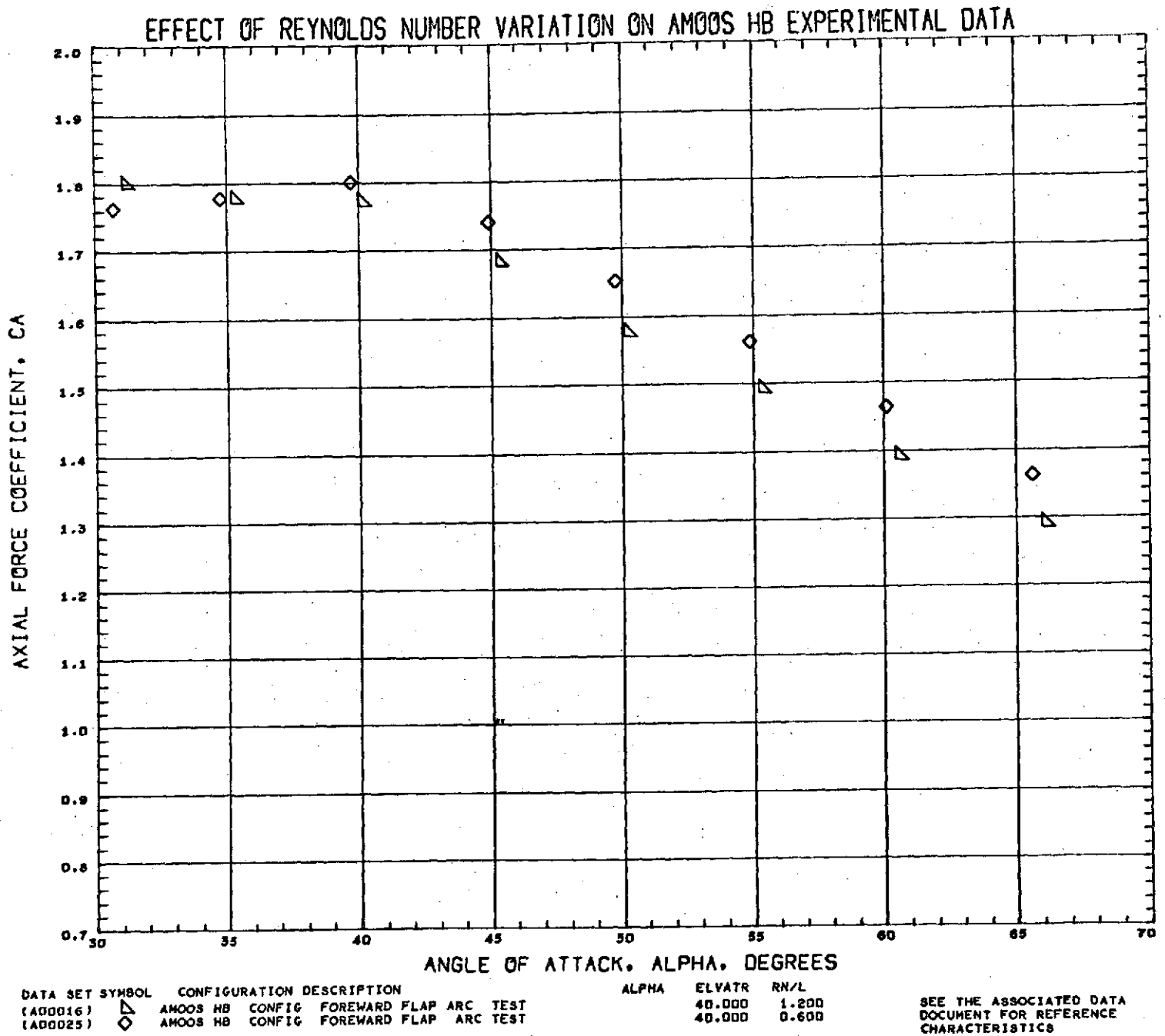


Fig. 14b - Comparison of Axial Force Coefficients for the HB Configuration with the Compression Flap Deflected 40° at Two Different Reynolds Numbers

Appendix A

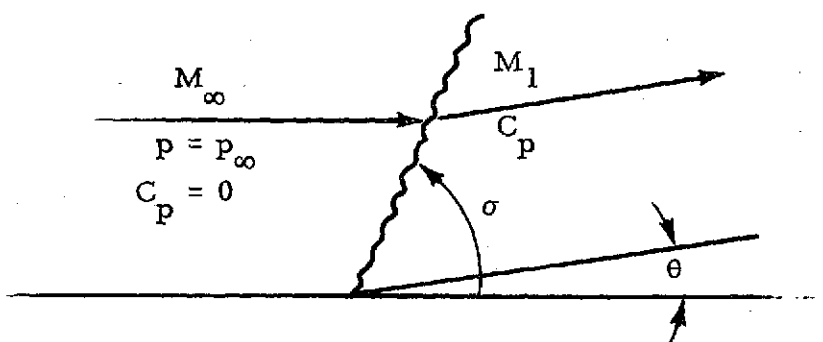
JUSTIFICATION FOR USE OF NEWTONIAN  
FLOW THEORY



### Appendix A

The validity of the use of Newtonian theory for AMOOS applications may be examined from the point of view of two basic equations – two oblique shock relationships.

A schematic of the flow situation is presented below.



Consider hypersonic flow attempting to negotiate a compression corner with included angle  $\theta$  having a freestream Mach number,  $M_\infty$ , and  $p = p_\infty$ . The conditions behind the resulting shock are labeled as  $M_1$  and  $\rho_1$  and the shock angle is labeled  $\sigma$ . The pressure coefficient behind the shock may be calculated by the equation:

$$C_p = \frac{2 \sin \sigma \sin \theta}{\cos(\sigma - \theta)} \quad (\text{Ref. A-1}) \quad (\text{A.1})$$

Also the density ratio across the shock may be calculated by the equation:

$$\rho_1 / \rho_\infty = \frac{\gamma + 1}{\left( \frac{2}{M_\infty^2 \sin^2 \sigma} \right) + (\gamma - 1)} = \frac{\tan \sigma}{\tan(\sigma - \theta)} \quad (\text{Ref. A-2}) \quad (\text{A.2})$$

For hypersonic flow as  $M_\infty \rightarrow \infty$  the shock angle  $\sigma$  becomes smaller and eventually approaches  $\theta$ , therefore:

$$(\sigma - \theta) \text{ is very small and}$$

$$M_\infty^2 \sin^2 \sigma \rightarrow \infty$$

Equation (A.2) reduces to

$$\rho/\rho_\infty = \frac{\gamma+1}{\gamma-1} \doteq \frac{\tan \sigma}{(\sigma - \theta)} \quad (\text{Ref. A-3})$$

or

$$\sigma \doteq \theta + \frac{\gamma-1}{\gamma+1} \tan \sigma \doteq \theta + \frac{\gamma-1}{\gamma+1} \sigma$$

or

$$\sigma \doteq \frac{\gamma+1}{2} \theta \quad \text{for air } 1.0 < \gamma < 1.4 \quad (\text{A.3})$$

Now substitute  $\sigma$  from Eq. (A.3) into Eq. (A.1).

$$C_p = \frac{2 \sin \left\{ \left( \frac{\gamma+1}{2} \right) \theta \right\} \sin \theta}{\cos(\sigma - \theta)}$$

or

$$C_p \doteq 2 \sin \left\{ \left( \frac{\gamma+1}{2} \right) \theta \right\} \sin \theta \quad (\text{A.4})$$

as  $(\sigma - \theta)$  approaches 0.

For small angles it can be shown that

$$\sin \left( \frac{\gamma+1}{2} \right) \theta \doteq \left( \frac{\gamma+1}{2} \right) \sin \theta$$

Then

$$C_p = 2 \left( \frac{\gamma+1}{2} \right) \sin\theta \sin\theta$$

$$C_p = (\gamma+1) \sin^2\theta = 2 \sin^2\theta \quad (\text{A.5})$$

as  $\gamma \rightarrow 1$  as  $M_\infty \rightarrow \infty$ .

Equation (A.5) which was used by the Hypersonic Arbitrary Body Computer Program is therefore valid for high Mach numbers and application to high temperature environments where  $\gamma \rightarrow 1$ .

REFERENCES

- A-1. Ames Research Staff, "Equations, Tables, and Charts for Compressible Flow," NACA Report 1135, Ames Aeronautical Laboratory, Moffett Field, Calif., 1953.
- A-2. Liepmann, H. W., and A. Roshko, Elements of Gasdynamics, Wiley, New York, February 1960.
- A-3. Truitt, Robert Wesley, Hypersonic Aerodynamics, The Ronald Press Company, New York, 1959.